Longitudinal Monitoring of Biohybrid Tissue-Engineered Vascular Grafts by Multimodal
Molecular Imaging

List of publications

List of publications included in this thesis:

Rama E, Mohapatra S R, Sugimura Y, Suzuki T, Siebert S, Barmin R, Hermann J, Baier J, Rix A, Lemainque T, Koletnik S, Elshafei A S, Pallares R M, Dadfar S M, Tolba R H, Schulz V, Jankowski J, Apel C, Akhyari P, Jockenhoevel S, Kiessling F. *In Vitro and in Vivo Evaluation of Biohybrid Tissue-Engineered Vascular Grafts with Transformative 1H/19F MRI Traceable Scaffolds*, Biomaterials, 2024.

Rama E, Mohapatra S R, Melcher C, Nolte T, Dadfar S M, Brueck R, Pathak V, Rix A, Gries T, Schulz V, Lammers T, Apel C, Jockenhoevel S, Kiessling F. *Monitoring the Remodeling of Biohybrid Tissue-Engineered Vascular Grafts by Multimodal Molecular Imaging*, Advanced Science, 2022.

Other publications - *Denotes equal contribution:

Koczera P, Thomas F, **Rama E**, Thoröe-Boveleth S, Kiessling F, Lammers T, Herres-Pawlis S. *Microbubble-encapsulated Cobalt Nitrato Complexes for Ultrasound-triggerable Nitric Oxide Delivery*, ChemMedChem, 2024.

Darguzyte M*, **Rama E***, Rix A, Baier J, Hermann J, Rezvantalab S, Khedri M, Jankowski J, Kiessling F. *Riboflavin-targeted polymers improve tolerance of paclitaxel while maintaining therapeutic efficacy*, Nanomedicine: Nanotechnology, Biology and Medicine, 2024.

Barmin B A, Moosavifar M J, Zhang R, Rütten S, Thoröe-Boveleth S, **Rama E**, Ojha T, Kiessling F, Lammers T, Pallares R M. *Hybrid ultrasound and photoacoustic contrast agent designs combining metal phthalocyanines and PBCA microbubbles*, Journal of Materials Chemistry B, 2024.

Möckel D, Bartneck M, Niemietz P, Wagner M, Ehling J, **Rama E**, Weiler M, Gremse F, Eulberg D, Pola R, Pechar M, Etrych T, Storm G, Kiessling F, Tacke F, Lammers T. *CCL2 chemokine inhibition primes the tumor vasculature for improved nanomedicine delivery and efficacy*, Journal of Controlled Release, 2024.

Dasgupta A, Sun T, **Rama E**, Motta A, Zhang Y, Power C, Moeckel D, Fletcher S M, Moosavifar M J, Barmin R, Porte C, Buhl E M, Bastard C, Pallares R M, Kiessling F, McDannold N, Mitragotri S, Lammers T. *Transferrin Receptor-Targeted Nonspherical Microbubbles for Blood–Brain Barrier Sonopermeation*, Advanced Materials, 2023.

Biancacci I, De Santis D, **Rama E**, Benderski K, Momoh J, Pohlberger R, Moeckel D, Kaps L, Rijcken C J F, Prakash J, Thewissen M, Kiessling F, Shi Y, Peña Q, Sofias A M, Consolino L, Lammers T. *Repurposing Tamoxifen for Tumor Microenvironment Priming and Enhanced Tumor-Targeted Drug Delivery*, Advanced Therapeutics, 2023.

Dasgupta A, Sun T, Palomba R, **Rama E**, Zhang Y, Power C, Moeckel D, Liu M, Sarode A, Weiler M, Motta A, Porte C, Magnuska Z, Elshafei A S, Barmin R, Graham A, McClelland A, Rommel D, Stickeler E, Kiessling F, Pallares R M, De Laporte L, Decuzzi P, McDannold N, Mitragotri S, Lammers T. *Nonspherical ultrasound microbubbles*, Proceedings of the National Academy of Sciences, 2023.

Tezcan O, Elshafei A S, Benderski K, **Rama E**, Wagner M, Moeckel D, Pola R, Pechar M, Etrych T, von Stillfried S, Kiessling F, Weiskirchen R, Meurer S, Lammers T. *Effect of

Cellular and Microenvironmental Multidrug Resistance on Tumor-Targeted Drug Delivery in Triple-Negative Breast cancer, Journal of Controlled Release, 2023.

Mohapatra S R, **Rama E**, Melcher C, Call T, Al Enezy-Ulbrich M A, Pich A, Apel C, Kiessling F, Jockenhoevel S. *From In Vitro to Perioperative Vascular Tissue Engineering: Shortening Production Time by Traceable Textile-Reinforcement*, Tissue Engineering and Regenerative Medicine, 2022.

Pathak V, Nolte T, **Rama E**, Rix A, Dadfar S M, Paefgen V, Banala S, Buhl E M, Weiler M, Schulz V, Lammers T, Kiessling F. *Molecular magnetic resonance imaging of Alpha-v-Beta-3 integrin expression in tumors with ultrasound microbubbles*, Biomaterials, 2021.

Liu M, Dasgupta A, Qu N, **Rama E**, Kiessling F, Lammers T. *Strategies to Maximize Anthracycline Drug Loading in Albumin Microbubbles*, ACS Biomaterials Science & Engineering, 2021.

Monitoring the Remodeling of Biohybrid Tissue-Engineered Vascular Grafts by Multimodal Molecular Imaging

Elena Rama, Saurav Ranjan Mohapatra, Christoph Melcher, Teresa Nolte,
Seyed Mohammadali Dadfar, Ramona Brueck, Vertika Pathak, Anne Rix, Thomas Gries,
Volkmar Schulz, Twan Lammers, Christian Apel, Stefan Jockenhoevel,
and Fabian Kiessling*

Tissue-engineered vascular grafts (TEVGs) with the ability to grow and remodel open new perspectives for cardiovascular surgery. Equipping TEVGs with synthetic polymers and biological components provides a good compromise between high structural stability and biological adaptability. However, imaging approaches to control grafts' structural integrity, physiological function, and remodeling during the entire transition between late in vitro maturation and early in vivo engraftment are mandatory for clinical implementation. Thus, a comprehensive molecular imaging concept using magnetic resonance imaging (MRI) and ultrasound (US) to monitor textile scaffold resorption, extracellular matrix (ECM) remodeling, and endothelial integrity in TEVGs is presented here. Superparamagnetic iron-oxide nanoparticles (SPION) incorporated in biodegradable poly(lactic-*co*-glycolic acid) (PLGA) fibers of the TEVGs allow to quantitatively monitor scaffold resorption via MRI both in vitro and in vivo. Additionally, ECM formation can be depicted by molecular MRI using elastin- and collagen-targeted probes. Finally, molecular US of $\alpha_v\beta_3$ integrins confirms the absence of endothelial dysfunction; the latter is provocable by TNF-α. In conclusion, the successful employment of noninvasive molecular imaging to longitudinally evaluate TEVGs remodeling is demonstrated. This approach may foster its translation from in vitro quality control assessment to in vivo applications to ensure proper prostheses engraftment.

1. Introduction

Despite major discoveries and successes that occurred in the field of prevention and treatment of cardiovascular diseases, they remain the leading cause of death worldwide.[1,2] Cardiovascular pathologies are associated with a broad spectrum of comorbidities, including partial occlusion or complete loss of patency, aneurism of the vessel wall, reduced blood supply, and consequently insufficient nutrients uptake leading to tissue damage and inflammation.

Tissue engineering (TE) has the potential to improve, repair, or replace partially or completely damaged tissues and organs through the development of prostheses mimicking both functionally and biologically the native structures. In recent decades, enormous progress has been made in the study and development of cardiovascular implants, vascular prostheses, patches, stents, and shunts.[3] About 600 000 surgical operations using such revascularization devices are performed annually. However, once implanted in the body, many of the synthetic prosthetic

E. Rama, T. Nolte, S. M. Dadfar, R. Brueck, V. Pathak, A. Rix, V. Schulz,
T. Lammers, F. Kiessling
Institute for Experimental Molecular Imaging University Clinic and
Helmholtz Institute for Biomedical Engineering RWTH – Aachen
University Forckenbeckstrasse 55
52074 Aachen, Germany
E-mail: fkiessling@ukaachen.de

S. R. Mohapatra, C. Apel, S. Jockenhoevel
Department of Biohybrid & Medical Textiles
Institute of Applied Medical Engineering RWTH – Aachen University
Forckenbeckstrasse 55
52074 Aachen, Germany
C. Melcher, T. Gries
Institute for Textile Technology RWTH – Aachen University
Forckenbeckstrasse 55
52074 Aachen, Germany

models clinically used today, i.e., expanded polytetrafluoroethylene (GORE-TEX) and poly(ethylene terephthalate) (Dacron), show poor outcomes. Their lack of in vivo remodeling and growth proficiency in addition to inadequate hemocompatibility can result in complete occlusion of the prostheses, thrombus formation, calcific deposition, hyperplasia of the intima, and biomechanical properties mismatch.[4–7]

TE is now focusing on the employment of a combination of synthetic materials, which provide mechanical strength, and biological components to contribute to the biocompatibility of the prostheses with the host organism. In this context, a refined strategy to ensure high biocompatibility and functionality of vascular graft is to provide strong structural support with synthetic material at the early post-transplantation phase to avoid graft rupture, but also to have parts of the scaffold being degraded to maintain a mechanical trigger stimulating extracellular matrix (ECM) production and minimizing the amount of synthetic material finally remaining in the body. This can be achieved by combining a nondegradable with a biodegradable scaffold material. In this view, poly(lactic-co-glycolic acid) (PLGA) is becoming one of the most used synthetic materials for the fabrication of TE prostheses.[8,9] Moreover, it is a Food and Drug Administration (FDA) approved, biocompatible and biodegradable copolymer, characterized by intrinsic favorable mechanical capabilities, a tailorable biodegradation rate, and the release of nontoxic degradation products.[10] However, the accumulation of these degradation products, i.e., lactic and glycolic acid, raises several concerns especially because they trigger the decrease of the pH in the surrounding environment leading to swelling of the tissues as well as inflammatory (acute and chronic) and foreign body reactions.[11] Therefore, there is a high demand to intensify the investigation of prostheses' behavior and performances upon in vivo implantation.

The implementation of noninvasive and nondestructive monitoring tools is highly desirable as they could strongly foster clinical translation of TE implants and enable the early detection of therapeutically reversible dysfunctions, i.e., damage on the integrity of the prostheses and loss of functionality. From this point of view, magnetic resonance imaging (MRI) is an attractive imaging modality because, unlike computed tomography (CT) and X-ray, it does not require ionizing radiation and is characterized by high spatial and temporal resolution with excellent soft-tissue contrast. Similarly, ultrasound (US) is widely used in the clinic because it provides outstanding real-time diagnostic and imaging information with high patient safety.[12–14]

Nonetheless, conventional MRI and US are inadequate to monitor textile scaffold components and cellular behavior within TE implants. Novel approaches toward the incorporation of MRI contrast agents into the textile scaffold and cells embedded into the structure of vascular grafts have already been investigated and proved to be efficient for their visualization.[4,15,16] However, comprehensive diagnostic tools for monitoring implant remodeling from late in vitro bioreactor conditioning to early in vivo implantation, being the most critical phase, are still hardly available.

In this regard, this study aimed to develop imageable biohybrid vascular scaffolds and a comprehensive molecular imaging concept to monitor their late in vitro conditioning and the early in vivo implantation phase. The imaging concept included the assessment of the textile scaffold remodeling, deposition of main ECM components, and the onset of potential inflammatory reactions. As shown in **Figure 1**, we first developed tissue-engineered vascular grafts (TEVGs) consisting of nondegradable warp-knitted polyvinylidene fluoride (PVDF) tubular meshes coated with degradable and biocompatible e-spun PLGA fibers that were molded into fibrin gel containing smooth muscle cells (SMCs) and endothelial cells (ECs). Additionally, superparamagnetic iron oxide nanoparticles (SPION) were passively incorporated into the PLGA fibers allowing the longitudinal monitoring of the degradable copolymer by MRI. Furthermore, the replacement of the degraded fibers by deposition of newly synthesized ECM components was assessed via means of elastin- and collagen type I-targeted MRI molecular gadolinium-based probes (ESMA and EP-3533). Moreover, molecular ultrasound imaging with c[RGDfK]-functionalized poly(n-butyl cyanoacrylate) microbubbles (c[RGDfK]-MBs) was employed to assess $\alpha v\beta 3$ integrin expression as a marker of inflammation and endothelial dysfunction.

2. Results and Discussion

2.1. MRI Reliably Detects SPION-Labeled Scaffolds and Captures PLGA Degradation

Despite the high biocompatibility of PLGA, its invisibility by noninvasive imaging makes it an uncontrollable component when used as scaffold material of the vascular prosthesis. This is particularly critical during the in vitro conditioning and in vivo remodeling phase.

To overcome this hurdle, we passively labeled the PLGA fibers with SPION (**Figure 2**a). These iron-oxide nanoparticles lead to local susceptibilities and predominantly decrease T2 and T2* relaxation times (respectively increase the R2 and R2* relaxation rates), resulting in a strong hypointense MRI contrast. The resulting R2 quantitative MRI analyses of the different PLGA samples, as depicted in Figure 2b, showed a significant improvement in fiber detectability with increasing SPION concentrations (R2 values for control: (4.3 ± 0.3) s^{-1}; 0.2% SPION-labeled PLGA fibers: (5.9 ± 0.9) s^{-1}; 0.4% SPION-labeled PLGA fibers: (7.5 ± 1.3) s^{-1}). Interestingly, for R2* the difference between the samples was less prominent and not significant although, also here, a slightly increased relaxation rate was detected with higher SPION concentration (Figure 2c; R2* values for control: (12.6 ± 9.3) s^{-1}; 0.2% SPION-labeled PLGA fibers: (117 ± 10.6) s^{-1}; 0.4% SPION-labeled PLGA fibers: (203 ± 106) s^{-1}). The statistical insignificance of R2* changes may be explained by the high sensitivity of the employed gradient echo sequence not only to the presence of SPION, but also to SPION unrelated inhomogeneities in the main magnetic B0 field that might have persisted even after performing field map-based shimming. Hence, R2 was selected for all subsequent analyses.

Encouraged by the improved visibility of the SPION-labeled PLGA fibers via MRI, the PLGA fibers, electrospun for 10 and 30 min, were subsequently evaluated in combination with the warp-knitted PVDF tubular structures that are the main supporting and nonbiodegradable component of the textile scaffolds in the vascular graft (Figure 2d-e). As displayed in Figure 2f, the SPION-labeled PLGA fibers showed higher R2 relaxation rates in comparison with the unlabeled control (R2 values for 10 min of PLGA electrospinning: control: (5.4 ± 0.1) s^{-1}; 0.2% SPION-
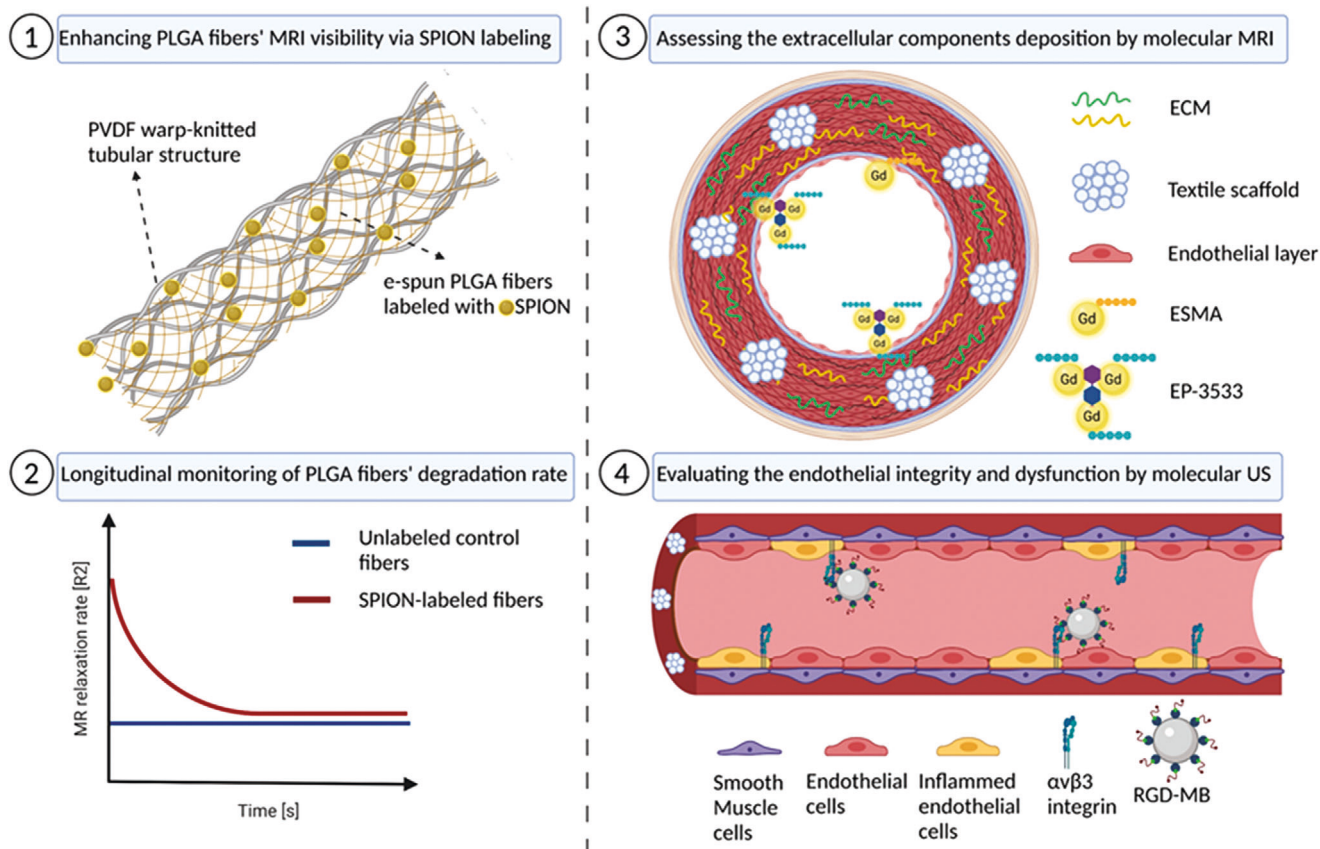
Figure 1. Schematic depiction of the study design (created with BioRender.com).

labeled PLGA fibers: (8.2 ± 1.4) s−1; 0.4% SPION-labeled PLGA fibers: (11.2 ± 2.1) s−1; R2 values for 30 min of PLGA electrospinning: control: (5.1 ± 0.3) s−1; 0.2% SPION-labeled PLGA fibers: (9.5 ± 0.3) s−1; 0.4% SPION-labeled PLGA fibers: (10.9 ± 1.1) s−1). However, no difference was observed between the 10 and 30 min of PLGA electrospinning conditions. Therefore, the increase of the electrospinning time and hence the thickness of the PLGA coating layer do not affect the MRI detection of these fibers.

After confirming the MRI visibility of the SPION-labeled PLGA fibers, the degradation rate of the copolymer was evaluated. The R2 values of SPION-labeled PLGA multilayer sheets decreased over time, which can be explained by the release of the SPION from the swollen and degrading fibers (**Figure 3**a–c; R2 values for control at week 1: (3.6 ± 0.7) s−1 versus week 11: (2.3 ± 0.1) s−1; 0.2% SPION-labeled PLGA fibers at week 1: (11.3 ± 8.5) s−1 versus week (11: (4.7 ± 0.8) s−1; 0.4% SPION-labeled PLGA fibers at week 1: (21.2 ± 4.0) s−1 versus week 11: (5.2 ± 0.5) s−1).[17]

Next, the SPION-labeled PLGA fibers were investigated in combination with the PVDF tubular structure and incubated in PBS. In compliance with the electrospinning procedure, only the 0.2% SPION concentration was used in this and subsequent studies to avoid clustering of the iron-oxide nanoparticles at high concentrations.[18] The change in the relaxation rates (Figure 3e–f), reflecting the degradation of the fibers, was better depicted for the SPION-labeled PLGA fibers in comparison to the unlabeled

control ones (R2 values for unlabeled control at week 1: (2.2 ± 0.1) s−1 versus week 3: (1.7 ± 0.1) s−1; 0.2% SPION-labeled PLGA fibers at week 1: (7.3 ± 0.6) s−1 versus week 3: (1.9 ± 0.1) s−1). Interestingly, the incubation of the samples in an aqueous environment, such as PBS in comparison to the stiffer fibrin gel used in the previous experimental setup, might have accelerated the degradation rate of the fibers, in this case occurring after 3 weeks compared to 11 weeks observed in the previous study.

The final experiment on the degradation of SPION-labeled PLGA fibers was performed using complete biohybrid vascular scaffolds (Figure 3g). For this purpose, the textile scaffold consisting of a warp-knitted PVDF tubular structure coated with SPION-labeled PLGA fibers was embedded in fibrin gel containing SMCs and ECs. In contrast to the unlabeled control, the degradation of the SPION-labeled PLGA fibers was again trackable via MRI (R2 values for control at day 1: (4.0 ± 0.3) s−1 versus day 7: (3.0 ± 0.9) s−1; 0.2% SPION-labeled PLGA fibers at day 1: (6.2 ± 0.7) s−1 versus day 7: (3.5 ± 0.1) s−1). The degradation of the fibers was strongly accelerated and occurred in only 7 days (Figure 3h–i). Furthermore, R2 analyses also displayed a slight increase in the medium relaxation values corresponding to the decrease of the R2 values of the SPION-labeled PLGA fibers, indicating the release of the SPION from the fibers and their following accumulation in the circulating medium (Figure S1, Supporting Information). The faster degradation of PLGA fibers may be explained by the presence of cells. Due to ATP
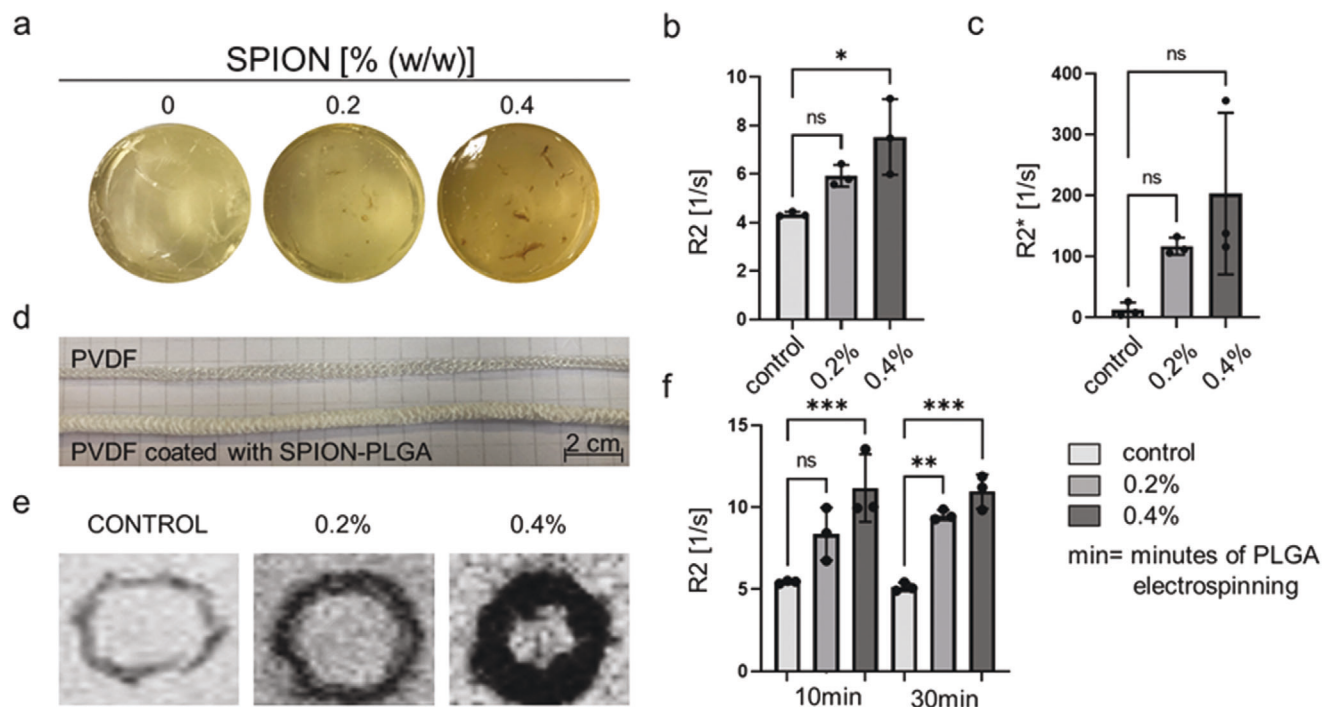
**ADVANCED
SCIENCE NEWS**

www.advancedsciencenews.com

**ADVANCED
SCIENCE**
Open Access

www.advancedscience.com

Figure 2. MRI investigation of SPION-labeled PLGA fibers. a) Gelatin phantoms containing 0%, 0.2%, and 0.4% (w/w) of SPION. b,c) R2 and R2* analyses of SPION-labeled PLGA fibers (both concentrations) in comparison to the unlabeled control. d) Visual comparison between an uncoated and SPION-labeled PLGA-coated PVDF tubular scaffold. e) T2 weighted MRI images of PVDF tubular scaffolds coated with 0.2% and 0.4% (w/w) of SPION. f) R2 analyses of different PLGA electrospinning time, 10 and 30 min, containing 0.2% and 0.4% (w/w) of SPION. All values were obtained in triplicates: mean ± SD; t-test with Tukey post hoc correction test was applied; ns > 0.05, *$p < 0.05$, **$p < 0.01$, ***$p < 0.001$, and ****$p < 0.0001$.

production and oxidative phosphorylation in the mitochondria of cells, the extracellular pH (normally 7.4) can locally become acidic and range between 5.7 and 6.1 during the early stages of wound healing.[19] The acidic pH triggers PLGA degradation by ester hydrolysis in acidic conditions.[20] This also leads to an enhanced accumulation of PLGA degradation products (lactic and glycolic acid), which further enhances and accelerates the drop in pH and, thus, the degradation process. Furthermore, PLGA degradation was additionally investigated via histological staining after 1, 3, and 7 days of bioreactor cultivation of TEVGs. H&E staining showed the gradual disappearing of the PLGA fiber network and filling of the spaces by cells and new ECM components (Figure S2, Supporting Information).[21,22]

As an initial proof-of-concept for the in vivo visibility and longitudinal monitorability of our vascular grafts, both SPION-labeled TEVGs and unlabeled control were subcutaneously implanted on the left and right side of the dorsum of Lewis male rats. As shown in **Figure 4**a, animals were longitudinally monitored for 21 days via MRI. The R2 relaxometry of SPION-labeled TEVGs showed significantly higher values in comparison to unlabeled controls, indicating a significant improvement in TEVGs detectability due to SPION incorporation (Figure 4b; R2 values for control: (16.1 ± 2.4) s⁻¹; SPION-labeled PLGA fibers: (20.9 ± 0.8) s⁻¹). Furthermore, decreases in relaxation rate values during the 21 days of MRI evaluation indicated PLGA fibers' degradation and the corresponding release of SPION (Figure 4c; R2 values for control at day 1: (16.05 ± 2.4) s⁻¹ versus day 21: (16.12 ± 1.8) s⁻¹; R2 values for SPION-labeled PLGA fibers at day 1: (20.9 ± 0.8) s⁻¹ versus

day 21: 17.9 ± 1.3). Ex vivo H&E staining confirmed the gradual infiltration of cells within the vascular grafts together with the concomitant degradation of the PLGA fibers and their replacement by new ECM (Figure 4d).

2.2. Molecular MRI Depicts the Extracellular Matrix

The main mechanical properties of blood vessels are provided by two major ECM components, i.e., collagen and elastin.[23] Collagen sponge-matrix guarantees the tensile stiffness and is required to sustain high blood pressure and to prevent rupture. Elastin confers tissue elasticity, i.e., dynamic stretching under pressure and recoiling to its original configuration.[24,25]

In our TEVGs, ECM remodeling coincides with the PLGA fiber degradation and was characterized using elastin-targeted (ESMA) and collagen-type-I-targeted (EP-3533) molecular MRI probes. Both probes have already been extensively characterized.[26–28] Untargeted Gd-DTPA (Magnevist, Bayer, Germany) and human umbilical arteries (HUA), which are rich in collagen and elastin, were used as a negative and as a positive control, respectively (**Figure 5**a–d). Interestingly, the quantitative R1 analyses showed almost no ESMA accumulation in TEVGs (R1 precontrast agents: (0.4± 0.1) s⁻¹; R1 post-ESMA: (0.4 ± 0.1) s⁻¹; R1 post-Magnevist: (0.4 ± 0.1) s⁻¹) indicating that no elastin fibers were produced and deposited during the 14 days of bioreactor conditioning and maturation of the vascular grafts (Figure 5b). Furthermore, the lack of elastin fibers deposition
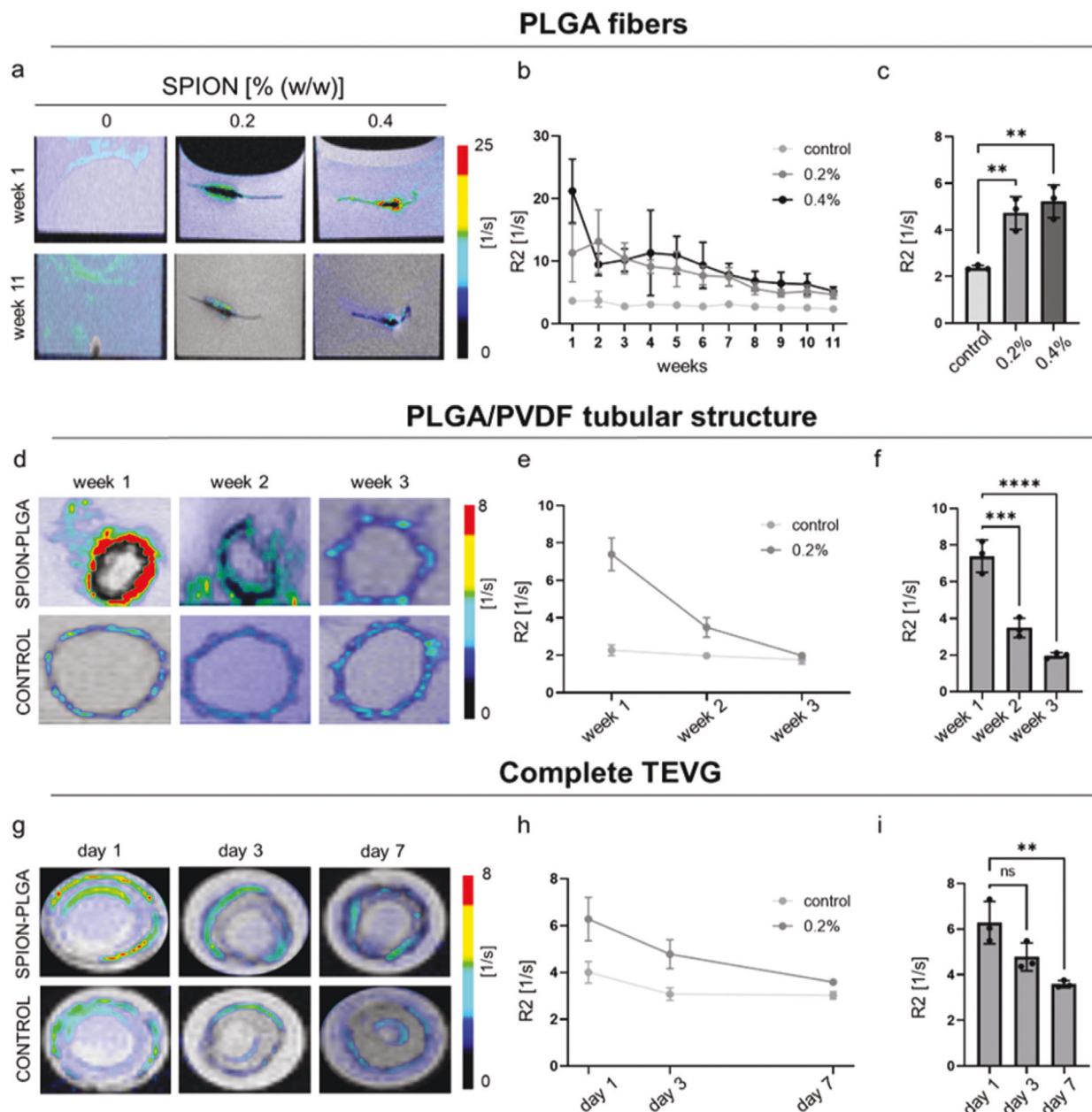
Figure 3. Monitoring of PLGA fiber degradation by MRI. a) Superimposed R2 color maps on T2 weighted images of 0.2% and 0.4% (w/w) SPION-labeled PLGA fibers embedded in fibrin gel during the first week (top) and the last week (bottom) of the experiment. b) R2 relaxation rates of the different PLGA fibers over time. c) Comparison of R2 values between SPION-labeled PLGA fibers and the unlabeled control at the end of the experiment. d) R2 color maps superimposed on T2 weighted images of SPION-labeled PLGA fibers combined with the PVDF tubular scaffold (top) and of unlabeled controls (bottom) in PBS. e) R2 relaxation rates of 0.2% SPION-labeled PLGA fibers in comparison to the unlabeled control. f) R2 values of 0.2% SPION-labeled PLGA fibers decrease as a result of fibers degradation. g) T2 weighted MRI images of the complete TEVGs with SPION-labeled (top) and unlabeled PLGA fibers (bottom), with corresponding superimposed R2 color map. h,i) R2 relaxometry confirms the degradation of 0.2% SPION-labeled PLGA fibers in comparison to the unlabeled controls and their faster degradation in the presence of SMCs and ECs. All values were obtained in triplicates: mean ± SD; one-way ANOVA b,e,h) and t-test c,f,i) with Tukey post hoc correction test were applied; ns > 0.05, $^{*}p < 0.05$, $^{**}p < 0.01$, $^{***}p < 0.001$, and $^{****}p < 0.0001$.

within our TEVGs was confirmed via immunofluorescence histology and microscopy (Figure 5g). The regulation of elastin molecular precursor synthesis and the formation of elastic fibers within a 3D fibrin culture remains unclear. Niklason et al. reported only little elastin deposition suggesting that the accumulation of the degradation products of their TEVGs might have impaired ECM deposition.[29] In contrast, Jockenhoevel et al. confirmed the presence of elastin within their biohybrid vascular grafts, arguing for a balanced use of fibrin gel and ascorbate for boosting elastin production and deposition.[30] In support of the latter, Long and Tranquillo also showed an enhanced elastin production by SMCs, when seeded in fibrin gels, suggesting a
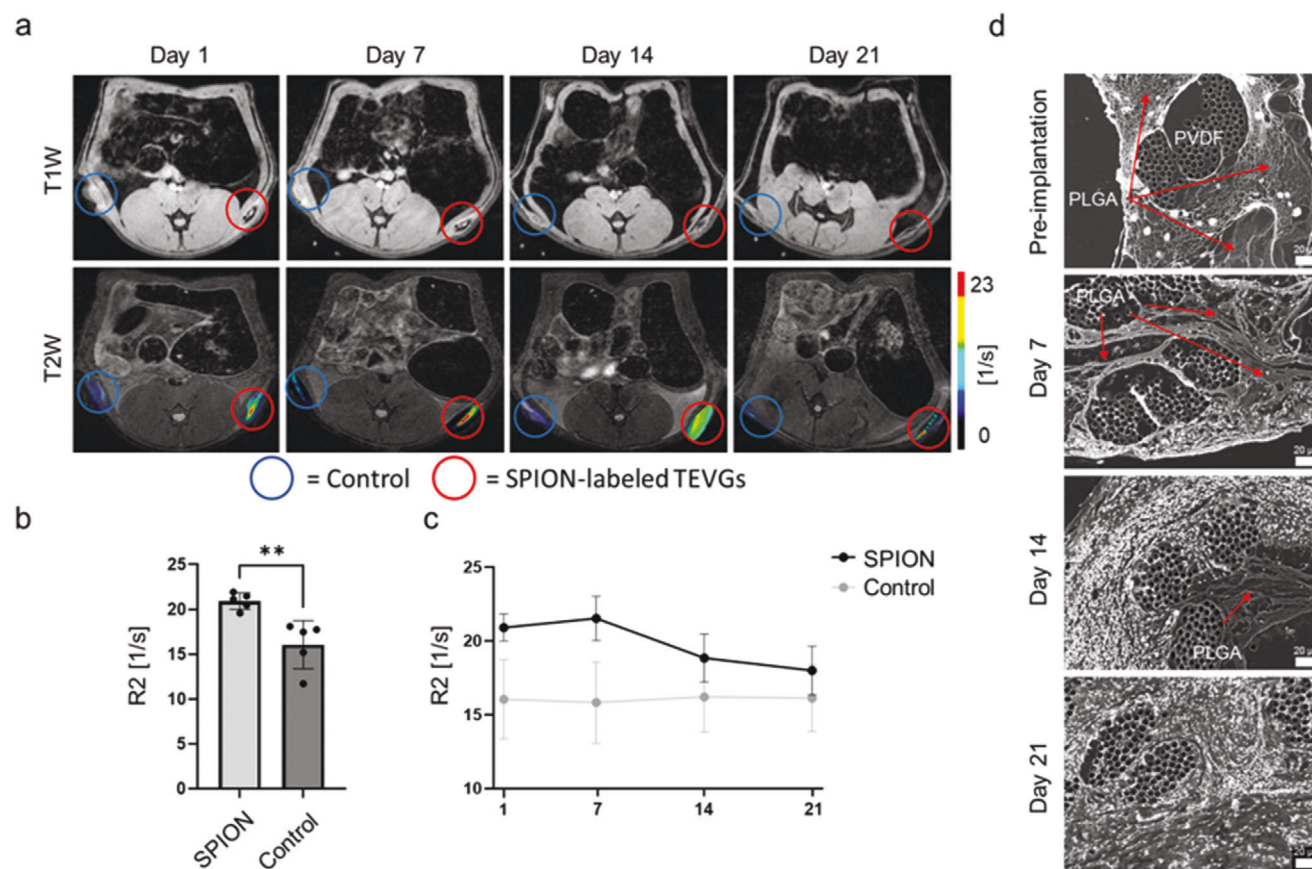
**ADVANCED
SCIENCE NEWS**

www.advancedsciencenews.com

**ADVANCED
SCIENCE**
Open Access

www.advancedscience.com

Figure 4. In vivo longitudinal monitoring of SPION-labeled PLGA degradation. a) T1- and T2-weighted MRI images of subcutaneously implanted SPION-labeled TEVGs (red circles) and unlabeled controls (blue circles) for 21 days. R2 color maps of both samples superimposed on the gray scale T2-weighted images highlight the PLGA fibers degradation over time. b) Comparison of the R2 relaxation rate of SPION-labeled TEVGs and unlabeled controls at day. c) R2 relaxation rate of SPION-labeled and unlabeled TEVGs over 21 days. d) Ex vivo histological evaluation of explanted TEVGs via H&E staining (shown in gray scale). All values were obtained in triplicates: mean $\pm$ SD; t-test b) and one-way ANOVA c) and with Tukey post hoc correction test were applied; ns > 0.05, $^{*}p < 0.05$, $^{**}p < 0.01$, $^{***}p < 0.001$, and $^{****}p < 0.0001$.

positive influence of fibrin on the production of elastin fibers.[23] A further strategy to overcome the lack of elastin production was suggested by L'Heureux and colleagues who used fibroblasts instead of SMCs.[31] Alternatively, also the employment of bone marrow-derived smooth muscle progenitor cells might increase elastin deposition.[32] Additionally, it is possible to directly incorporate elastin as a textile component by electrospinning or as well by introducing elastin-like recombinamers into the molding gel.[33–36]

In conclusion, the regulation of elastin production, as an important structural element in TEVGs, is still an issue of discussion, and our imaging approach opens an attractive opportunity to study this process longitudinally in intact TEVGs.

In contrast to the lack of elastin in our TEVGs, a hyperintense signal was observed for the collagen type I binding probe EP-3533 (Figure 5c) and confirmed by T1 relaxometry (R1 precontrast agents: (0.4 ± 0.1) s^{-1}; R1 post-EP-3533: (0.6 ± 0.1) s^{-1}; R1 post-Magnevist: (0.4 ± 0.1) s^{-1}). Furthermore, histological analyses were performed to investigate the presence of collagen type I and type IV by immunofluorescence, and total collagen via Masson's trichrome staining. Immunofluorescence microscopy confirmed the abundant deposition of collagen fibers

within our TEVGs, which visually appeared comparable to collagen deposition in HUA. Moreover, we also investigated early collagen type I deposition by histology and confirmed its presence after 3 days of bioreactor maturation of our TEVGs (Figure S3, Supporting Information). These findings are in line with previous studies, demonstrating enhanced collagen production by SMCs when TEVGs' in vitro maturation is carried out under dynamic conditions.[37,38] MR imaging was also performed on HUA samples (Figure 5e–f) to confirm the validity and functionality of our imaging approach. For both ESMA and EP-3533, a high and statistically significant increase in signal intensities was found, which was absent for Magnevist. The signal changes in the MR images could be confirmed by relaxometry (R1 precontrast agents: (0.5 ± 0.003) s^{-1}; R1 post-ESMA: (1.5 ± 0.04) s^{-1}; R1 post-EP-3533: (0.6 ± 0.03) s^{-1}; R1 post-Magnevist: (0.5 ± 0.08) s^{-1}). Furthermore, to investigate the MRI sensitivity to the evaluated targeted probes, we introduced known amounts of collagen type I and elastin in the fibrin molding gel, respectively. The ESMA and EP-3533 R1 values correlate linearly with elastin and collagen type I amounts within the employed the acellularized scaffold (Figure S4, Supporting Information). Our data are supported by previous studies, in which the linear correlation be-
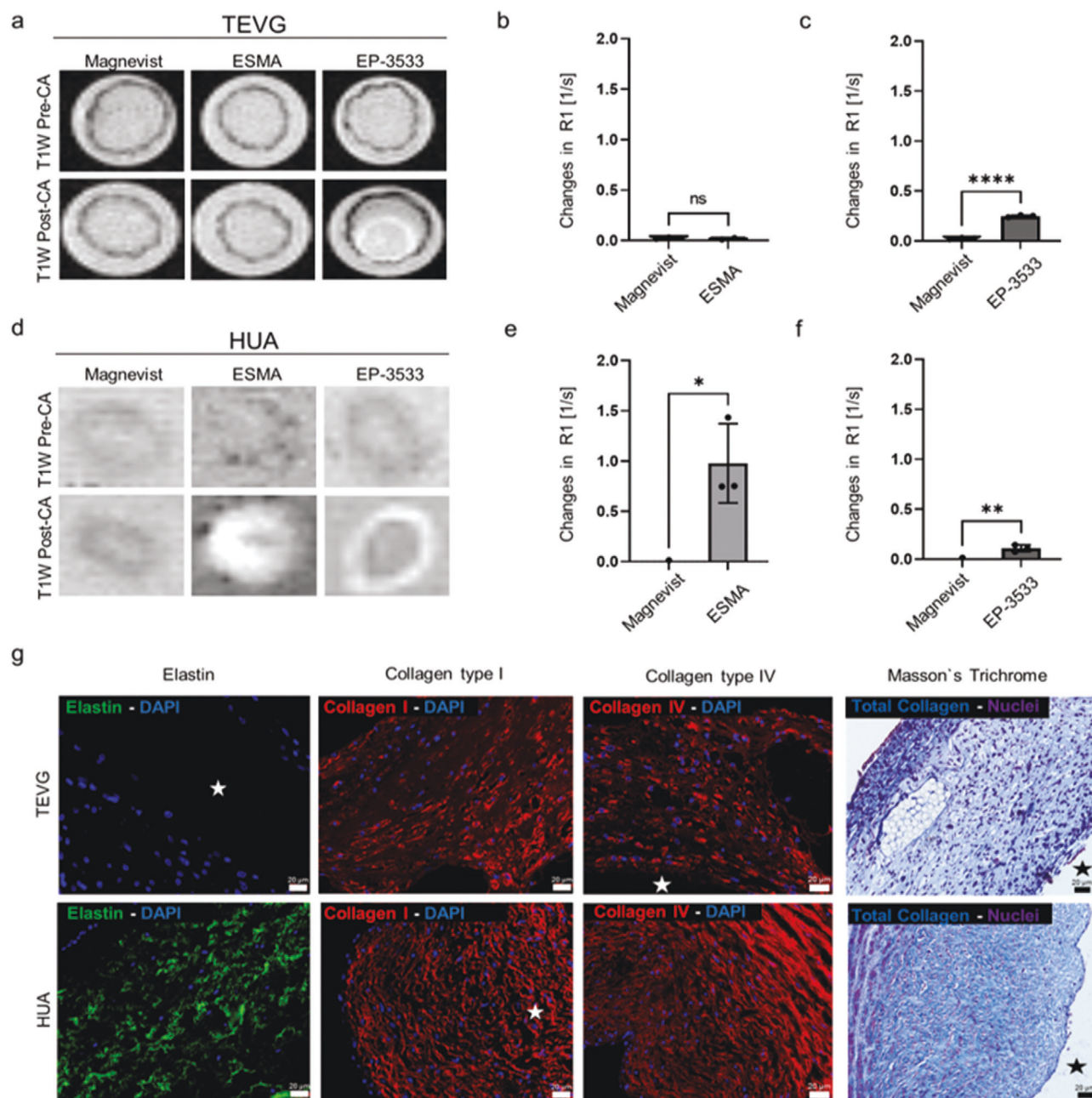
Figure 5. MRI investigation of ECM deposition in TEVGs and HUA. a) T1 weighted MRI images of TEVGs before (top) and after injection (bottom) of ESMA, EP-3533, and Magnevist. b) Changes in R1 values were obtained by subtracting the pre- from the post-injection values. R1 relaxometry of TEVGs do not markedly change after injection of ESMA. c) Compared to Magnevist, R1 values of TEVGs significantly change after injection of EP-3533. d) MRI images of HUA (positive control) before (top) and after (bottom) injection of ESMA, EP-3533, and Magnevist. e,f) R1 relaxometry of HUA after ESMA and EP-3533 injection indicate the specificity of the probes to their targets. g) Representative histological images of TEVGs (top) and HUA (bottom) showing elastin (green), collagen type I (red), collagen type IV (red) by immunofluorescence, and total collagen (blue) via Masson's trichrome staining. No elastin deposition, but an abundant deposition of collagen (including type I and IV) is detectable in TEVGs. All values were obtained in triplicates: mean ± SD; t-test with Tukey post hoc correction test was applied; ns > 0.05, $^*p < 0.05$, $^{**}p < 0.01$, $^{***}p < 0.001$, and $^{****}p < 0.0001$. The star indicates TEVGs' and HUA's lumen.

tween R1 values and ESMA or EP-3533 fraction bound to elastin or collagen type I has already been shown, e.g., by ICP-MS, by Western blot, and by staining and Gd analysis.[27,39,40] Consequently, molecular MRI proved to be an efficient tool to characterize the deposition and remodeling of the two main ECM components in TEVGs in vitro. Thus, the highly sensitive evaluation of ECM deposition during the in vitro conditioning of the vascular prostheses might represent a fundamental step forward to predict and ameliorate the host's outcomes upon in vivo implantation.

ADVANCED
SCIENCE NEWS
www.advancedsciencenews.com

ADVANCED
SCIENCE
Open Access
www.advancedscience.com

2.3. Molecular Ultrasound Imaging Assesses Endothelial Integrity and Inflammation

$\alpha_v\beta_3$ integrin is an important marker of inflammation and thrombus formation. This integrin directly interacts with $\alpha_{IIb}\beta_3$ integrins on platelets and plays a role in several pathways leading to hyperplasia of the intima and, thus, stenosis of vascular grafts.[39] It has been shown that, especially after the disruption of endothelial coverage, $\alpha_v\beta_3$ expression increases and induces strong SMCs proliferation toward the inner lumen of the vessel.[40–42]

Therefore, $\alpha_v\beta_3$ integrin expression is an excellent marker of endothelial dysfunction in our TEVGs. We decided to assess $\alpha_v\beta_3$ integrin expression by molecular US imaging as it is noninvasive and easily applicable in vitro and in vivo. Furthermore, even if the entire endothelial layer is destroyed, luminal availability of $\alpha_v\beta_3$ integrin is still preserved by activated SMCs. Thus, $\alpha_v\beta_3$ integrin expression would still indicate failures in the endothelialization of TEVGs. Molecular US imaging in TEVGs showed comparable MB binding signal between c[RGDfK]-MB and c[RADfK]-control MBs (**Figure 6**a), indicating no integrin expression. The competitive binding experiment, performed at all three observation time points confirmed this result (Figure 6b). MB binding was investigated and acquired in nonlinear contrast mode (NLC), which removes all the linear response from tissue signal from the quantification process and allows a highly accurate quantification of molecular biomarkers. The final values obtained after quantification were expressed as differential targeted enhancement (d.T.E.). The linear correlation between US signals and MBs concentrations was also evaluated in phantoms reaching a correlation coefficient of R2 = 0.9905 (Figure S5, Supporting Information). The lack of $\alpha_v\beta_3$ integrin expression in our TEVGs might be due to the absence of the complement system precursors and the different types of immune system cells. Furthermore, in line with our findings, it has been shown that $\alpha_v\beta_3$ integrin is minimally expressed on resting endothelium, and its upregulation is induced by mechanical endothelial denudation, shear stress, growth factors, and cytokines.[43]

Therefore, TNF-α, one of the major inflammatory cytokines, was used to increase $\alpha_v\beta_3$ integrin expression in our TEVGs to mimic a situation of endothelial dysfunction.[44] TNF-α treated TEVGs showed an increased c[RGDfK]-MB binding in comparison to c[RADfK]-control MBs and a decreased binging after competitive blocking of $\alpha_v\beta_3$ integrins (Figure 6a,c). Furthermore, the preactivation of cells with TNF-α led to a 70-fold increase in c[RGDfK]-MBs binding compared to the untreated TEVGs (d.T.E. for c[RGDfK]-MB in untreated TEVGs: 0.1 ± 0.1 versus in TNF-α treated TEVGs: 6.9 ± 2.3).
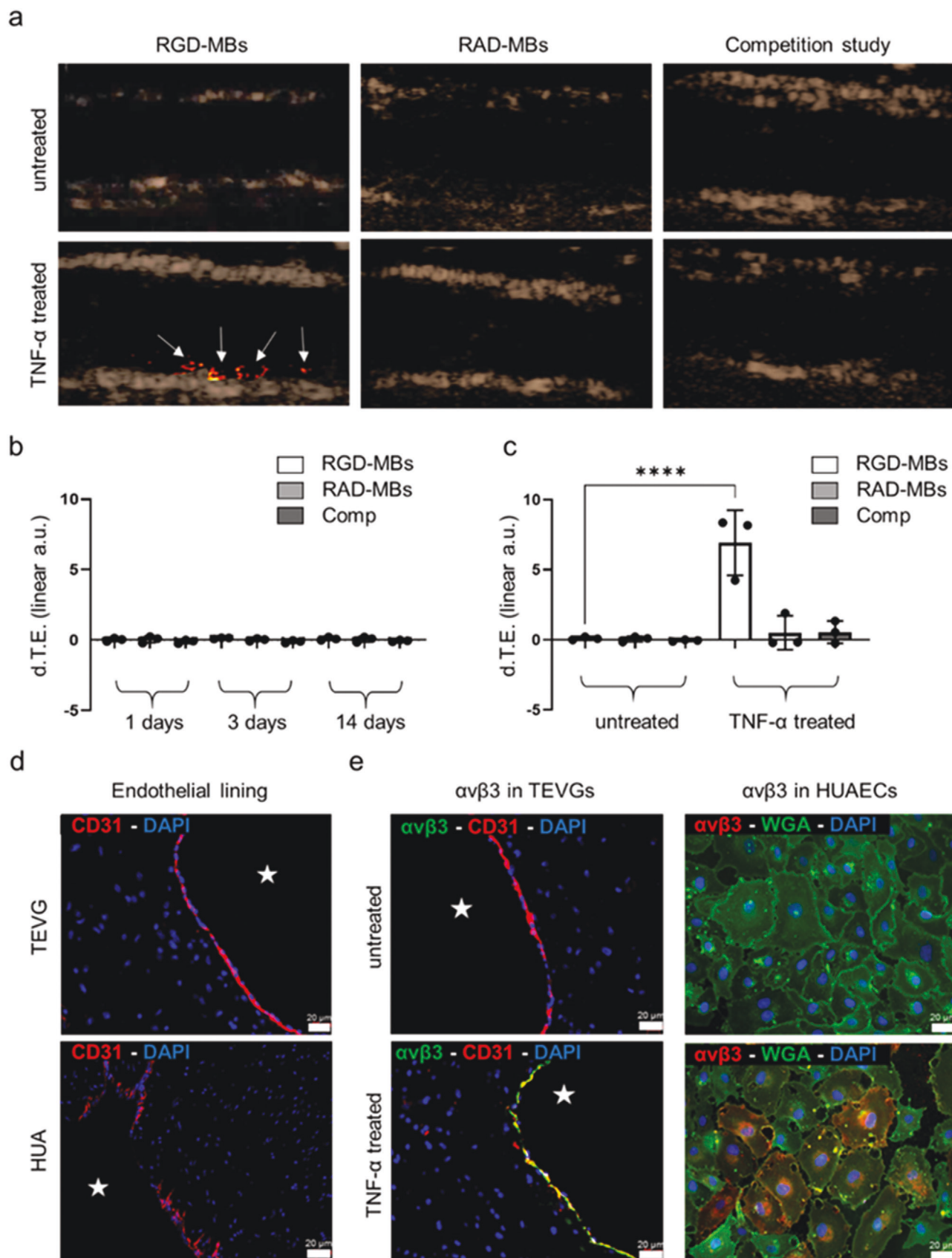
Subsequently, immunofluorescence analyses were performed to evaluate the endothelial coverage and $\alpha_v\beta_3$ integrin expression in TEVGs (Figure 6d–e). Histology confirmed the presence of a continuous endothelial layer and the $\alpha_v\beta_3$ integrin expression by ECs only in TNF-α treated TEVGs (Figure 6e). To further investigate the basal expression level of $\alpha_v\beta_3$ integrin, histological analyses were performed on 2D cultured human umbilical artery endothelial cells (HUAECs), shown in Figure 6e, and on HUA, serving as positive controls (Figure S6, Supporting Information). In line with the TEVGs, the 2D cultured HUAECs did not express $\alpha_v\beta_3$ integrins prior to TNF-α activation. In contrast, HUA samples physiologically expressed $\alpha_v\beta_3$ integrins, even in absence of

ongoing inflammatory reactions. Subsequently, we can conclude that the bioreactor design that kept shear stress low as well as the dynamic flow conditions applied for the in vitro maturation of our TEVGs' might have caused only shallow levels of distress to the ECs being not sufficient to stimulate $\alpha_v\beta_3$ integrin expression. Moreover, there might be a possible correlation between the lack of integrins and elastin in our TEVGs. It is well known that the integrin system, especially $\alpha_v\beta_3$ integrins, physiologically influences the cytoskeleton remodeling through a complex interplay of signaling pathways.[45–47] The cytoskeleton remodeling has also been achieved in vitro by repeated stretching cycles and, thus, stressing of SMCs resulting in higher production and deposition of elastin.[48] Therefore, several studies on the matter seem to suggest that the absence of integrins, which modulate the stretching of cellular components and ECM formation in response to physiological pulsatile flow and pressure, might result in impaired ECM deposition, i.e., the lack of elastin.

Consequently, here we show that the employment of MRI and molecularly targeted US efficiently enables the noninvasive longitudinal monitoring of scaffold resorption, ECM remodeling, and endothelial integrity. Evaluating these aspects before and after the implantation of vascular grafts is fundamental to ensure their integrity and functionality. The application of MRI in tissue engineering has several advantages, such as excellent imaging penetration depth as well as superior soft-tissue contrast, providing anatomical, functional, and cellular information. Furthermore, MRI is an imaging technique routinely applied for clinical investigations. Here, the direct labeling of the textile scaffold with MRI contrast agents, such as SPIONs, holds great translational potential as five SPION agents are already clinically approved.[49] Alternatively, labeling scaffolds with ^{19}F MRI might represent a valuable addition to ^{1}H MRI. For example, ^{19}F-labeled compounds can be used to label cells and synthetic polymers with a sufficient number of highly mobile ^{19}F atoms can be applied as parts of the scaffold material.[50,51]

Gadolinium-based MR contrast agents are the most used ones in clinics. However, there are always concerns about the release of gadolinium from the chelate complexes and potential resulting adverse effects.[52] As the persistence of these agents in the body correlates with gadolinium release, the use of these molecular MRI probes is considered particularly critical. Nevertheless, new MRI probes were designed to detect mesenchymal stem cell activity, ECM deposition, and remodeling via matrix metalloproteinases, showing promising results.[26,27,53,54] Concerning the agents used in this study, we can say that the pharmacokinetic properties and Gd-release kinetics of ESMA and EP-3533 were already tested and appear acceptable.[55,56] Furthermore, even if the agents cannot be approved for MRI, there is still the option to entrap radiometals in the chelate complexes and use them for SPECT or PET imaging as an attractive clinical alternative.

X-ray and CT have been extensively used to characterize and assess tissue-engineered scaffold properties as porosity and integrity.[57–59] For instance, CT imaging might be applied to monitor the degradation of acellularized vascular graft scaffolds by assessing the changes in volume and density, or combined with other imaging modalities, such as positron emission tomography (PET), to localize and quantify vascular inflammation.[4,58] Nonetheless, CT does not represent an ideal tool for the noninvasive imaging of vascular implants compared

2105783 (9 of 15)

**ADVANCED
SCIENCE NEWS**

www.advancedsciencenews.com

**ADVANCED
SCIENCE**
Open Access

www.advancedscience.com

with MRI, mainly because of lower tissue contrast and radiation exposure.[60]

US is another valuable imaging tool to monitor vascular grafts' functionality in vitro and in vivo. It provides excellent temporal resolution and reasonable tissue penetration. US can be used to assess vessel wall integrity and patency of vascular implants or to evaluate the endothelial coverage, atherosclerotic plaque formation, and inflammatory reaction through the employment of targeted contrast agents, the latter being already clinically employed or currently under clinical trial.[14,61–63]

In addition to $\alpha_v\beta_3$ integrins imaging, which was carried out in our study, other targeting ligands might be suitable for the detection of endothelial lining integrity or distress. For instance, major endothelial markers of inflammation, such as P-selectin, von Willebrand factor (VWF), vascular endothelial growth factor (VEGF) receptors, vascular cell adhesion molecule 1 (VCAM-1), and intercellular adhesion molecule 1 (ICAM-1), have been extensively explored during the investigation of cardiovascular diseases as early detection of atherosclerotic plaque.[64–70] Furthermore, Curaj et al. showed the high sensitivity of junctional adhesion molecule A (JAM-A) functionalized MB for the US detection of transient endothelial activation, which could be an important early indicator of endothelial distress in the TEVGs.[71]

3. Conclusion

In this manuscript, we present a comprehensive imaging approach to characterize TEVGs noninvasively and nondestructively. This includes the visualization of textile scaffold components, ECM deposition, and the assessment of endothelial integrity. In detail, we propose the incorporation of SPION into PLGA fibers to efficiently monitor their degradation by MRI both in vitro and in vivo. Indeed, the subcutaneous implantation of our TEVGs into a rat model provides an initial proof-of-concept for the in vivo detection and longitudinal evaluation of our SPION-labeled PLGA fibers. Furthermore, we show that using the same imaging modality, both elastin and collagen type I deposition can be effectively assessed providing valuable insights into the maturation and remodeling of the TEVGs. We also demonstrate that molecularly targeted US is an efficient tool for the assessment of endothelial dysfunction that may result in hyperplasia of the intima, thrombus formation, and loss of patency of the vascular grafts. Consequently, our imaging approach might strongly support quality control in the critical transition phase between late in vitro bioreactor maturation and early in vivo implantation of cardiovascular implants and thus, foster their clinical translation.

Table 1. Process parameters of the warp-knitting process of the tubular PVDF grafts.

Graft area	Warp-knitting chain notation	Effective arcs per cm (EAC) value
Front side	2/4-2-2-2-0-2-2-2-4-2-2-2-0-2/2///	EAC 6
Back side	2/2-2-0-0-2-2-2-4-2-2-2-0-0-2-2-2/4///	EAC 6
Brim fibers	0-2-2-2-2-2-0-2-0-2-2-2-2-2-0/2/// 0-0-2-0-2-0-0-0-0-0-2-0-2-0-0-0///	EAC 6

4. Experimental Section

Synthesis of Oleic Acid-Coated SPION: Oleic acid-coated SPION were synthesized by thermal decomposition according to a previously established protocol.[72,73] Purified iron (III) oleate precursor (8 mmol) and oleic acid (58.4 mmol) were dissolved in 1-octadecene (50 mL) in a three-neck round-bottom flask insulated with glass wool and aluminum foil. The ratio of oleic acid to precursor was kept constant at 7:3. Then, the mixture was heated to 100 °C and maintained at this temperature without reflux to evaporate residual water. After degassing and fitting a reflux cooler, the reaction mixture was heated further to 340 °C with a heating rate of 3 °C min⁻¹ under argon atmosphere and aged at the same temperature for 3 h. After cooling down the sample to room temperature, the sample was transferred to 50 mL Falcon tubes, and acetone was added. To assist the deposition of nanoparticles and to increase the extraction of impurities from the solvent, the sample was kept at 50 °C in a water bath for 5 min and then sonicated for 5 min. The sample was centrifuged, and the supernatant was discarded. Then, the nanoparticles were dispersed in a mixture of hexane and methanol with a ratio of 1:6. The mixture was centrifuged, and the washing of the sample was repeated three more times with hexane and methanol. In the end, the washed nanoparticles were dispersed in hexane. After the addition of one drop of oleic acid, the final sample was stored at 4 °C until further use.

PVDF Mesh Production: By using PVDF (Lenzing Plastics GmbH & Co. KG, Lenzing, Austria) multifilament fibers (150 dtex, 48 filaments), three different tubular graft structures were produced using a double-bar raschel warp-knitting machine (Karl Meyer Holding GmbH & Co. KG, Obertshausen, Germany). The number of fibers was altered (4, 6, and 10 fibers) to achieve different inner diameters of the resulting round knitted mesh structures. The warp-knitting process parameters are stated in **Table 1**.

Electrospinning of SPION-Labeled PLGA Fibers: The warp-knitted grafts were coated by electrospun PLGA (Purasorb PLG 8523, Corbion Purac Gorinchem, Netherlands) fibers labeled with SPION. All spinning procedures were performed using a coaxial spinning head (Bioinicia SL, Paterna, Spain) with two coaxial arranged steel capillaries with inner diameters of 1400 μm (shell capillary) and 580 μm (core capillary). SPION-labeled PLGA fibers were spun at a voltage of +22 kV (emitter) and −20 kV (collector). The electrospinning of the fibers was performed at 25 °C and 30% of humidity. Three different spinning solutions were produced, including 6% (w/w) PLGA (shell solution), 6% (w/w) PLGA labeled with 0.2% (w/w) SPION (core solution), and 6% (w/w) PLGA labeled with

---

Figure 6. Molecular US imaging of $\alpha_v\beta_3$ integrin expression. a) Contrast mode ultrasound images are shown with a color-coded overlay of the d.T.E., the latter indicating bound MBs (white arrows). While there is hardly any c[RGDfK]-MB binding in untreated TEVGs (top), TNF-α treatment of TEVGs results in a strong (bottom) c[RGDfK]-MB attachment to the inner lumen of the TEVGs. In both, untreated and TNF-α treated TEVGs no significant binding was observed after the injection of control c[RADfK]-MB, and the injection of c[RGDfK]-MB after blocking integrins with free c[RGDfK], respectively. b) Quantitative analysis of molecular US imaging data acquired at 1, 3, and 14 days of TEVGs' bioreactor conditioning. c) Comparison between c[RGDfK]-MB binding in TNF-α treated and untreated TEVGs. d) Immunofluorescence histology of ECs (red) in TEVGs and HUA to evaluate the endothelial lining integrity and continuity. e) Immunofluorescence images of $\alpha_v\beta_3$ integrin expression in untreated (top) and TNF-α treated (bottom) TEVGs and HUAECs. In TEVGs, histology shows colocalization of $\alpha_v\beta_3$ (red) with CD31 (green) only after TNF-α injection. The basal level of $\alpha_v\beta_3$ integrin expression is investigated in HUAECs. Only after TNF-α treatment, HUAECs show colocalization of $\alpha_v\beta_3$ (red) with wheat germ agglutinin (WGA) (green), indicating the cells' nonactive phenotype. All values were obtained in triplicates: mean ± SD; *t*-test with Tukey post hoc correction test was applied; ns > 0.05, $^*p$ < 0.05, $^{**}p$ < 0.01, $^{***}p$ < 0.001, and $^{****}p$ < 0.0001. The star indicates TEVGs' and HUA's lumen.

**ADVANCED
SCIENCE NEWS**

www.advancedsciencenews.com

**ADVANCED
SCIENCE**
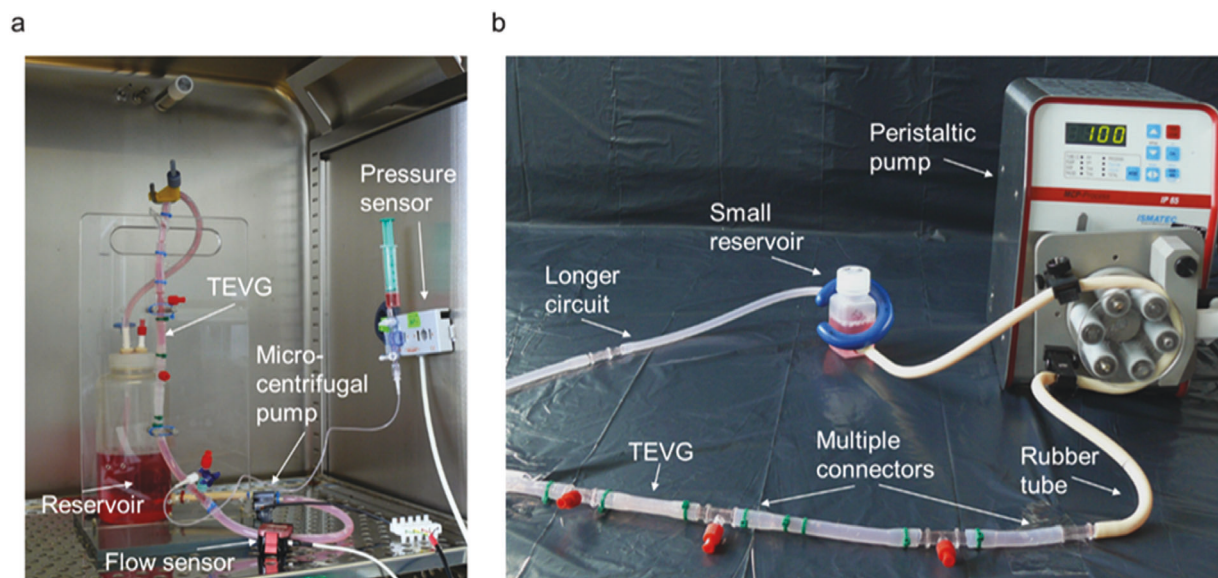Open Access

www.advancedscience.com

Figure 7. Visual display of the custom-made bioreactor modifications. a) The closed bioreactor circuit was connected to a 500 mL medium reservoir, a micro-centrifugal pump, and to pressure and flow sensors. b) Later, the bioreactor circuit was equipped with longer silicon and rubber tubes, a small medium reservoir fitting into the 7T MRI, and a peristaltic pump so that TEVGs were easily insertable and removable during the imaging procedure.

0.4% (w/w) SPION (core solution) dissolved in methanol (MeOH, neoLab Migge Laborbedarf – Vertriebs GmbH, Heidelberg, Germany) and chloroform (CHCl$_3$, Carl Roth GmbH & Co. KG, Karlsruhe, Germany). Each spinning solution was prepared (10 mL) and stirred for 24 h until the PLGA was completely dissolved. The SPION solution was added to the core solution shortly before the execution of the electrospinning process and mixed gently until reaching a homogenous solution. For coating of the PVDF grafts, the core of the coaxial spinning head was loaded with the core solution and the shell solution was loaded into the shell of the coaxial spinning head, respectively. For each coating procedure, a PVDF graft (30 cm) was put on a cylindrical collector (tip to collector distance of 20 cm). The spinning head was moved continuously along the entire length of the graft during the spinning process with a speed of 30 mm s^{-1}. Coating was performed on different samples for 10 or 30 min. The flow rates of the core and shell solution were set to 0.5 and 1 mL h^{-1} during the spinning process.

Biohybrid Tissue-Engineered Vascular Graft Production and Bioreactor Conditioning: The molding of the vascular graft was performed inside a silicon tube (6.4 mm inner diameter) (Carl Roth GmbH, Germany). A metal rod (3 mm diameter) surrounded by the textile scaffold was inserted as a core. Subsequently, the matrix solution was injected into the molding cavity. The matrix solution consisted of fibrinogen (10 mg mL^{-1}) (Calbiochem, Darmstadt, Germany), thrombin (40 U mL^{-1}) (Sigma, Steinheim, Germany), tris buffer, CaCl$_2$ (50 ×10^{-3} M) (Sigma, Steinheim, Germany) and human arterial smooth muscle cells (10^7 cells mL^{-1}). The metal rod was removed after the molding, and human arterial endothelial cells (10^6 per cm graft) were injected into TEVG's lumen for the endothelialization process.

Subsequently, TEVGs were conditioned in a bioreactor system consisting of a silicon tube closed circuit containing the vascular graft and a medium reservoir (500 mL) (**Figure 7**a). The dynamic flow of the medium within the system was provided by a micro-centrifugal pump (Rs Pro, Corby, United Kingdom) and the generated flow and pressure were monitored by a flow sensor (Em-tec GmbH, Finning, Germany) and a pressure sensor (Codan GmbH, Lensahn, Germany). To enable multimodal imaging at the same time, the bioreactor was modified (Figure 7b). The silicon tube system was elongated by multiple connectors and rubber tubes (Saint-Gobain, Herzogenrath, Germany), the micro-centrifugal pump was replaced by a peristaltic pump (MCP Process, Ismatec, Cole Parmer GmbH, Germany), and the medium reservoir was substituted with a smaller bottle (50 mL) to fit into the 7T MRI.

Enhancing the PLGA Fibers Detectability by SPION Labeling: MRI phantoms were produced by embedding two different concentrations of SPION-labeled PLGA fibers (0.2% and 0.4%) in 10% gelatin (w/v) and compared to unlabeled ones used as a negative control. Subsequently, both 0.2% and 0.4% of SPION-labeled PLGA fibers were analyzed in combination with the PVDF tubular structure. Moreover, the electrospinning time for the production of the PLGA coating layer upon the PVDF meshes was also investigated to assess whether longer coating time might influence the MRI visibility of the fibers. Next, the phantoms were measured in a Bruker BioSpec 70/20 USR 7T MRI scanner (Bruker BioSpin GmbH, Germany) using a ^{1}H transmit-receive volume coil with active detuning with an inner diameter of 82 mm and a bore length of 112 mm.

Initially, shimming based on B0 field mapping was performed to reduce the nonlinear image distortions due to the inhomogeneities of the static magnetic field (B0).

Transverse relaxation times (T2) were measured using a 2D multi-slice, multi-echo spin-echo (MSME) sequence with a 90° excitation pulse followed by a train of equally spaced 180° refocusing pulses [repetition time (TR) = 2000 ms; echo time (TE) = 20 ms; echo spacing = 20 ms; echo images = 30; number of averages = 4; matrix size = 150 × 150; FOV = (35 × 20) mm^2; slice thickness = 1 mm].

T2* relaxation times were measured using a multiple gradient echo (MGE) sequence [TR = 800 ms; TE = 4.5 ms; echo spacing = 5.5 ms; echo images = 30; number of averages = 6; flip angle = 50°; matrix size = 150 × 150; FOV = (35 × 20) mm^2; slice thickness = 1 mm].

T2 and T2* relaxation times and the respective R2 and R2* relaxation rates were calculated by fitting an exponential curve to the signal amplitudes as a function of the echo time (TE) for each segmented region of interest (ROI) obtained by using the Imalytics Preclinical Software (Gremse-IT GmbH, Aachen, Germany). The fitting of the exponential curve was performed by using Equation (1)

$$M = M_0 \; e^{-\frac{TE}{T2}} + C \qquad (1)$$

in which an offset (C) was included to account for a signal plateau created by noise or a component with slow signal decay. R2 and R2* were calculated as the inverse of T2 and T2*, respectively.

Moreover, T2- and T2*- weighted images were acquired using a T2-weighted fast spin echo sequence [TR = 3878 ms; TE = 80 ms; echo spac-

2105783 (11 of 15)

ADVANCED
SCIENCE NEWS

www.advancedsciencenews.com

ADVANCED
SCIENCE
Open Access

www.advancedscience.com

ing = 40 ms; acceleration factor = 4; matrix size = 360 × 150; FOV = (35 × 20) mm^2; slice thickness = 1 mm] and a T2*-weighted gradient echo sequence [TR = 907 ms; TE = 30 ms; flip angle = 18°; matrix size = 360 × 150; FOV = (35 × 20) mm^2; slice thickness = 1 mm], respectively.

Longitudinal MRI Monitoring of the PLGA Fiber Degradation Rate: SPION-labeled and unlabeled control fibers were embedded in fibrin phantoms. The fibrin gel consisted of fibrinogen (1 mL) (Merck KGaA, Darmstadt, Germany) dissolved in TBS (10 mg mL^{-1}), thrombin (150 μL) (Merck KGaA, Darmstadt, Germany), aprotinin (20 U mL^{-1}) (Abcam, Berlin, Germany), and CaCl$_2$ (150 μL) (Sigma, Steinheim, Germany). Fibrin phantoms were imaged using the 7T MRI scanner for a total duration of 11 weeks. The samples were incubated at 37 °C for the first 8 weeks and at 70 °C until the end of the experiment to accelerate the degradation of the PLGA.

In addition, PLGA degradation was monitored in combination with the PVDF tubular structures. For this purpose, PVDF filaments coated with PLGA were incubated in PBS at 37 °C for 3 weeks. The same MRI sequences as for the gelatin phantoms were employed for the acquisition of T2-/T2*-weighted images and T2/T2* relaxation times. Colormaps were obtained using Imalytics Preclinical Software (Gremse-IT GmbH, Aachen, Germany) and by superimposition of the calculated R2 colormap onto the corresponding T2-weighted image.

Assessment of PLGA Degradation in Complete TEVGs: TEVGs were longitudinally studied by 7T MRI over a period of 7 days to investigate whether the degradation of SPION-labeled PLGA fibers was influenced by the presence of cells. TEVGs were monitored immediately after endothelialization of the lumen of the vascular graft as well as after 3 and 7 days, respectively.

T2 relaxometry was performed using a MSME sequence [TR = 5600 ms; TE = 20 ms; echo spacing = 20 ms; echo images = 30; number of averages = 4; matrix size = 150 × 150; FOV = (35 × 20) mm^2; slice thickness = 1 mm] and Equation (1) was used for the fitting of the exponential curve. The shown R2 colormaps were calculated and obtained as for the previous studies.

In Vivo Longitudinal MRI Evaluation of PLGA Degradation in TEVGs: A total of six inbred male Lewis rats (Janvier Labs, Le Genest-Saint-Isle, France), aged 12 weeks, were used. The animal experiments were approved by the governmental review committee on animal care (Landesamt für Natur, Umwelt und Verbraucherschutz Nordrhein-Westfalen, LANUV, NRW). Under general (Isoflurane, 2% in O$_2$) and local anesthesia (Ropivacaine 2 mg kg^{-1}), each rat underwent a surgical procedure, which consisted of the subcutaneous implantation of 1 cm of SPION-labeled TEVG on the left side and 1 cm of unlabeled control on the right side of the dorsum. The cells incorporated into both SPION-labeled and unlabeled TEVGs were obtained by previously sacrificing one Lewis rat, which was used as a cell donor to avoid immunogenicity. On days 1, 7, 14, and 21 post-implantation, the MRI investigation was performed under isoflurane anesthesia using a 7T MRI equipped with a ^{1}H transmit-receive volume coil with active detuning. One animal each was sacrificed after days 7 and 14, and the remaining three at day 21 to allow further ex vivo histological analyses. Anatomical T2- and T1-weighted images were acquired by using a T2-weighted fast spin echo sequence [TR = 1300 ms; TE = 25 ms; echo spacing = 8.3 ms; acceleration factor = 8; matrix size = 180 × 180; FOV = (50 × 60) mm^2; slice thickness = 1 mm] and a T1-weighted fast spin echo sequence [TR = 200 ms; TE = 2.9 ms; flip angle = 30°; matrix size = 180 × 180; FOV = (50 × 60) mm^2; slice thickness = 1 mm], respectively. T2 relaxometry was performed using a MSME sequence [TR = 4445 ms; TE = 7 ms; echo spacing = 20 ms; echo images = 40; number of averages = 1; matrix size = 144 × 112; FOV = (50 × 60) mm^2; slice thickness = 1 mm].

Molecular MRI of Elastin and Collagen in Tissue-Engineered Vascular Grafts: To study the production and deposition of the extracellular matrix, ESMA (Lantheus Medical Imaging, North Billerica, Massachusetts, USA) and EP-3533 (Collagen Medical LLC, Belmont, Massachusetts, USA) were used molecular MRI probes to assess elastin and type I collagen deposition, respectively. Both MRI probes were compared to the nonspecific clinical contrast agent Gd-DTPA (Magnevist, Bayer, Germany).

TEVGs were measured with 7T MRI after 14 days of bioreactor conditioning. Following the acquisition of T1 relaxation times, the nonspecific

contrast agent Gd-DTPA (0.3 mmol mL^{-1}) was injected into the bioreactor with a peristaltic pump (MCP-Process, Ismatec, Cole-Parmer GmbH, Germany) at a constant flow rate of 0.5 mL min^{-1} and circulated at room temperature for 1 h, followed by washing with fresh cell medium (Lonza Bioscience, North Carolina, United States) for 1 h. Then, another T1 relaxometry measurement was performed to assess the change in T1 relaxation time. On the same TEVGs, the procedure was repeated for ESMA (0.2 mmol mL^{-1}) and EP-3533 (10 μmol mL^{-1}), respectively.

T1 relaxation times were acquired using a fast spin echo sequence with static TE and variable TR [number of T1 Experiments = 6; TR = 5000–275 ms; TE = 12 ms; acceleration factor = 4; echo spacing = 6 ms; number of averages = 1; matrix size = 100 × 100; FOV = (10 × 10) mm^2; slice thickness = 1 mm]. T1 was calculated by fitting an exponential curve to the signal amplitudes as a function of the TR for each segmented ROI obtained by using the Imalytics Preclinical Software (Gremse-IT GmbH, Aachen, Germany). The fitting of the exponential curve was performed by using Equation (2)

$$M = M_0 \left(1 - e^{-\frac{TR}{T1}} \right) \qquad (2)$$

Moreover, T1-weighted images were acquired using a fast spin echo sequence [TR = 150 ms; TE = 2.9 ms; flip angle = 50°; matrix size = 100 × 100; FOV = (50 × 60) mm^2; slice thickness = 1 mm] In addition, the three molecular MRI probes were applied on HUA serving as positive controls regarding the presence of elastin and type I collagen. The employment of human samples used throughout this study was performed in compliance with the Ethical Committee approval (278/16).

PBCA MB Synthesis and Coupling of Peptides: PBCA MBs were synthesized based on a previously described protocol.[74,75] Triton X-100 (3 mL) (Sigma-Aldrich, Darmstadt, Germany) was dissolved in distilled water (300 mL) via means of a magnetic stirrer. The pH of the solution was decreased to 2.5 by dropwise addition of hydrochloric acid (1 M). Subsequently, butyl cyanoacrylate (BCA) (Special polymers Ltd., Sofia, Bulgaria) (3 mL) was added dropwise to the aqueous solution and homogenized at 10 000 rpm by using an Ultra-Turrax T-50 (IKA Werke GmbH & Co. KG, Staufen, Germany) for 1 h. The emulsion was then transferred into Falcon tubes (50 mL), centrifuged at 500 rpm to remove the debris for 20 min, and washed three times with 0.02% Triton X-100 aqueous solution. The size and concentration of the MBs were determined using a Coulter counter (Multisizer 4e, Beckman Coulter Life Sciences, Indiana, USA). For each measurement, the MBs (2 μL) were dispersed in ISOTON II diluent (20 mL) (Beckman Coulter). Based on a previously established protocol, MBs' surface was functionalized with biotinylated c[RGDfK] and c[RADfK] peptides (Vivitide, Gardner, Massachusetts, USA), the MBs were hydrolyzed with NaOH (0.1 N, pH 11) at room temperature under constant rotation at 40 rpm for 15 min.[76] Then, hydrochloric acid (1 M) was used to decrease the pH to 2.5–3. The MBs were centrifuged at 500 rpm for 20 min and washed with 0.02% Triton X-100 aqueous solution. A second solution of 1-ethyl-3-(3-dimethylaminopropyl) carbodiimide (10 mg) (Carl Roth GmbH, Karlsruhe, Germany) mixed with triethanolamine (2 μL) (Acros Organics, Schwerte, Germany) was prepared in a glass vial using a magnetic stirrer. MBs were added to this solution and, after 30 s of stirring, streptavidin (1 mg mL^{-1}) was added. After stirring at 150 rpm at room temperature for 1 h, the mixture was kept at 4 °C for 12 h. Then, in presence of 0.02% HEPES (4-(2-hydroxyethyl)-1-piperazineethanesulfonic acid) buffer, the MBs were washed by 3 centrifugation steps at 500 rpm for 20 min. Subsequently, they were mixed with biotinylated c[RGDfK] or c[RADfK] at room temperature under constant rotation at 40 rpm for 15 min, and again washed with 0.02% Triton X-100 aqueous solution.

Molecular Ultrasound Imaging of TEVGs: US imaging was performed using a VEVO 3100 ultrasound system equipped with a linear-array-MX-250 transducer (FUJIFILM VisualSonics, Toronto, Ontario, Canada). To enable the specific binding of c[RGDfK]-functionalized MBs in the TEVGs under flow conditions, the modified bioreactor circuit was placed horizontally on the ultrasound table. Then, the transducer was placed transversally onto the silicone tube containing the TEVGs to obtain sagittal images of the lumen of the graft. The flow rate was maintained constant at

**ADVANCED
SCIENCE NEWS**

www.advancedsciencenews.com

ADVANCED SCIENCE
Open Access

www.advancedscience.com

0.5 mL min^{-1} using a peristaltic pump. The accumulation of c[RGDfK]-functionalized MBs was compared with c[RADfK]-functionalized ones, the latter serving as negative controls. Furthermore, a competitive binding experiment was performed by injecting free c[RGDfK] prior to the injection of c[RGDfK]-functionalized MBs in access. c[RADfK]-functionalized MBs (1×10^9 MB mL^{-1}) were injected into the medium reservoir of the bioreactor circuit, and the inflow of the MBs was imaged in NLC mode at 18 MHz frequency, 4% power, and 500 frames were acquired. The MBs were circulated for 8 min. Subsequently, the medium with the unbound MBs was removed, the TEVGs were washed with sterile DPBS, and fresh medium was added. 500 frames were recorded at 4% power and 18 MHz frequency, and a 100% power destructive pulse was applied after 250 frames to destroy the bound MBs. The same procedure was repeated for the c[RGDfK]-functionalized MBs and the competitive binding experiment. For quantifying the contrast intensity given by target-bound MBs, ROI were drawn using the VevoLAB software version 3.2 (FUJIFILM VisualSonics, Toronto, Ontario, Canada). Subsequently, the d.T.E. was calculated by subtracting the signal before and after MB destruction.

Immunohistochemistry: The samples were fixed in Carnoy's solution at room temperature for 3 h, washed in ethanol for 1 h, dehydrated by using a dehydration device (Leica TP 1020, Wetzlar, Germany) for 12 h, and embedded in paraffin. 5 μm thick paraffin sections were cut using a microtome (Microm HM 430, Thermofisher Scientific, Massachusetts, USA), dried at 37 °C for 12 h, and stored at room temperature. Prior to staining, the samples were deparaffinized by serial dilution of xylol and ethanol. Subsequently, the object slides were placed inside Sequenza Staining racks (Thermofisher Scientific, Massachusetts, USA) to allow the blocking and permeabilization of the samples by using a 0.1% Triton X-100 aqueous solution containing 5% of normal goat serum (NGS) (Agilent Dako, Santa Clara, California, USA) at room temperature for 1 h. The samples were incubated with the primary antibody at 37 °C for 1 h, washed three times with PBS for 5 min, and incubated with the respective secondary antibody for 1 h. Subsequently, the samples were washed three times with PBS for 5 min, incubated with DAPI (1:500) (Thermofisher Scientific, Massachusetts, USA) for 5 min, washed three times with PBS for 5 min, and mounted with fluorescent mounting medium (Agilent Dako, Santa Clara, California, USA). The primary antibodies used in this study are: monoclonal, anti-human alpha-smooth muscle actin (α-SMA) (Sigma-Aldrich, Darmstadt, Germany); monoclonal, anti-human CD31 (Sigma-Aldrich, Darmstadt, Germany); polyclonal, anti-human type I collagen (Acris Antibodies GmbH, Herford, Germany); polyclonal, anti-human type IV collagen (Acris Antibodies GmbH, Herford, Germany); polyclonal, anti-human elastin (Acris Antibodies GmbH, Herford, Germany); monoclonal, anti-human $\alpha_v\beta_3$ integrin (eBioscience, San Diego, California, USA). The secondary antibodies used throughout this study are anti-mouse Alexa Fluor 488 (Thermofisher Scientific, Massachusetts, USA), anti-mouse Alexa Fluor 594 (Thermofisher Scientific, Massachusetts, USA), and anti-rabbit Alexa Fluor 594 (Thermofisher Scientific, Massachusetts, USA).

The Masson's trichrome staining was performed using a Masson's trichrome stain kit (Abcam, Berlin, Germany) as per protocol.

H&E staining were performed using Eosin G solution 0.5% in water (Carl Roth GmbH, Karlsruhe, Germany) to stain the ECM and Hematoxylin solution (Carl Roth GmbH, Karlsruhe, Germany) to counterstain the nuclei. Images were acquired using Vectra 3.0 Microscope Automated Quantitative Pathology Imaging.

For each stained TEVGs' section, representative images were acquired using an Axio Imager M2 fluorescence microscope equipped with an AxioCam MRm Rev.3 camera (Carl-Zeiss, Oberkochen) with a magnification of 20×.

Statistical Analysis: All in vitro samples were analyzed in triplicate (sample size = 3). To obtain R2 and R1 relaxation rate values, MRI images were processed with Imalytics Preclinical Software (Gremse-IT GmbH, Aachen, Germany), which was used first to draw the ROI and then to obtain the R2 and R1 values, respectively. Colormaps were also obtained by using Imalytics Preclinical Software (Gremse-IT GmbH, Aachen, Germany). Regarding the US analysis of bound MBs, images acquired in NLC mode were processed by drawing ROI using the VevoLAB software version 3.2 (FUJIFILM VisualSonics, Toronto, Ontario, Canada). After obtaining Con-

trast mean Power values for the corresponding drawn ROI, d.T.E values were obtained by subtracting the signal before and after MB destruction. The results are presented as mean values $\pm$ standard deviations (SD). The analysis was performed by using GraphPad Prism 9 (GraphPad Prism Software, San Diego, California, USA), and the statistical analyses between two groups (t-test) or multiples groups (one-way ANOVA) (one-tailed) with the suggested post-hoc correction test (Tukey) were applied as recommended by the software. Statistical significance was considered for values p $\leq$ 0.05.

Supporting Information

Supporting Information is available from the Wiley Online Library or from the author.

Conflict of Interest

The authors declare no conflict of interest.

Data Availability Statement

The data that support the findings of this study are available in the supplementary material of this article.

[1] G. A. Roth, G. A. Mensah, V. Fuster, *J. Am. Coll. Cardiol.* **2020**, *76*, 2982.

[2] G. A. Mensah, G. A. Roth, V. Fuster, *J. Am. Coll. Cardiol.* **2019**, *74*, 2529.

[3] V. L. Roger, A. S. Go, D. M. Lloyd-Jones, R. J. Adams, J. D. Berry, T. M. Brown, M. R. Carnethon, S. Dai, G. De Simone, E. S. Ford, C. S. Fox, H. J. Fullerton, C. Gillespie, K. J. Greenlund, S. M. Hailpern, J. A. Heit, P. Michael Ho, V. J. Howard, B. M. Kissela, S. J. Kittner, D. T. Lackland, J. H. Lichtman, L. D. Lisabeth, D. M. Makuc, G. M. Marcus, A. Marelli, D. B. Matchar, M. M. McDermott, J. B. Meigs, C. S. Moy, et al., *Circulation* **2011**, *123*, 18.

[4] F. Wolf, V. Paefgen, O. Winz, M. Mertens, S. Koch, N. Gross-Weege, A. Morgenroth, A. Rix, H. Schnoering, K. Chalabi, S. Jockenhoevel, T. Lammers, F. Mottaghy, F. Kiessling, P. Mela, *Biomaterials* **2019**, *216*, 119228.

[5] C. Spadaccio, A. Rainer, R. Barbato, M. Chello, B. Meyns, *Int. J. Cardiol.* **2013**, *168*, 5028.

[6] Z. Keidar, N. Pirmisashvili, M. Leiderman, S. Nitecki, O. Israel, *J. Nucl. Med.* **2014**, *55*, 392.

[7] P. Zilla, D. Bezuidenhout, P. Human, *Biomaterials* **2007**, *28*, 5009.

[8] A. Subramanian, U. M. Krishnan, S. Sethuraman, *Biomed Res. Int.* **2013**, *2013*, 1.

[9] M. P. Prabhakaran, D. Kai, L. Ghasemi-Mobarakeh, S. Ramakrishna, *Biomed. Mater.* **2011**, *6*, 055001.

[10] H. K. Makadia, S. J. Siegel, *Polymers* **2011**, *3*, 1377.

[11] W. Ji, F. Yang, H. Seyednejad, Z. Chen, W. E. Hennink, J. M. Anderson, J. J. P. van den Beucken, J. A. Jansen, *Biomaterials* **2012**, *33*, 6604.

[12] F. A. Gallagher, *Clin. Radiol.* **2010**, *65*, 557.

[13] T. Van Rooij, V. Daeichin, I. Skachkov, N. De Jong, K. Kooiman, *Int. J. Hyperthermia* **2015**, *31*, 90.

[14] G. Köse, M. Darguzyte, F. Kiessling, *Nanomaterials* **2020**, *10*, 1935.

[15] M. E. Mertens, S. Koch, P. Schuster, J. Wehner, Z. Wu, F. Gremse, V. Schulz, L. Rongen, F. Wolf, J. Frese, V. N. Gesché, M. van Zandvoort, P. Mela, S. Jockenhoevel, F. Kiessling, T. Lammers, *Biomaterials* **2015**, *39*, 155.

[16] M. E. Mertens, A. Hermann, A. Bühren, L. Olde-Damink, D. Möckel, F. Gremse, J. Ehling, F. Kiessling, T. Lammers, *Adv. Funct. Mater.* **2014**, *24*, 754.

[17] E. H. Gang, C. S. Ki, J. W. Kim, J. Lee, B. G. Cha, K. H. Lee, Y. H. Park, *Fibers Polym.* **2012**, *13*, 685.

[18] R. L. Andersson, L. Cabedo, M. S. Hedenqvist, R. T. Olsson, V. Ström, *RSC Adv.* **2016**, *6*, 21413.

[19] L. A. Schneider, A. Korber, S. Grabbe, J. Dissemond, *Arch. Dermatol. Res.* **2007**, *298*, 413.

[20] J. R. Casey, S. Grinstein, J. Orlowski, *Nat. Rev. Mol. Cell Biol.* **2010**, *11*, 50.

[21] G. Chen, T. Sato, H. Ohgushi, T. Ushida, T. Tateishi, J. Tanaka, *Biomaterials* **2005**, *26*, 2559.

[22] M. Krok-Borkowicz, K. Reczyńska, Ł. Rumian, E. Menaszek, M. Orzelski, P. Malisz, P. Silmanowicz, P. Dobrzyński, E. Pamuła, *Int. J. Mol. Sci.* **2020**, *21*, 7541.

[23] J. L. Long, R. T. Tranquillo, *Matrix Biol.* **2003**, *22*, 339.

[24] A. Ratcliffe, *Matrix Biol.* **2000**, *22*, 353.

[25] L. Buttafoco, N. G. Kolkman, P. Engbers-Buijtenhuijs, A. A. Poot, P. J. Dijkstra, I. Vermes, J. Feijen, *Biomaterials* **2006**, *27*, 724.

[26] P. Caravan, B. Das, S. Dumas, F. H. Epstein, P. A. Helm, V. Jacques, S. Koerner, A. Kolodziej, L. Shen, W. C. Sun, Z. Zhang, *Angew. Chem., Int. Ed.* **2007**, *46*, 8171.

[27] M. R. Makowski, A. J. Wiethoff, U. Blume, F. Cuello, A. Warley, C. H. P. Jansen, E. Nagel, R. Razavi, D. C. Onthank, R. R. Cesati, M. S. Marber, T. Schaeffter, A. Smith, S. P. Robinson, R. M. Botnar, *Nat. Med.* **2011**, *17*, 383.

[28] B. Elkenhans, A. Protti, A. Shah, D. Onthank, R. Botnar, *Sci. Rep.* **2021**, *11*, 11004.

[29] S. P. Higgins, A. K. Solan, L. E. Niklason, *J. Biomed. Mater. Res., Part A* **2003**, *67*, 295.

[30] S. Koch, T. C. Flanagan, J. S. Sachweh, F. Tanios, H. Schnoering, T. Deichmann, V. Ellä, M. Kellomäki, N. Gronloh, T. Gries, R. Tolba, T. Schmitz-Rode, S. Jockenhoevel, *Biomaterials* **2010**, *31*, 4731.

[31] N. L'Heureux, S. Pâquet, R. Labbé, L. Germain, F. A. Auger, *FASEB J.* **1998**, *12*, 47.

[32] J. Y. Liu, D. D. Swartz, H. F. Peng, S. F. Gugino, J. A. Russell, S. T. Andreadis, *Cardiovasc. Res.* **2007**, *75*, 618.

[33] A. Fernández-Colino, F. Wolf, S. Rütten, T. Schmitz-Rode, J. C. Rodríguez-Cabello, S. Jockenhoevel, P. Mela, *Front. Bioeng. Biotechnol.* **2019**, *7*, 340.

[34] I. G. De Torre, F. Wolf, M. Santos, L. Rongen, M. Alonso, S. Jockenhoevel, J. C. Rodríguez-Cabello, P. Mela, *Acta Biomater.* **2015**, *12*, 146.

[35] E. D. Boland, J. A. Matthwes, K. J. Pawlowski, D. G. Simpson, G. E. Wnek, G. L. Bowlin, *Front. Biosci.* **2004**, *26*, 1422.

[36] R. Wang, B. J. De Kort, A. I. P. M. Smits, A. S. Weiss, *Elastin in Vascular Grafts*, Springer, Cham **2020**.

[37] M. S. Hahn, M. K. McHale, E. Wang, R. H. Schmedlen, J. L. West, *Ann. Biomed. Eng.* **2007**, *35*, 190.

[38] S. I. Jeong, J. H. Kwon, J. I. Lim, S. W. Cho, Y. Jung, W. J. Sung, S. H. Kim, Y. H. Kim, Y. M. Lee, B. S. Kim, C. Y. Choi, S. J. Kim, *Biomaterials* **2005**, *26*, 1405.

[39] E. T. Choi, L. Engel, A. D. Callow, S. Sun, J. Trachtenberg, S. Santoro, U. S. Ryan, *J. Vasc. Surg.* **1994**, *19*, 125.

[40] T.-L. Yue, J. M. Stadel, *Exp. Cell Res.* **1994**, *214*, 459.

[41] L. Liaw, M. P. Skinner, E. W. Raines, R. Ross, D. A. Cheresh, S. M. Schwartz, C. M. Giachelli, *J. Clin. Invest.* **1995**, *95*, 713.

[42] A. Rix, S. Fokong, S. Heringer, R. Pjontek, L. Kabelitz, B. Theek, M. A. Brockmann, M. Wiesmann, F. Kiessling, *Invest. Radiol.* **2016**, *51*, 767.

[43] B. Gao, T. M. Saba, M. Tsan, *Am. J. Physiol. - Cell Physiol.* **2002**, *283*, C1196.

[44] T. V. Byzova, R. Rabbani, S. E. D'Souza, E. F. Plow, *Thromb. Haemostasis* **1998**, *80*, 726.

[45] I. Delon, N. H. Brown, *Curr. Opin. Cell Biol.* **2007**, *19*, 43.

[46] W. F. Daamen, D. Quaglino, *Cell. Signalling* **2019**, *63*, 109364.

[47] B. Venkatesh, G. Tanentzapf, R. J. Khadilkar, K. Y. L. Ho, B. Venkatesh, G. Tanentzapf, *Curr. Biol.* **2020**, *30*, 3316.

[48] M. C. Sutcliffe, J. M. Davidson, *Matrix Collagen Relat. Res.* **1990**, *10*, 148.

[49] R. Jin, B. Lin, D. Li, H. Ai, *Curr. Opin. Pharmacol.* **2014**, *18*, 18.

[50] S. S. Moonshi, C. Zhang, H. Peng, S. Puttick, S. Rose, N. M. Fisk, K. Bhakoo, B. W. Stringer, G. G. Qiao, P. A. Gurr, A. K. Whittaker, *Nanoscale* **2018**, *10*, 8226.

[51] T. Lammers, M. E. Mertens, P. Schuster, K. Rahimi, Y. Shi, V. Schulz, A. J. C. Kuehne, S. Jockenhoevel, F. Kiessling, *Chem. Mater.* **2017**, *29*, 2669.

[52] O. Bruder, S. Schneider, D. Nothnagel, G. Pilz, M. Lombardi, A. Sinha, A. Wagner, T. Dill, H. Frank, A. Van Rossum, J. Schwitter, E. Nagel, J. Senges, G. Sabin, U. Sechtem, H. Mahrholdt, *JACC Cardiovasc. Imaging* **2011**, *4*, 1171.

[53] J. V. Terrovitis, J. W. M. Bulte, S. Sarvananthan, L. A. Crowe, P. Sarathchandra, P. Batten, E. Sachlos, A. H. Chester, J. T. Czernuszka, D. N. Firmin, P. M. Taylor, M. H. Yacoub, *Tissue Eng.* **2006**, *12*, 2765.

[54] F. Hyafil, E. Vucic, J. C. Cornily, R. Sharma, V. Amirbekian, F. Blackwell, E. Lancelot, C. Corot, V. Fuster, Z. S. Galis, L. J. Feldman, Z. A. Fayad, *Eur. Heart J.* **2011**, *32*, 1561.

[55] Q. Sun, M. Baues, B. M. Klinkhammer, J. Ehling, S. Djudjaj, N. I. Drude, C. Daniel, K. Amann, R. Kramann, H. Kim, J. Saez-Rodriguez, R. Weiskirchen, D. C. Onthank, R. M. Botnar, F. Kiessling, J. Floege, T. Lammers, P. Boor, *Sci. Transl. Med.* **2019**, *11*, 1.

[56] P. Caravan, Y. Yang, R. Zachariah, A. Schmitt, M. Mino-Kenudson, H. H. Chen, D. E. Sosnovik, G. Dai, B. C. Fuchs, M. Lanuti, *Am. J. Respir. Cell Mol. Biol.* **2013**, *49*, 1120.

[57] I. Papantoniou, M. Sonnaert, L. Geris, F. P. Luyten, J. Schrooten, G. Kerckhofs, *Tissue Eng., Part C Methods* **2014**, *20*, 177.

[58] H. Talacua, Proefschrift, Universiteit Utrecht, Nederland, *In Situ Cardiovascular Tissue Engineering*, **2016**.

[59] Y. Wang, E. Bella, C. S. D. Lee, C. Migliaresi, L. Pelcastre, Z. Schwartz, B. D. Boyan, A. Motta, *Biomaterials* **2010**, *31*, 4672.

[60] H. Xu, S. F. Othman, R. L. Magin, *J. Biosci. Bioeng.* **2008**, *106*, 515.

[61] A. Curaj, Z. Wu, S. Fokong, E. A. Liehn, C. Weber, A. Burlacu, T. Lammers, M. Van Zandvoort, F. Kiessling, *Arterioscler., Thromb., Vasc. Biol.* **2015**, *35*, 1366.

[62] L. Appold, Y. Shi, S. Rütten, A. Kühne, A. Pich, F. Kiessling, T. Lammers, *Macromol. Biosci.* **2017**, *17*, 1.

[63] L. Oddo, G. Paradossi, B. Cerroni, C. Ben-Harush, E. Ariel, F. Di Meco, Z. Ram, R. Grossman, *ACS Omega* **2019**, *4*, 13371.

[64] J. Kappelmayer, B. Nagy, K. Miszti-Blasius, Z. Hevessy, H. Setiadi, *Clin. Chem. Lab. Med.* **2004**, *42*, 475.

[65] U. Gotsch, U. Jäger, M. Dominis, D. Vestweber, *Cell Commun. Adhes.* **1994**, *2*, 7.

2105783 (14 of 15)

[66] K. Ley, Y. Huo, *J. Clin. Invest.* **2001**, *107*, 1209.

[67] T. Masumura, K. Yamamoto, N. Shimizu, S. Obi, J. Ando, *Arterioscler., Thromb., Vasc. Biol.* **2009**, *29*, 2125.

[68] J. E. Nesmith, J. C. Chappell, J. G. Cluceru, V. L. Bautch, *Development* **2017**, *144*, 869.

[69] P. J. Lenting, O. D. Christophe, C. V. Denis, *Blood* **2015**, *125*, 2019.

[70] Q. Li, T. Syrovets, T. Simmet, J. Ding, J. Xu, W. Chen, D. Zhu, P. Gao, *Exp. Biol. Med.* **2013**, *238*, 176.

[71] A. Curaj, Z. Wu, A. Rix, O. Gresch, M. Sternkopf, S. Alampour-Rajabi, T. Lammers, M. Van Zandvoort, C. Weber, R. R. Koenen, E. A. Liehn, F. Kiessling, *Arterioscler., Thromb., Vasc. Biol.* **2018**, *38*, 40.

[72] S. Mohammadali, K. Roemhild, N. I. Drude, S. Von Stillfried, R. Knüchel, F. Kiessling, T. Lammers, *J., Nanobiotechnol.* **2019**, *138*, 302.

[73] R. Hufschmid, H. Arami, R. M. Ferguson, M. Gonzales, E. Teeman, L. N. Brush, D. Browning, K. M. Krishnan, *Nanoscale* **2015**, *7*, 11142.

[74] M. Palmowski, B. Morgenstern, P. Hauff, M. Reinhardt, J. Huppert, M. Maurer, E. C. Woenne, S. Doerk, G. Ladewig, J. W. Jenne, S. Delorme, L. Grenacher, P. Hallscheidt, G. W. Kauffmann, W. Semmler, F. Kiessling, *Invest. Radiol.* **2008**, *43*, 162.

[75] M. Palmowski, P. Peschke, J. Huppert, P. Hauff, M. Reinhardt, M. Maurer, C. P. Karger, M. Scholz, W. Semmler, P. E. Huber, F. M. Kiessling, *Neoplasia* **2009**, *11*, 856.

[76] V. Pathak, T. Nolte, E. Rama, A. Rix, S. M. Dadfar, V. Paefgen, S. Banala, E. M. Buhl, M. Weiler, V. Schulz, T. Lammers, F. Kiessling, *Biomaterials* **2021**, *275*, 120896.

2105783 (15 of 15)

Supporting Information

Monitoring the Remodeling of Biohybrid Tissue-Engineered Vascular Grafts by Multimodal Molecular Imaging

Elena Rama, Saurav Ranjan Mohapatra, Christoph Melcher, Teresa Nolte, Seyed Mohammadali Dadfar, Ramona Brueck, Vertika Pathak, Anne Rix, Thomas Gries, Volkmar Schulz, Twan Lammers, Christian Apel, Stefan Jockenhoevel and Fabian Kiessling[*]

Supporting Information

Monitoring the Remodeling of Biohybrid Tissue-Engineered Vascular Grafts by Multimodal Molecular Imaging

Elena Rama, Saurav Ranjan Mohapatra, Christoph Melcher, Teresa Nolte, Seyed Mohammadali Dadfar, Ramona Brueck, Vertika Pathak, Anne Rix, Thomas Gries, Volkmar Schulz, Twan Lammers, Christian Apel, Stefan Jockenhoevel and Fabian Kiessling[*]
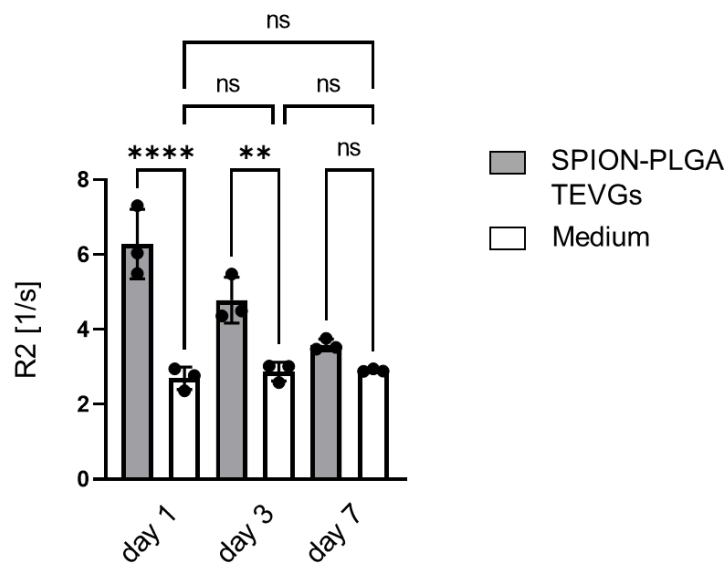
Figure S1. MRI evaluation of SPION release into the bioreactor medium. A slight increase in the R2 relaxation rates of the mediums was observed from day 1 to day 7 days of bioreactor conditioning of TEVGs, indicating the release of the SPION from the degrading PLGA fibers into the medium. Inversely, the R2 values of 0.2% SPION-labeled PLGA fibers decrease over time, indicating PLGA degradation. All values are obtained in triplicates: mean $\pm$ SD; *p<0.05, **p<0.01, ***p<0.001, and ****p<0.0001.
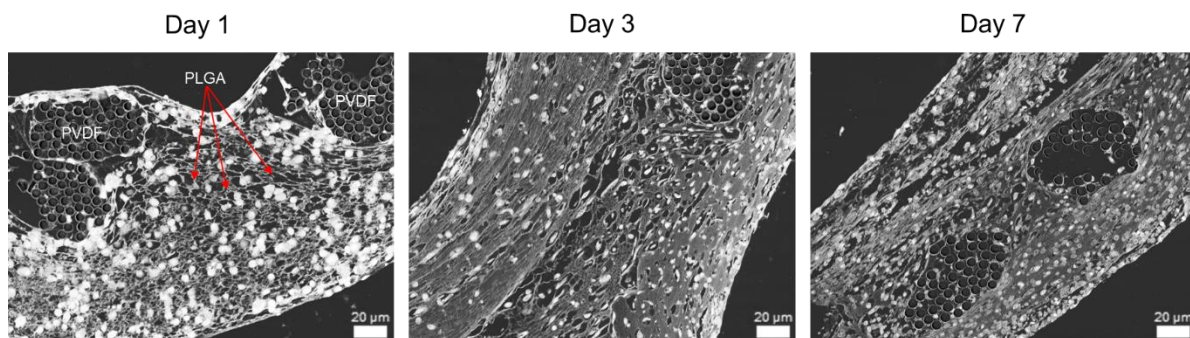
Figure S2. H&E staining of TEVGs. H&E staining were performed using Eosin G solution 0.5 % in water to stain the ECM and Hematoxylin solution for the counterstain of the nuclei. Images were acquired using Vectra® 3.0 Microscope Automated Quantitative Pathology Imaging System and converted in gray scale to enhance the visualization of the PLGA fiber. Histology images show the gradual replacing of PLGA with newly deposited ECM. Images were acquired after 1 day, 3 days, and 7 days of bioreactor conditioning of TEVGs.
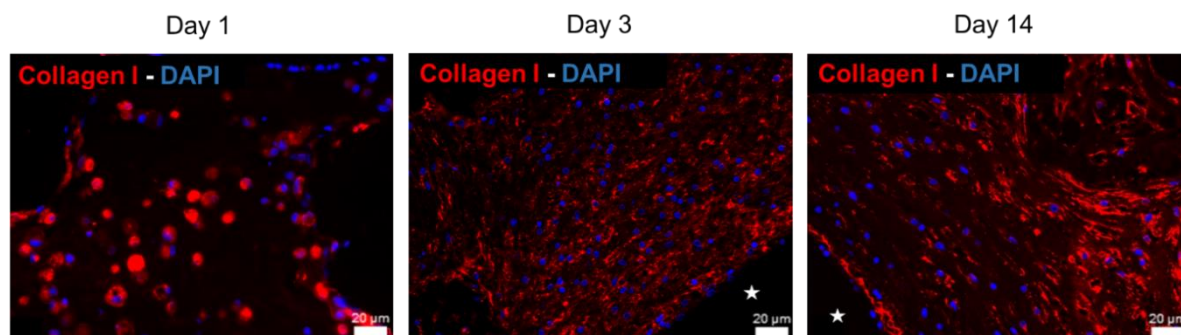
Figure S3. Histological analysis of collagen type I deposition within TEVGs. Immunofluorescence images show collagen type I positive cells already at day 1 of TEVGs maturation. At day 3 of bioreactor conditioning, there is a strong collagen type I deposition, which further increases until the last day of TEVGs monitoring. The star indicates TEVGs' lumen.
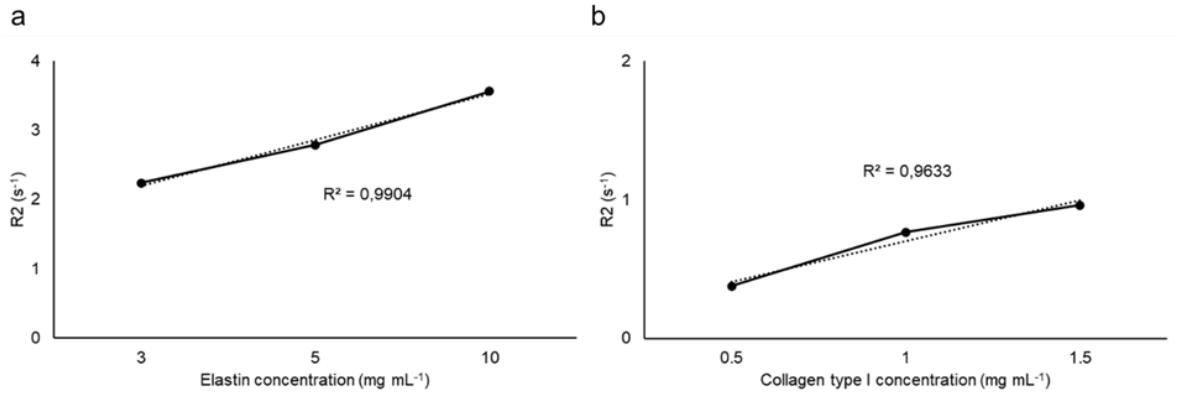
Figure S4. Linearity between MRI signal and amount of elastin and collagen type I. Graphs show the linear correlation between the ESMA or EP-3533 MRI signal at different concentration of elastin or collagen type I introduced in the fibrin gel used for the molding of the vascular grafts.
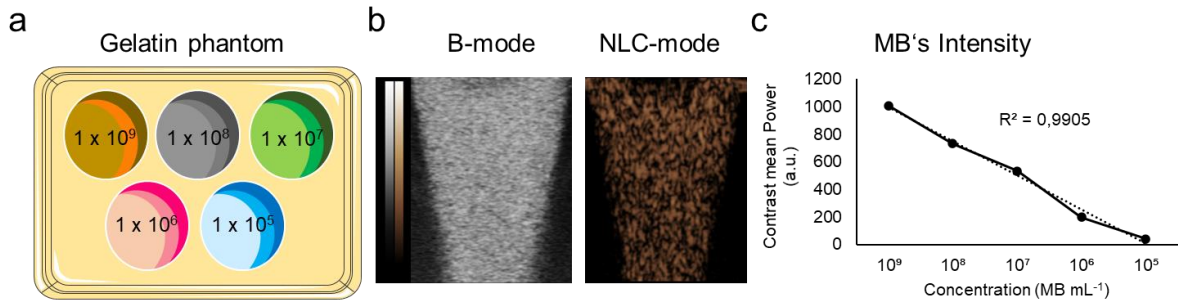

Figure S5. Linear correlation between MB's concentration and US contrast intensity. a: Schematic depiction of the 10% w/v gelatin phantom in which the wells were obtained by dipping sand-filled Eppendorf tubes until solidification of the gelatin. Later, the wells were filled with a mixture of 3% w/v gelatin and different concentration (ranging from 1×10^9 MB mL^{-1} to 1×10^5 MB mL^{-1}) of c[RGDfK]-MBs. b: US images in B-mode and NLC-mode of the gelatin embedded MBs. c: The linear correlation between MB's concentration and US signal intensity detected ($R^2 = 0.9905$) indicates the high sensitivity of the US.
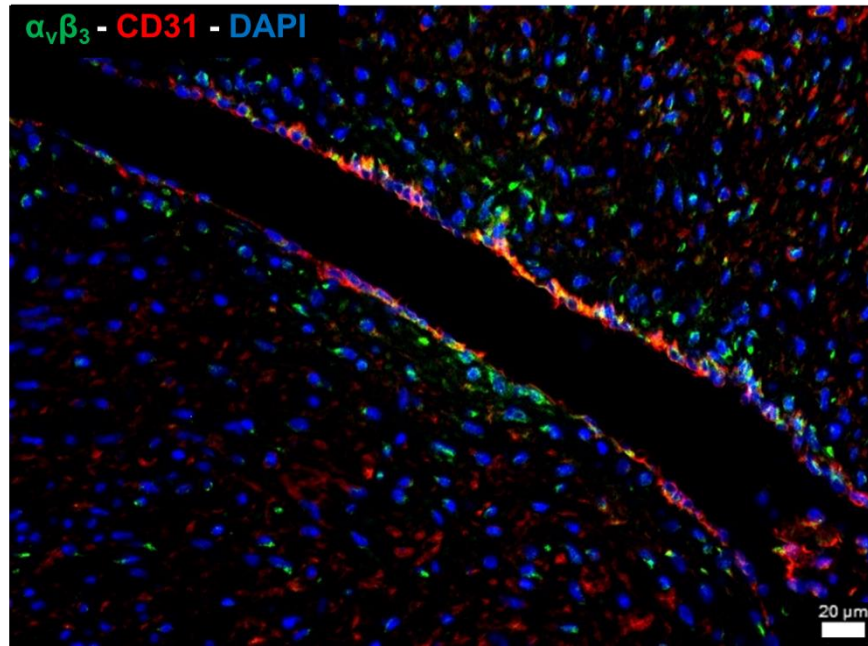
Figure S6. $\alpha_v\beta_3$ integrin staining (green) in HUA. ECs are visualized with a CD31 staining (red) and cell nuclei with DAPI (blue). This representative image shows the colocalization of $\alpha_v\beta_3$ integrins with the endothelial lining, indicating the physiological expression of integrins within the HUA.

In vitro and in vivo evaluation of biohybrid tissue-engineered vascular grafts with transformative ^{1}H/^{19}F MRI traceable scaffolds

Elena Rama [a], Saurav Ranjan Mohapatra [b], Yukiharu Sugimura [c], Tomoyuki Suzuki [c], Stefan Siebert [b], Roman Barmin [a], Juliane Hermann [d], Jasmin Baier [a], Anne Rix [a], Teresa Lemainque [a,e], Susanne Koletnik [a], Asmaa Said Elshafei [a], Roger Molto Pallares [a], Seyed Mohammadali Dadfar [a,f], René H. Tolba [g], Volkmar Schulz [a], Joachim Jankowski [d,h,i], Christian Apel [b], Payam Akhyari [c], Stefan Jockenhoevel [b], Fabian Kiessling [a,*]

[a] *Institute for Experimental Molecular Imaging, Faculty of Medicine, RWTH Aachen University, Forckenbeckstraße 55, 52074 Aachen, Germany*
[b] *Department of Biohybrid & Medical Textiles, AME-Institute of Applied Medical Engineering, Helmholtz Institute, RWTH Aachen University, Forckenbeckstraße 55, 52074 Aachen, Germany*
[c] *Department of Cardiac Surgery, Medical Faculty and RWTH University Hospital Aachen, RWTH Aachen University, Aachen, Germany*
[d] *Institute for Molecular Cardiovascular Research (IMCAR), University Hospital RWTH Aachen, Aachen, Germany*
[e] *Department of Diagnostic and Interventional Radiology, Medical Faculty, RWTH Aachen University, 52074 Aachen, Germany*
[f] *Ardena Oss, 5349 AB Oss, the Netherlands*
[g] *Institute for Laboratory Animal Science and Experimental Surgery, Medical Faculty, RWTH Aachen International University, Aachen, Germany*
[h] *Aachen-Maastricht Institute for CardioRenal Disease (AMICARE), University Hospital RWTH Aachen, Aachen, Germany*
[i] *Department of Pathology, Cardiovascular Research Institute Maastricht (CARIM), University of Maastricht, the Netherlands*

ARTICLE INFO

ABSTRACT

Biohybrid tissue-engineered vascular grafts (TEVGs) promise long-term durability due to their ability to adapt to hosts' needs. However, the latter calls for sensitive non-invasive imaging approaches to longitudinally monitor their functionality, integrity, and positioning. Here, we present an imaging approach comprising the labeling of non-degradable and degradable TEVGs' components for their in vitro and in vivo monitoring by hybrid ^{1}H/^{19}F MRI. TEVGs (inner diameter 1.5 mm) consisted of biodegradable poly(lactic-*co*-glycolic acid) (PLGA) fibers passively incorporating superparamagnetic iron oxide nanoparticles (SPIONs), non-degradable polyvinylidene fluoride scaffolds labeled with highly fluorinated thermoplastic polyurethane (^{19}F-TPU) fibers, a smooth muscle cells containing fibrin blend, and endothelial cells. ^{1}H/^{19}F MRI of TEVGs in bioreactors, and after subcutaneous and infrarenal implantation in rats, revealed that PLGA degradation could be faithfully monitored by the decreasing SPIONs signal. The ^{19}F signal of ^{19}F-TPU remained constant over weeks. PLGA degradation was compensated by cells' collagen and α-smooth-muscle-actin deposition. Interestingly, only TEVGs implanted on the abdominal aorta contained elastin. XTT and histology proved that our imaging markers did not influence extracellular matrix deposition and host immune reaction. This concept of non-invasive longitudinal assessment of cardiovascular implants using ^{1}H/^{19}F MRI might be applicable to various biohybrid tissue-engineered implants, facilitating their clinical translation.

1. Introduction

Cardiovascular diseases (CVD), such as deep vein thrombosis, aortic, coronary artery, cerebrovascular, and peripheral artery disease, combined with longstanding diabetes and hypertension, as well as an ever-increasing aging population, are the leading cause of death worldwide [1,2]. Common surgical strategies for treating CVD include coronary artery bypass or major arterial reconstruction. Bypassing obstructed or aneurysmal vascular segments through an autologous graft, such as saphenous vein, radial, and mammary artery, is currently the preferred clinical treatment [3]. It does not trigger an immune foreign body reaction, preventing graft rejection, and already possesses a functional

endothelial layer that prevents thrombosis or excessive smooth muscle cell (SMC) proliferation. However, autologous grafts present a substantial drawback, namely donor morbidity that prevents autografting [4].

Synthetic grafts, e.g., from expanded polytetrafluoroethylene (GORE-TEX), poly(ethylene terephthalate) (Dacron), and polyurethane (PU), are viable alternatives [5]. Currently, synthetic grafts dominate the global vascular grafts market with an estimated compound annual growth rate (CAGR) of 7.0 % from 2022 to 2030 (source: Grand View Research, Report ID: 978-1-68038-628-8). Despite their extensive use in standard clinical practice, synthetic grafts have many limitations as they tend to exacerbate chronic immune reactions, inflammation, calcification, thrombosis, and stenosis parallel to their inability to grow with the host organism, lack of remodeling, compliance mismatch, and limited application to >6 mm diameter blood vessels [6,7].

As a future alternative, biohybrid tissue-engineered vascular grafts (TEVGs) are being developed [8,9]. Their scaffolds often combine non-degradable and biodegradable materials to optimally balance scaffold durability and adaptability. Indeed, the presence of a permanent scaffold, albeit minimal, is needed to withstand blood pressure during in vivo implantation and ensure graft integrity, while the presence of biodegradable materials is needed to facilitate scaffold growth, remodeling, and integration within the host organism. Notably, the degradation of these biodegradable materials induces mechanical stress, which in turn triggers extracellular matrix (ECM) production, thereby preserving the structural integrity of the graft and facilitating the restoration of native-like tissue. Additionally, this process allows for scaffold reshaping, preventing the formation of a too-rigid structure that could hinder the physiological integration and maturation of TEVGs. However, the production of native-like ECM is not always guaranteed since it depends on several interconnected mechano- and immune-driven processes. Key factors such as scaffold topography (pore and fiber size), scaffold chemical composition, and material degradation rate influence and are influenced by the ECM-cell interaction, matrix-bound vesicles-mediated ECM immunomodulatory effects, as well as integrin-mediated cell response, infiltration rate of T-cells and M2 macrophages [8,9]. The latter are fundamental for a functional endothelium, SMCs proliferation, and consequent release of pro-inflammatory cytokines and anti-inflammatory cytokines, i.e., IL-10 responsible for ECM remodeling via matrix metalloproteinase-9.

Due to the high flexibility of TEVGs to adapt to their environment, dysregulation and dysfunction may already occur during in vitro maturation as well as during the in vivo remodeling. Thus, regular monitoring of TEVGs' in vitro and in vivo maturation is mandatory to e. g., avoid the implantation of dysfunctional systems, and early detect and treat rejection, acute/chronic inflammation, as well as loss of graft patency due to thrombosis and stenosis [10–13].

In this context, magnetic resonance imaging (MRI) is one of the most powerful diagnostic tools. Despite the higher costs and longer processing times associated with MRI compared to other routinely employed imaging techniques (i.e., X-ray fluoroscopy and computed tomography), MRI offers a better soft tissue contrast and provides complementary functional information. Even though it is worth noting that CT technology is currently strongly evolving towards higher sensitivity and specificity due to the introduction of single photon counting and spectral detectors, MRI further advantages are the lack of ionizing radiation, and the higher sensitivity imaging markers (micromolar range in comparison to millimolar range in CT) [14,15]. Many ^{1}H contrast agents are (pre)clinically employed, e.g., gadolinium (Gd)- or iron-based (i.e., superparamagnetic iron oxide nanoparticles, SPIONs), to acquire distinct tissue characteristics [16,17]. However, to enhance the specificity for material detection, several studies headed their research toward the application of ^{19}F MRI as a parallel alternative to ^{1}H MRI [18]. The almost complete lack of endogenous ^{19}F in the human body leads to an almost linear relationship between ^{19}F content and measured signal [19,20]. Nevertheless, due to the limited signal sensitivity of current MR

hardware (in the range of mM concentrations) and the low abundance of ^{19}F nuclei in vivo following exogenous administration, high concentrations of mobile ^{19}F equivalent atoms are required. Commonly used fluoropolymers, such as polyvinylidene fluoride (PVDF), polytetrafluoroethylene (PTFE), perfluoroalkoxy (PFA), fluorinated ethylene propylene (FEP), ethylene tetrafluoroethylene (ETFE), and ethylene chlorotrifluoroethylene (ECTFE), exhibit excellent characteristics for tissue engineering purposes. However, they are entirely unsuitable for ^{19}F MRI applications given their high crystallinity, which results in a rapid decay of the MRI signal for mechanically rigid ^{19}F atoms. Previous studies addressed this limitation by utilizing a novel highly fluorinated polymer, fluorinated thermoplastic polyurethane (^{19}F-TPU), which possesses an amorphous structure and a large number of magnetically equivalent ^{19}F atoms capable to vibrate freely [21,22]. ^{19}F-TPU differs from other MRI markers i.e., Gadolinium, which are detected through a change in relaxivity based on the chemical environment. Moreover, ^{19}F-TPU offers several advantages, including biocompatibility, chemical inertness, and non-immunogenicity.

To ensure non-invasive monitoring of TEVGs' remodeling without losing track of their positioning and structural integrity, we here propose the combined use of permanent fibers (^{19}F-TPU and PVDF) and a biodegradable component, poly(lactic-*co*-glycolic acid) (PLGA). This FDA-approved biodegradable polymer is known for its versatility, strong physical properties, high biocompatibility, tuneable physical properties, non-toxic degradation by-products, extensive research support, and clinical experience [23]. As shown in Fig. 1, we first incorporated oleic acid coated SPIONs into the core of the PLGA fibers and added ^{19}F-TPU to the main PVDF tubular scaffold to compensate for their lack of MR visibility and monitorability. TEVGs were finally obtained by molding the textile scaffold with fibrin gel containing SMCs and endothelial cells (ECs). The incorporation of the selected MRI labels (SPIONs and ^{19}F) ensured the non-invasive longitudinal monitoring of TEVGs via hybrid ^{1}H/^{19}F MRI. This allowed efficient assessment of SPIONs-labeled PLGA fibers (SPION-PLGA) degradation over time and permanent monitoring of the positioning and integrity of the TEVGs both in vitro during bioreactor conditioning and in vivo as subcutaneous implants as well as abdominal aorta bypass in rats. Moreover, the excellent biocompatibility of all textile components used in our model of TEVGs was thoroughly investigated via cytotoxicity assays and histological analyses.

2. Materials and methods

2.1. Textile scaffold production

2.1.1. PVDF mesh
PVDF (Lenzing Plastics GmbH & co. KG, Lenzing, Austria) multifilament fibers (150 dtex, 48 filaments) were employed to produce a tubular textile scaffold using a double-bar raschel warp-knitting machine (RIUS, COMATEX, Barcelona, Spain).

2.1.2. Oleic acid-coated SPIONs
Oleic acid-coated SPIONs were synthesized by thermal decomposition based on a previously established protocol [24,25]. Briefly, 7.2 g of the iron (III) oleate and 18.4 g of oleic acid were dissolved in 50 mL of 1-octadecene. Then, the mixture was heated to 100 °C and maintained at this temperature without reflux for 30 min. After degassing, fitting a reflux cooler, and purging the flask with argon, the reaction mixture was heated further to 340 °C with a heating rate of 3 °C min^{-1} under argon atmosphere for 3 h. After cooling down to room temperature, the freshly prepared nanoparticles were precipitated by adding acetone to the flask. The mixture was sonicated, centrifuged and the supernatant was discarded. Finally, the washed nanoparticles were dispersed in hexane and methanol (1:6) and further centrifuged. Following several washing steps, one drop of oleic acid was added to the nanoparticles dispersed in hexane.
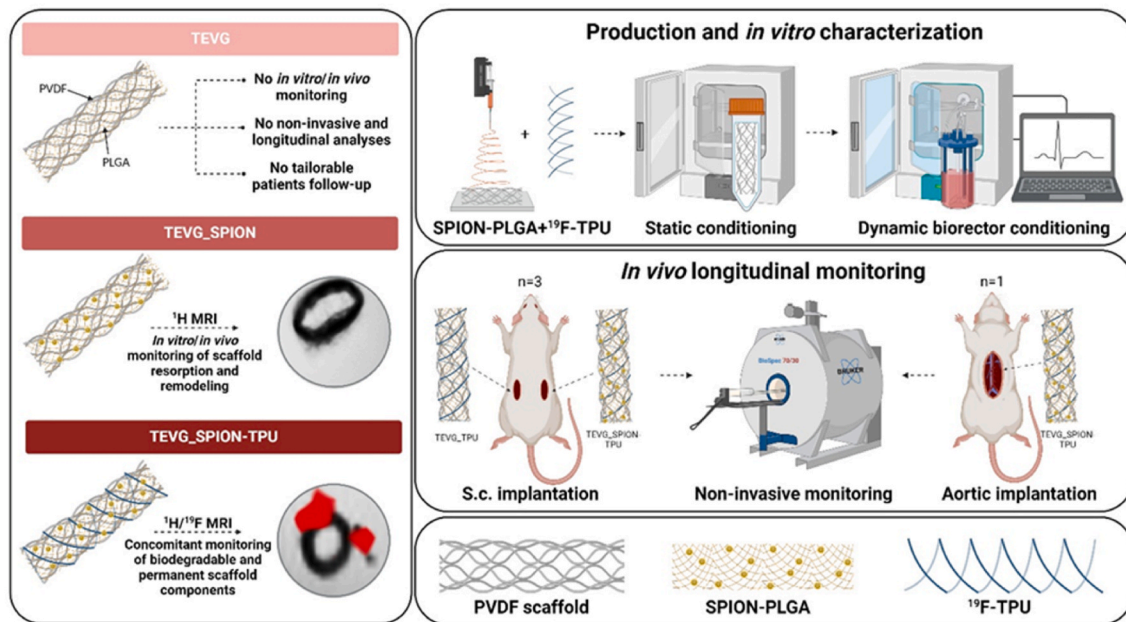
Fig. 1. Schematic depiction of the study design (Created with BioRender.com).

2.1.3. Electrospun SPION-PLGA fibers

As described in a previously published protocol, a coaxial spinning head (Bioinicia SL, Paterna, Spain) with two coaxial arranged steel capillaries with inner diameters of 1400 μm (shell capillary) and 580 μm (core capillary) were used [12]. To obtain a core-shell fiber structure, a solution containing 6 % (w/w) PLGA labeled with 0.2 % (w/w) SPIONs was used for the core and one with 6 % (w/w) PLGA was employed for the shell. The SPION-PLGA fibers were spun at a voltage of $+22$ kV (emitter) and -20 kV (collector) at 25 °C and 30 % humidity. Both spinning solutions were prepared by dissolving the PLGA in methanol and chloroform (MeOH, neoLab Migge Laborbedarf – Vertriebs GmbH, Heidelberg, Germany and CHCl3, Carl Roth GmbH & Co. KG, Karlsruhe, Germany). SPIONs were added to the core solution shortly before starting the electrospinning procedure. After placing the PVDF warp-knitted scaffold on a cylindrical collector, the spinning head, placed at a distance of 15 cm, was moved over the entire length of the meshes at a speed of 30 mm s^{-1} with core and shell solutions' flow rates set to 0.5 mL h^{-1} and 1 mL h^{-1}.

2.1.4. ^{19}F-TPU fibers

^{19}F-TPU was purchased as granules from Lubrizol, Wickliffe, Ohio, United States, and dried at 80 °C for 24 h prior to spinning. To obtain multifilaments (68 dtex, 48 filaments) via melt spinning (Fourné Polymertechnik GmbH, Alfter, Germany), a blow chamber, multifilament spinnerets, heating godet and a winder were used with process temperatures ranging from 185 to 220 °C.

2.2. TEVGs preparation

2.2.1. Harvesting of syngeneic cells

All animal experiments were approved by the German State Office for Nature, Environment and Consumer Protection (LANUV) North Rhine-Westphalia and performed in adherence to institutional guidelines, EU Directive 2010/63, and the German federal law on the protection of animals. All animals received humane care conforming to the principles of the "Guide for the Care and Use of Laboratory Animals" (8th Edition, National Institutes of Health (NIH) Publication, 2011, USA). The study was designed, executed, and reported in line with the "Animal Research: Reporting of In Vivo Experiments" (ARRIVE) guidelines. Inbred Lewis male rats (Strain name: LEW/OrlRj, Janvier Labs, Le Genest Saint Isle, France) were chosen as the appropriate animal model.

Inbred siblings share nearly identical genetic pools, allowing TEVGs containing cells harvested from one sibling to be implanted in another without causing inflammation or graft rejection. Furthermore, euthanizing one donor animal enables the collection of a maximum of cells and tissues, preventing the over-stressing of a single animal with both surgeries - cell and tissue harvesting followed by TEVG implantation. With a ratio of 1:3, cells harvested from one donor animal were used to produce 3 syngeneic TEVGs. ECs were derived from enzymatic digestion of the abdominal aorta, while adipose mesenchymal stem cells were derived from adipose tissue, an easily accessible source that provides a high yield of these cells. These cells display a smooth muscle-like phenotype after in vitro mechanostimulation in the bioreactor [26,27].

2.2.2. Harvesting of human cells

The use of human samples was conducted in compliance with the Ethical Committee approval (EK 2067). Human umbilical cords were used to harvest human umbilical artery smooth muscle cells (HUASMCs) and human umbilical artery endothelial cells (HUAECs).

2.2.3. Bioreactor conditioning of TEVGs

TEVGs for in vitro testing were produced using human cells, while TEVGs intended for implantation into rats were produced using syngeneic cells from Lewis male rats. In detail, a silicon tube of 2.4 mm inner diameter (Carl Roth GmbH, Germany) and a metal rod of 1.5 mm diameter were used for the molding of the textile scaffold. As described in a previously published protocol, TEVGs containing human cells were produced using 10 mg mL^{-1} fibrinogen (Calbiochem, Darmstadt, Germany), 40 U mL^{-1} thrombin (Sigma, Steinheim, Germany), TRIS buffer, and 50 mM CaCl₂ (Sigma, Steinheim, Germany), and 10×10^6 HUASMCs mL^{-1} and a total of 1.4 mL per cm graft were injected into the silicon tube containing the textile scaffold and the metal rod [12]. 3×10^6 HUAECs mL^{-1} and a total of 1 mL per cm graft were employed for the endothelialization of the TEVGs lumen, which was performed under constant rotation for 24 h. TEVGs underwent bioreactor conditioning for a maximum of 4–7 days.

For all TEVGs, the employed bioreactor system consisted of i) a 500 mL medium reservoir, ii) a peristaltic pump (MCP Process, Ismatec, Cole Parmer GmbH, Germany) to modulate the medium dynamic flow, and iii) flow and pressure sensors (Em-tec GmbH, Finning, Germany and Codan GmbH, Lensahn, Germany) to monitor flow and pressure within the system.

The mechanical properties of our TEVGs were assessed, focusing on burst, biaxial, and suture retention strength, as described in a previously published protocol [22]. All tested parameters demonstrated that our TEVGs are characterized by sufficient mechanical strength. The presence of ^{19}F-TPU fibers sutured on the preexisting PVDF and PLGA textile scaffold are expected to not affect the prostheses' mechanical properties.

2.3. MRI longitudinal evaluation of SPION-PLGA fiber degradation

A Bruker BioSpec 70/20 USR 7 T MRI scanner (Bruker BioSpin GmbH, Germany) equipped with a ^{1}H transmit-receive volume coil with active detuning with an inner diameter of 82 mm and a bore length of 112 mm was used to evaluate temperature (37 and 70 °C), static or dynamic culturing, and degradation process (hydrolysis or enzymatic) as main variables affecting PLGA degradation. A first set of samples (SPION-PLGA fibers) was incubated at different temperatures (37 and 70 °C) and subjected to either static or dynamic culturing conditions for 4 weeks. A second set of samples was incubated at fixed 37 °C, but exposed to i) a slightly acidic environment, ii) enzymes, iii) a combination of both. All samples were imaged every one week. All MRI images presented in this study were acquired axially. Qualitative ^{1}H-T$_2$-weighted images were acquired using a fast spin echo sequence [Repetition time (TR): 2197 ms; Echo time (TE): 80 ms; echo spacing: 26 ms; acceleration factor: 8; matrix size; 180 x 180; Field of view (FOV): (25 x 25) mm^2; slice thickness; 5 mm; total acquisition time: 6 min]. The degradation of the SPION-PLGA coating was quantified by the decrease in transverse relaxation times (T$_2$), measured using a 2D multi-slice, multi-echo spin-echo (MSME) sequence with a 90° excitation pulse followed by a train of equally spaced 180° refocusing pulses [TR: 3742 ms; TE: 20 ms; echo spacing: 20 ms; echo images: 30; number of averages: 4; matrix size: 100 x 100; FOV: (25 x 25) mm^2; slice thickness: 5 mm; total acquisition time: 25 min]. T$_2$ relaxation times and the corresponding R2 relaxation rates (T$_2^{-1}$) were calculated using Imalytics Preclinical Software (Gremse-IT GmbH, Aachen, Germany) by fitting an exponential curve to the signal amplitudes as a function of the TE for each segmented region of interest (ROI). Equation (1) was used for the fitting of the exponential curve:

$$M = M_0\, e^{-\frac{TE}{T2}} + C \tag{1}$$

The offset (C) was included to account for a signal plateau created by noise or a component with slow signal decay. The relaxation rate R$_2$ was calculated as the inverse of T$_2$.

Additionally, R$_2$ colormaps were obtained after voxel-wise fitting of equation (1) using the ParaVision 7 preclinical imaging software (Bruker BioSpin GmbH, Germany).

2.4. In vitro characterization of the textile scaffold and TEVGs by hybrid ^{1}H/^{19}F MRI

2.4.1. ^{19}F-TPU characterization

The Bruker 7 T MRI scanner equipped with a ^{1}H/^{19}F transmit-receive volume coil (72 mm of inner diameter and 112 mm of bore length) with active detuning was used. First, the ^{19}F-TPU granules (Lubrizol, Wickliffe, Ohio, United States) were tested alongside a water phantom. Subsequently, non-localized spectra of ^{19}F were acquired with an NSPECT sequence [TR: 1000 ms; flip angle: 30°; number of acquisition points: 10000; bandwidth: 353.87 ppm; averages: 30; total acquisition time: 30 s]. The spectra showed one defined peak at −84 ppm and one smaller side peak at −78 ppm, indicating that not all fluorine atoms in the ^{19}F-TPU polymeric chain are equivalent. For all following ^{19}F-TPU image acquisitions, the offset frequency was set to −24.000 Hz from the ^{1}H peak. Prior to performing the ultrashort echo time (UTE) imaging, the gradient trajectories were measured using the ^{1}H signal. ^{19}F-UTE imaging [TR: 30.000 ms; Echo time (TE): 0.296 ms; flip angle: 15.0°; averages: 30; matrix size: 32 × 32; FOV: (25 × 25) mm^2; slice thickness:

5 mm; total acquisition time: 9 min] was applied. Mean calculated ^{19}F-TPU signal intensities within ROIs were measured and normalized to the standard deviation (σ) of the noise (measured in the background).

Later, to assess the concomitant visibility of both ^{1}H and ^{19}F signals, MRI phantoms were produced by placing the obtained ^{19}F-TPU threads and fibers in a 15 mL falcon tube filled with water. ^{19}F signals were acquired using the ^{19}F-UTE sequence mentioned above with 90 averages. Qualitative ^{1}H-T$_2$-weighted images were acquired using a fast spin echo sequence [TR: 2197 ms; TE: 80 ms; echo spacing: 26 ms; acceleration factor: 8; matrix size: 180 x 180; FOV: (25 x 25) mm^2; slice thickness; 5 mm; total acquisition time: 6 min]. Imalytics Preclinical Software (Gremse-IT GmbH, Aachen, Germany) was employed for all the image analyses.

2.4.2. Enhancing ^{19}F-TPU fiber visibility

To find an optimum ^{19}F-UTE image quality, i.e., good signal-to-noise ratio (SNR), while keeping overall scan time within reasonable limits, a systematic investigation was performed to determine the amount of ^{19}F-TPU that needs to be incorporated in our vascular prosthesis textile scaffolds. Therefore, 1, 2, and 4 ^{19}F-TPU fibers were sewn on top of the prosthetic textile scaffold, which was initially composed of PVDF warp-knitted fibers and 0.2 % (w/w) SPION-PLGA coating. The samples were placed in a 15 mL falcon tube filled with water and monitored by employing the previously used ^{1}H-T$_2$-weighted and ^{19}F-UTE sequences.

2.4.3. Longitudinal monitoring of vascular prosthesis remodeling

As shown in Fig. 3, ^{19}F-TPU fibers were knitted onto the SPION-PLGA and PVDF textile scaffolds following three different designs (Design 1: four single ^{19}F-TPU fibers positioned at quarter points; Design 2: two couples of ^{19}F-TPU fibers positioned at half points; and Design 3: four couples of ^{19}F-TPU fibers positioned at quarter points). With these three designs, we aimed to investigate whether the ^{19}F SNR was influenced not only by the number of fibers within the FOV but also by their proximity or distance from each other. The samples were incubated in sterile PBS at 37 °C for 3 weeks. The same ^{19}F-UTE and ^{1}H-T$_2$-weighted sequence parameters were employed as during the above-described phantom measurements. T$_2$ relaxation times and the corresponding R$_2$ relaxation rates (T$_2^{-1}$) were calculated as previously described for the SPION-PLGA fiber degradation study.

2.4.4. Assessing the biocompatibility of the ^{19}F-TPU fibers

To investigate whether the novel ^{19}F-TPU fibers were biocompatible with the cellular components present in our vascular prosthesis, an in vitro cytotoxicity XTT assay was performed. HUASMCs and HUAECs were separately cultivated in sterile 24 well plates (Thermofisher Scientific, Massachusetts, USA) upon confluency. Subsequently, the cells were exposed to sterile SPION-PLGA and ^{19}F-TPU fibers using cell culture inserts with a pore size of 8.0 μm (Corning GmbH, Kaiserslautern, Germany) for 24 h. A negative control consisted of HUASMCs and HUAECs exposed to empty inserts. The colorimetric assay was quantitatively measured using a Tecan Infinite® 200 microplate reader (Tecan, Männedorf, Switzerland).

2.4.5. Longitudinal monitoring of TEVGs

TEVGs were monitored by hybrid ^{1}H/^{19}F MRI immediately after endothelialization of their lumen (day 1) as well as after 3 and 7 days. Prior to the MRI measurements, the bioreactor tubings containing the TEVGs were disconnected and clamped to facilitate placing the samples within the MRI bore. The same MR sequences as mentioned before, i.e., ^{1}H-T$_2$-weighted, ^{1}H-T$_1$-weighted, and ^{19}F-UTE sequences for imaging and ^{1}H MSME for T$_2$-mapping, were employed.

2.5. In vivo longitudinal hybrid assessment of implanted TEVGs

2.5.1. Subcutaneous implantation

Three inbred male Lewis rats (Janvier Labs, Le Genest-Saint-Isle,

France) of 12 weeks of age were employed for the evaluation and longitudinal monitoring of our vascular prostheses. Anesthesia was induced with 4–5 vol% of isoflurane combined with an O_2 flow rate of 4–5 L mL^{-1} and maintained with 2.5–3 vol% of isoflurane and 1 mL^{-1} of O_2. After shaving the dorsum of the animals and applying an antiseptic spray, 2 mg kg^{-1} of Ropivacaine was injected to ensure local anesthesia. SPION-PLGA coated PVDF scaffolds additionally labeled with ^{19}F-TPU and containing syngeneic rat SMCs and ECs (TEVG_SPION-TPU) and their counterpart lacking SPIONs labeling (TEVG_TPU) were inserted in 1.5 cm pouches obtained below the skin on the right and on the left part of the rat dorsum, respectively. The ^{1}H/^{19}F MRI longitudinal investigation was performed under isoflurane anesthesia on days 1, 7, 14, and 21 after the subcutaneous implantation of the TEVGs. The animals were euthanized after 21 days to perform histological analyses.

^{1}H-T_2-weighted and ^{1}H-T_1-weighted anatomical images were acquired using a T_2-weighted fast spin echo sequence [TR: 1300 ms; TE: 25 ms; echo spacing: 8.3 ms; acceleration factor: 8; matrix size: 180 x 180; FOV: (70 x 70) mm^2; slice thickness: 5 mm; total acquisition time: 4 min] and a T_1-weighted fast spin echo sequence [TR: 200 ms; TE: 2.9 ms; flip angle: 30°; matrix size: 180 x 180; FOV: (70 x 70) mm^2; slice thickness: 5 mm; total acquisition time: 5 min], respectively. T_2 relaxometry was performed using a MSME sequence [TR: 4123 ms; TE: 6.4 ms; echo spacing: 6.4 ms; echo images: 40; number of averages: 1; matrix size: 144 x 80; FOV: (70 x 70) mm^2; slice thickness: 5 mm; total acquisition time: 5 min]. To decrease the total scan time, the number of averages for the ^{19}F-UTE sequence was decreased from 90 to 50 while maintaining sufficient SNR.

2.5.2. Aortic TEVGs implantation

As a proof of concept, 2 Lewis male rats of ~350 g weight underwent laparotomy to insert TEVGs as aortic vascular grafts in the infrarenal region of the abdominal aorta. One animal received the TEVG_SPION-TPU, the other one TEVG labeled with only SPION-PLGA (TEVG_-SPION). Briefly, the animals received pre-surgery analgesia by 5 mg kg^{-1} s.c. Injection of carprofen®. The analgesic effect was assured for at least 3 days after the surgery. After induction of the anesthesia by isoflurane inhalation, the animals were intubated using a Viggo endotracheal tube (Viggo Medical Devices, New-Dehli, India) to ensure mechanical ventilation throughout the entire surgical procedure. After shaving and disinfecting the area of interest, the abdominal cavity was opened, and the abdominal aorta was exposed and separated. The TEVGs were sutured onto the native arterial wall. Subsequently, the patency of the vascular prosthesis was tested by ligating the abdominal aorta at the TEVGs insertion area and removing the upstream surgical clamp. The amount of lost fluid throughout the surgery was replaced by saline. The wound was sutured and disinfected, and the animals were monitored closely for the following days. ^{1}H/^{19}F MRI and ultrasound (US) were performed under isoflurane anesthesia on days 4, 11, and 18 after the surgery (day 0). The animals were euthanized after 18 days to perform histological analyses.

Respiratory gating was applied to the same MR sequences used during the previous in vivo study (subcutaneous TEVGs) to reduce motion artifacts while monitoring TEVGs implanted in the infrarenal region of the abdominal aorta. US imaging was performed using a VEVO 3100 preclinical US system equipped with a linear-array-MX-250 transducer (FUJIFILM VisualSonics, Toronto, Ontario, Canada). The US investigation was performed by placing the transducer perpendicularly to the floor and on the right side of the animal, allowing sagittal view of the TEVG and ligated rat abdominal aorta. The patency of the TEVGs as aortic vascular grafts in the infrarenal region of the abdominal aorta was assessed in B-mode at 21 MHz frequency, 4 % power, and 100 frames. Power Doppler US was used to detect blood flow within the implanted TEVGs at 16 MHz frequency, pulse repetition frequency 25 kHz, Doppler gain 36 dB, 100 % power, and 100 frames. The echo power was calculated as a percentage related to 100 % vascularity by drawing an ROI on TEVGs and ligated abdominal aortas using the VevoLAB software version 5.2 (FUJIFILM

VisualSonics, Toronto, Ontario, Canada).

2.6. Mass spectrometry investigation of SPION-PLGA fiber degradation

Paraffin-embedded samples collected during in vitro and in vivo evaluation of our TEVGs were coated with α-cyano-4-hydroxycinnamic acid (Bruker Daltonic, Germany) as a matrix (10 mg mL^{-1} dissolved in 70 % ACN/0.2 % TFA). The coating process was performed using a MALDI imaging sprayer (HTX TM-Sprayer: TMSP-M3, HTX Technologies, USA). MALDI data were accumulated using a TOF-TOF-mass spectrometer (Rapiflex; Bruker-Daltonic, Bremen, Germany) equipped with a SmartbeamTM 3D laser with a 10 kHz repetition rate and controlled by the Flex-Control 4.0 (Bruker-Daltonic, Germany). Mass spectra were acquired with 1200 laser shots for each raster point and a digitizer rate of 5.0 GS s^{-1} in reflector-positive and a mass range of 300-3200 Da.

Data analysis was performed using SCiLS Lab software (SCiLS Lab-2022b; SCiLS GmbH; Bremen, Germany) and Flex-Analysis 4.0 (Bruker-Daltonic, Bremen, Germany). MALDI MSI raw data sets were converted to the SCiLS SL file format. The baseline was calculated by an iterative top hat, and normalization was performed based on the total ion count (TIC) method. Peptides were identified through the MS/MS spectra using the lift option of the Rapiflex mass spectrometer (Bruker-Daltonic, Bremen, Germany). The mass spectra were calibrated and annotated using BioTools 3.2 (Bruker-Daltonic, Bremen, Germany) in combination with SwissProt (University of Geneva, Switzerland) and the MASCOT 2.2 database (Matrix Science, London, UK) comparing experimental mass-spectrometric data with calculated peptide masses for each entry into the sequence database.

2.7. Histology

All the samples were fixed in Carnoy's solution and embedded in paraffin blocks. A microtome (Microm HM 430, Thermofisher Scientific, Massachusetts, USA) was used to obtain 5 μm thick sections, which were later collected from a water bath using glass object slides (Thermofisher Scientific, Massachusetts, USA). Prior to adding the primary antibodies of choice, the samples were deparaffinized with xylene and ethanol, blocked and permeabilized using 5 % normal goat serum (Agilent Dako, Santa Clara, California, USA) mixed with 0.1 % Triton X-100 aqueous solution. The primary antibodies were incubated at room temperature for 1 h (anti-rat and human α-smooth muscle actin (αSMA), anti-rat and human elastin, anti-rat collagen I, anti-rat and human collagen III, anti-rat and human collagen IV, anti-rat F4/80, and anti-rat CD3; Acris Antibodies GmbH, Herford, Germany; Abcam, Berlin, Germany; Thermofisher Scientific, Massachusetts, USA). After extensive washing with PBS, secondary antibodies were added at room temperature for 45 min (Alexa Fluor 488 and Alexa Fluor 594 labeled anti-mouse IgG and anti-rabbit IgG antibodies; Thermofisher Scientific, Massachusetts, USA). DAPI (Thermofisher Scientific, Massachusetts, USA) was used to stain the nuclei. The slides were mounted using a fluorescent mounting medium (Agilent Dako, Santa Clara, California, USA). A different protocol was used to stain F4/80 and CD3. After blocking and permeabilization, samples were incubated with anti-F4/80 or anti-CD3 (Bio-Rad, Düsseldorf, Germany, and Abcam, Berlin, Germany) at room temperature for 1 h. After washing, anti-Horseradish Peroxidase (HRP) secondary antibodies (Abcam, Berlin, Germany) were applied at room temperature for 45 min. As following step, a Cy5 tyramine signal amplification (TSA)-conjugated dye (PerkinElmer, USA), diluted with an amplification diluent buffer (PerkinElmer, USA), was added for 10 min. DAPI (Thermofisher Scientific, Massachusetts, USA) was added for 5 min to stain the nuclei. After washing, the slides were mounted with Mowiol (Carl-Roth, Karlsruhe, Germany) mixed with DAPI (Merck, Germany).

To perform H&E staining, samples were incubated with Eosin G 0.5 % in water for 30 min, followed by extensive washing under running water for 20 min to stain the ECM components. Hematoxylin was added for 5 min to stain the nuclei (Eosin G 5 % and Hematoxylin, Carl Roth

GmbH, Karlsruhe, Germany).

Masson's trichrome and Von Kossa staining were performed using a Masson's trichrome stain kit (Abcam, Berlin, Germany) and Von Kossa stain kit (Abcam, Berlin, Germany), respectively, following the instructions of the manufacturer.

2.8. Microscopy

An Axio Imager M2 fluorescence microscope equipped with an AxioCam MRm Rev.3 camera (Carl-Zeiss, Oberkochen) with a magnification of 20× and Vectra® 3.0 Microscope Automated Quantitative Pathology Imaging were used to acquire representative images of stained tissue sections. Images were quantified via Fiji software (ImageJ, NIH) and inForm (Akoya Biosciences, Marlborough, Massachusetts, USA).

2.9. Statistical analysis

All in vitro samples were prepared and analyzed in triplicate (sample size = 3). For the in vivo subcutaneous study, power analysis was additionally performed using G* Power software (version 3.1.9.2) with a significance level of 0.05 (α err prob – type I error) and a statistical power of 0.8 (power 1-β err prob – type II error). This analysis indicated that 3 animals per group were necessary to ensure a significant difference of 20 % with a standard deviation of 5 %. In adherence to the principles of the 3Rs, i) 3 animals were used (Reduce), ii) to allow each animal to serve as its own sample and control simultaneously, TEVGs

labeled with both ^{19}F-TPU and SPIONs were implanted on the right side of the animal dorsum, and control TEVGs labeled with only ^{19}F-TPU were implanted on the left side (Reuse), and iii) syngeneic cells were harvested from these animals at the end of the longitudinal experiment to produce new TEVGs for future animal experiments (Recycle).

The results are presented as mean values ± standard deviations (SD). The analysis was performed using GraphPad Prism 8 (GraphPad Prism Software, San Diego, California, USA). The statistical comparison of two groups was performed using Student's t-test, while for multiple group analyses, one-way ANOVA (one-tailed) with a post-hoc correction test (Tukey) was applied as recommended by the software. Statistical significance was considered for values $p \leq 0.05$.

For the in vivo implantation of TEVGs in the infrarenal region of the abdominal aorta, no group comparison and statistical significance were performed due to the use of only 1 animal per group.

3. Results

3.1. Characterization of ^{19}F-TPU by hybrid $^1H/^{19}F$ MRI

The highly fluorinated polymer ^{19}F-TPU was intended to be used as permanent scaffold material. To better understand its MRI properties, it was first characterized in the form of rough granules, then as threads of approximately 3 mm, and finally as thin fibers of circa 1.5 mm diameter, as illustrated in Fig. 2A–C. The different production stages, from granules to polymeric fibers, significantly influenced MRI visibility, as
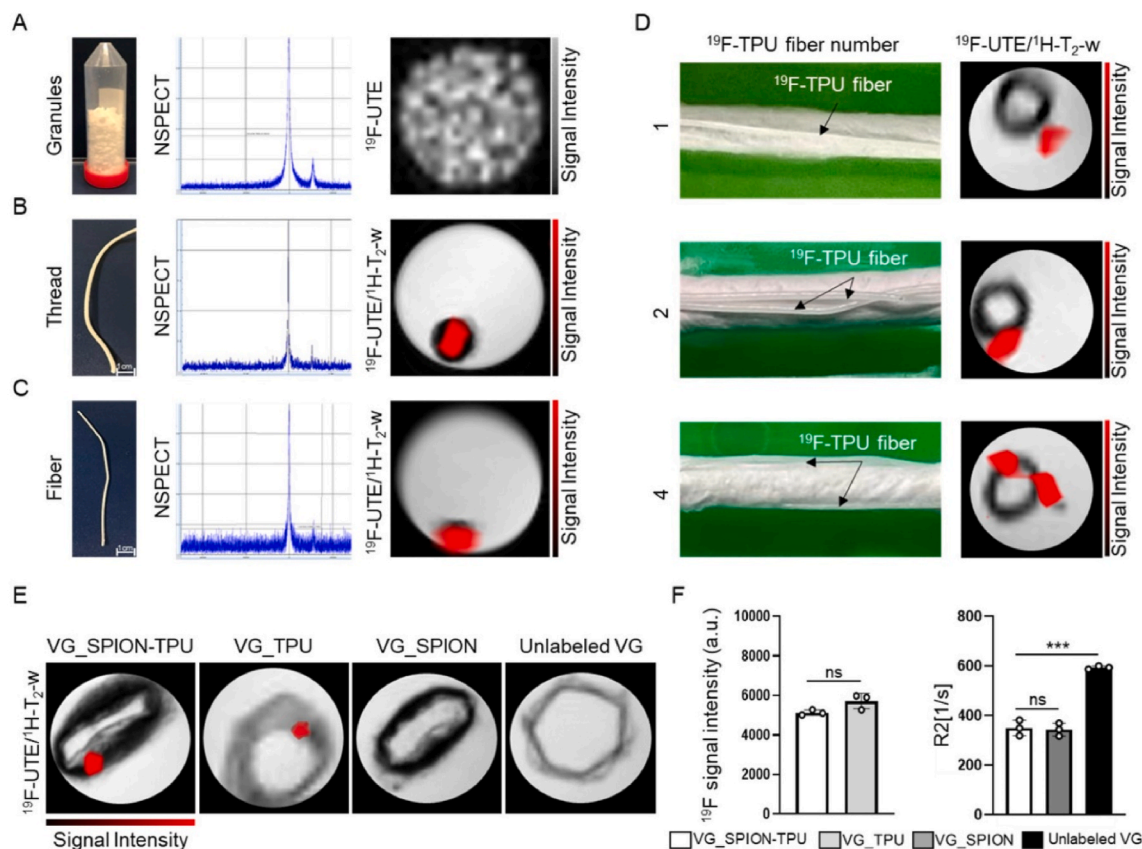

Fig. 2. Scaffold characterization with MRI. A-C) MR phantoms containing ^{19}F-TPU in the form of granules (A), threads (B), and fibers (C) exhibit the same NSPECT spectra, but with background noise that is inversely proportional to the amount of ^{19}F-TPU present in the sample. The ^{19}F-UTE "hot iron" images overlaying on grayscale ^1H-T_2-weighted images reflects the ^{19}F content within the phantoms. However, even for a single fiber, a distinct peak above the background noise is still detected. D) PVDF scaffolds coated with SPION-PLGA were additionally labeled with 1, 2, and 4 ^{19}F-TPU fibers, respectively. Hybrid $^1H/^{19}F$ MRI allows the detection of single ^{19}F-TPU fibers also in combination with other textile components. The ^{19}F signal improves if two or more fibers are positioned adjacently, due to the increase in ^{19}F-TPU per voxel. E) ^{19}F-UTE superimposed on ^1H-T_2-weighted images of VG_SPION-TPU, VG_SPION, and unlabeled VG show no interference or quenching between the two MR labels. F) Quantitative R_2 analyses confirm that SPION-PLGA does not influence the ^{19}F-TPU signal. All values were obtained in triplicates and are presented as means ± SD; One-way ANOVA with Tukey post hoc correction was applied to compare groups, indicating $p > 0.05$ as ns, $p < 0.05$ as *, $p < 0.01$ as **, $p < 0.001$ as ***, and $p < 0.0001$ as ****. Scale bar: 1 cm.

evidenced by the NSPECT spectra and the signal intensity obtained by ^{19}F-UTE sequences (granules: 17389 a.u.; thread: 6401 a.u.; fiber: 5144 a.u.). However, a well-defined peak was still detected for single ^{19}F-TPU fibers by ^{1}H/^{19}F MRI, and a clear "hot spot" ^{19}F signal superimposed to a ^{1}H-T_2-weighted image was obtained by image post-processing with Imalytics Preclinical software.

Next, the ^{19}F-TPU fibers were evaluated as permanent imaging labels of mixed scaffolds consisting of a degradable (PLGA fibers) and a non-degradable component (PVDF scaffold). In this context, different ^{19}F-TPU fiber numbers and positions were considered to optimize scaffolds' visibility in MRI (Fig. 2D). For this purpose, ^{19}F-TPU fibers were knitted onto the pre-existing warp-knitted PVDF textile scaffolds, which were additionally coated with electrospun PLGA fibers. To increase the MRI visibility of the latter, otherwise lacking in contrast, 0.2 % (w/w) SPIONs were passively incorporated into the PLGA fibers' core during the electrospinning process as described previously [12]. Hybrid ^{1}H/^{19}F MRI confirmed the visibility of single ^{19}F-TPU fibers when combined with the other textile components, which may influence the detection of ^{19}F signal via susceptibility artifacts, i.e., blooming artifacts, that cause distortions or local signal changes. Furthermore, it was beneficial to cluster two or more ^{19}F-TPU fibers to increase the ^{19}F content per voxel (1 fiber: 5355 ± 49.7 a.u.; 2 fibers: 5821 ± 40.9 a.u.; 4 fibers: 7684 ± 29.6 a.u.), rather than having them evenly distributed over the scaffold.

To exclude an influence of SPION-PLGA on the ^{19}F-TPU contrast, we measured the ^{19}F-TPU signal intensity and T_2 relaxation rates (R_2) of vascular grafts consisting only of textile scaffold without cellular components (VG). We produced different phantoms as follows: 1) VG containing both MR labels, SPIONs and ^{19}F-TPU fibers (VG_SPION-TPU), 2) VG lacking the ^{19}F-TPU (VG_SPION), 3) VG without SPIONs (VG_TPU),

and 4) unlabeled VG consisting of only MRI non-visible polymers. As shown in Fig. 2E and F, the presence of the grafts' components, especially SPIONs, did not influence the ^{19}F-TPU signal intensity (VG_SPION-TPU: 5128 ± 44 a.u vs. VG_TPU: 5711 ± 317.2 a.u.) and the presence of ^{19}F-TPU did not alter the R_2 values of the samples (VG_SPION-TPU: 349.8 ± 25.3 s^{-1}; VG_SPION: 317.7 ± 21.1 s^{-1}; unlabeled VG: 593.7 ± 5.6 s^{-1}).

3.2. Longitudinal investigation of the vascular prosthesis by hybrid ^{1}H/^{19}F MRI

After it was ensured that both MR labels were concomitantly detectable without impairment, we performed additional in vitro experiments to evaluate temperature (37 and 70 °C), static or dynamic culturing, and degradation process (hydrolysis or enzymatic) as main variables affecting PLGA degradation. Faster PLGA fiber degradation occurred at higher temperatures. Dynamic culturing also accelerated PLGA fiber degradation, particularly evident at 37 °C. Although no statistically significant differences were observed among samples exposed to pH 5, trypsin, or the combination of both, a faster PLGA fiber hydrolysis was noted compared to statically conditioned samples (Fig. S1, Supporting Information).

Subsequently, we investigated whether the resorption of SPION-PLGA fibers could be longitudinally monitored and the ^{19}F signal of the permanent scaffold component (^{19}F-TPU) remained stable. As previously described, ^{19}F-TPU fibers were knitted onto the SPION-PLGA and PVDF textile scaffolds following three different designs to further investigate the effects of SPION-PLGA degradation on ^{19}F signal detection (Fig. 3). ^{19}F-TPU fiber signal intensities measured by ^{19}F-UTE
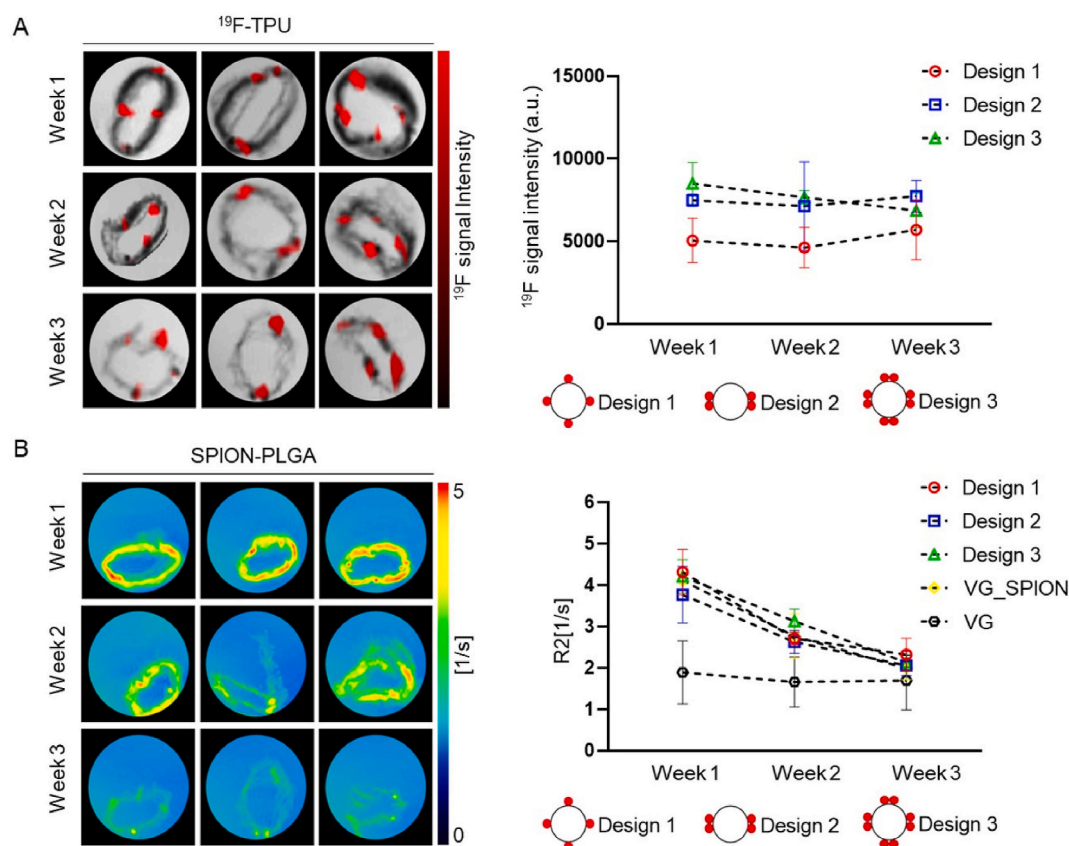

Fig. 3. Longitudinal evaluation of statically conditioned vascular prostheses. A) MR phantoms labeled with different numbers of ^{19}F-TPU fibers positioned in three different ways (Design 1–3). ^{19}F-UTE superimposed on T_2-weighted images show no statistically significant changes in ^{19}F-TPU fibers' signal intensity after 3 weeks of monitoring. B) R_2 colormaps superimposed to ^{1}H-T_2-weighted images show gradual degradation of the SPION-PLGA fibers in combination with ^{19}F-TPU fibers (VG_SPION-TPU Design 1–3) and without (VG_SPION). R_2 relaxometry confirms the SPION-PLGA degradation in comparison to the unlabeled counterpart. All values were obtained in triplicates and are presented as means ± SD; One-way ANOVA with Tukey post hoc correction was applied to compare groups.

sequence did not significantly change, indicating that the ^{19}F-TPU remained stable over the observation period (Fig. 3A; Table S1, Supporting Information). In contrast, PLGA fibers degraded throughout the observation time, which is clearly visible in R_2 colormaps superimposed to ^{1}H-T_2-weighted images (Fig. 3B; Table S1, Supporting Information). VG_SPION and unlabeled VG were used as additional negative controls (Fig. 3B; Table S1, Supporting Information). As postulated, the MR signal of ^{19}F-TPU remained constant throughout the observation period and was not influenced by the degrading SPION-PLGA fibers.

XTT cytotoxicity assays were employed to assess the biocompatibility of the ^{19}F-TPU fibers. As previously described, HUASMCs and HUAECs were exposed to the ^{19}F-TPU and SPION-PLGA fibers. Cells exposed to empty cell inserts were used as a negative control. The XTT revealed no difference in cell viability between both ^{19}F-TPU fiber exposed HUASMCs (100.3 ± 4.6 %) and HUAECs (97.3 ± 6.6 %) and unexposed negative control cells (HUASMCs: 101.4 ± 0.9 %; HUAECs: 95.4 ± 5.2 %) (Fig. 4A). SPION-PLGA fibers were also biocompatible but insignificantly tended to lower cell viability, as it was expected due to the generation of acidic degradation products (SPION-PLGA HUASMCs: 92.3 ± 3.2 %; SPION-PLGA HUAECs: 93.5 ± 9.7 %).

After confirming the biocompatibility of the imaging labels incorporated into the textile scaffold of our vascular prostheses and the

decision that Design 2 is ideal with respect to manufacturing and MR signal, complete biohybrid tissue-engineered vascular grafts (TEVGs) were produced by molding the textile scaffold with fibrin gel containing HUASMCs and introducing HUAECs for the endothelialization of the lumen. To longitudinally investigate the ^{19}F-TPU permanent MR signal and SPION-PLGA resorption, TEVGs were dynamically conditioned for 0, 3, and 7 days. No statistically significant changes in terms of ^{19}F-TPU fiber signal intensity were observed via ^{19}F-UTE and ^{1}H-T_2-weighted images superimposition (day 0: 7818 ± 1158 a.u.; day 3: 7106 ± 712.4 a.u.; day 7: 8701 ± 1196 a.u.) (Fig. 4B and C). Due to the presence of cellular components, a faster PLGA fibers degradation and, thus SPIONs release, was detected via a gradual decrease in the R_2 values depicted via quantitative R_2 colormaps (day 0: 4.8 ± 0.3 s^{-1}; day 3: 3.8 ± 0.3 s^{-1}; day 7: 2.7 ± 0.1 s^{-1}). The presence of cells and their metabolic and enzymatic activity contribute to the decrease in microenvironmental pH, which enhances the acidic hydrolysis of the PLGA fibers in comparison to previous samples containing no cells. Further histological analyses were performed to assess the impact of the presence of ^{19}F-TPU fibers on ECM components' production and deposition within our TEVGs with a particular focus on collagen I, III, and IV, and αSMA (Fig. S1, Supporting Information). For all these matrix components, a gradual increase in production and deposition was observed on day 7 in
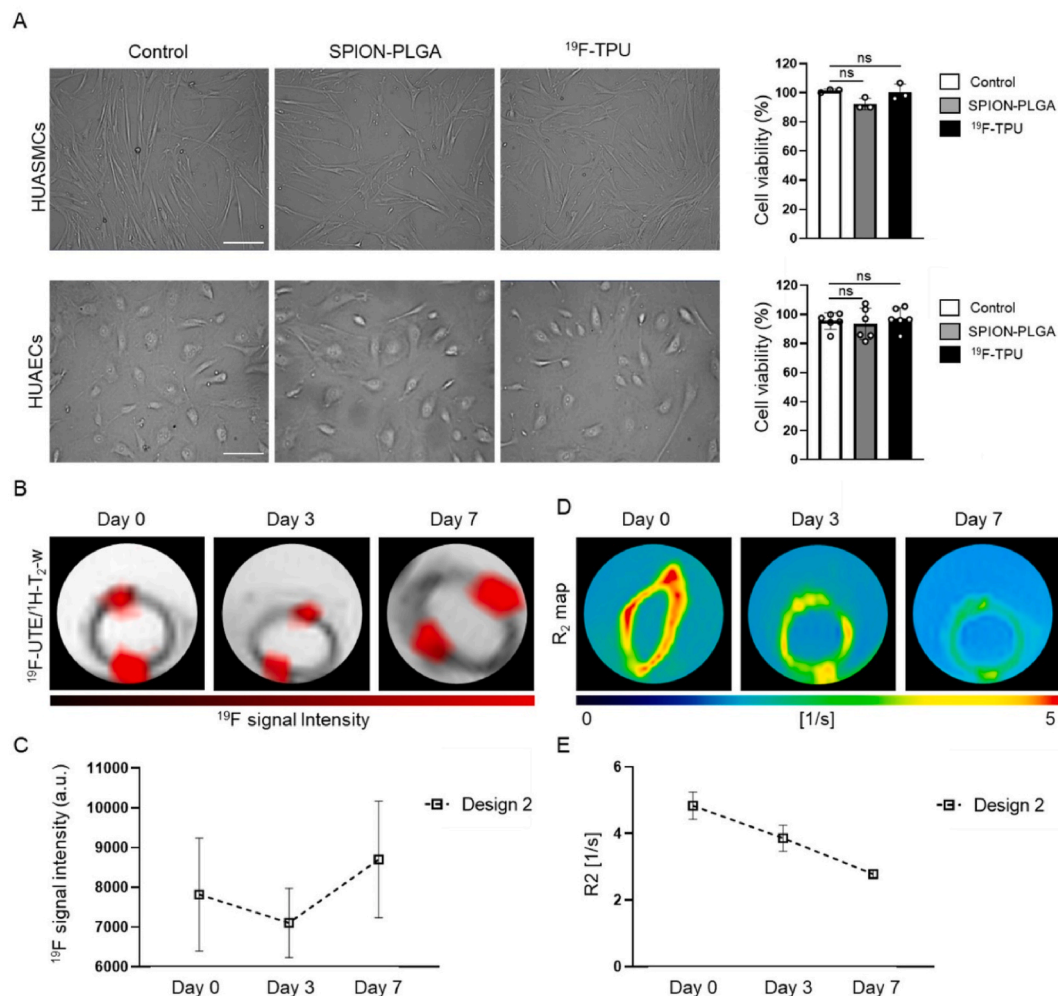

Fig. 4. Evaluation of ^{19}F-TPU biocompatibility and longitudinal monitoring of TEVGs under dynamic conditioning. A) Representative images of HUASMCs and HUAECs exposed to empty cell inserts, SPION-PLGA, or ^{19}F-TPU fibers. XTT shows no statistically significant differences in cell viability in both types of cells among the three groups. B) ^{19}F-UTE superimposed on grayscale ^{1}H-T_2-weighted images of TEVGs cultured for 7 days. C) ^{19}F-TPU related MR signal intensities remained stable over time. D-E) R_2 colormaps display gradual degradation of SPION-PLGA fibers. All values were obtained in triplicates and are presented as means ± SD; One-way ANOVA with Tukey post hoc correction was applied to compare groups, indicating p > 0.05 as ns, p < 0.05 as *, p < 0.01 as **, p < 0.001 as ***, and p < 0.0001 as ****. Scale bar: 500 μm.

comparison to day 0 (no bioreactor conditioning). Furthermore, a comparably increasing presence of major ECM components was observed in TEVGs containing both SPION-PLGA and ^{19}F-TPU (TEVG_SPION-TPU) and TEVGs only labeled with SPION-PLGA (TEVG_SPION), again confirming the biocompatibility of the ^{19}F-TPU fibers. Elastin production and deposition were additionally investigated (Fig. S2, Supporting Information). In contrast to the human umbilical artery, used as a positive control, no elastin fibers were present in all TEVGs, which is in line with previous findings [12].

3.3. Longitudinal in vivo evaluation of TEVGs by hybrid $^1H/^{19}F$ MRI

To confirm the in vivo translatability of our imaging approach and to ensure the permanent visibility of the ^{19}F-TPU fibers in vivo, three Lewis male rats were subcutaneously engrafted with TEVGs containing both MR labels, namely TEVG_SPION_TPU and TEVGs lacking SPIONs labeling (TEVG_TPU). The latter were used as a negative control to investigate the influence of SPIONs on the visibility of the ^{19}F-TPU fibers. As illustrated in Fig. 5A, the TEVG_SPION_TPU samples (in red) were subcutaneously implanted on the right side of the dorsum of the animals, while the TEVG_TPU counterparts (in blue) were engrafted on the left side. ^{19}F-TPU fibers remained visible without significant changes in signal intensity by hybrid $^1H/^{19}F$ MRI with no differences between TEVG_SPION-TPU and TEVG_TPU indicating that the SPIONs did not affect the ^{19}F MR signal (Fig. 5B; Table S2, Supporting Information). TEVG_SPION_TPU showed higher R_2 values than the TEVG_TPU counterpart due to the substantial decrease in T_2 generated by SPIONs (Fig. 5C; Table S2, Supporting Information). In comparison to the TEVG_TPU, whose R_2 values remained constant, in TEVG_SPION_TPU, R_2 progressively decreased throughout the observation time (Fig. 5C; Table S2, Supporting Information). The body weight of the rats, expressed in grams (g), was not altered over the examination period indicating that their well-being was not strongly impaired and highlighting the biocompatibility of the implanted prostheses (Fig. 5D).

TEVG_SPION-TPU and their TEVG_TPU counterparts were harvested at the end of the in vivo longitudinal MR investigation (Fig. 6C and D). TEVGs only labeled with SPION-PLGA (TEVG_SPION) and their unlabeled equivalent lacking all MR labels were used as additional negative controls (Fig. 6A and B). The latter were unpublished samples from a previous study [12]. Ex vivo immunofluorescence and histological analyses were performed to further investigate TEVG_SPION_TPUs' impact on living organisms. Hematoxylin and eosin (H&E) stains show strong endogenous cellular infiltration and prosthesis colonization, facilitating its integration within the host organism (Fig. 6). The total amount of collagen was investigated via Masson's trichrome staining in parallel to collagen III and IV, as major ECM components known to strongly influence vascular prostheses functionality. An abundant presence of various collagen types was observed, highlighting the strong maturation process that TEVGs underwent in vivo. Since αSMA is important for the contractility of blood vessels and can influence the production and deposition of ECM components via paracrine signaling and mechanical interactions, syngeneic smooth muscle cells (SMCs), derived from mesenchymal adipose stem cells of donor animals, were incorporated into the fibrin gel of our TEVGs. αSMA was also strongly observed in all TEVGs. No statistically significant differences were observed among the samples for all analyzed markers, suggesting that our imaging labels do not disturb the remodeling process (Fig. S3, Supporting Information).

To investigate the immune reaction of the host organisms toward our four models of TEVGs, the total number of macrophages (F4/80 positive cells) and T-cells (CD3 positive cells) was evaluated. After 21 days of in vivo implantation, a comparatively low number of immune cells was observed across all samples. The low inflammation and few phagocytic macrophages present within our samples can be attributed to the reduced presence of PLGA debris, which was also confirmed via MS (see

Fig. S4, Supporting Information). Our TEVGs exhibited a lower immune response in comparison to synthetic grafts, known for their poor performance, compliance mismatch, and non-biocompatible composition [28–31]. Hence, synthetic grafts are characterized by graft failure rates between 70 % and 100 % at 10–15 years of long-term follow-up [32].

To further investigate the in vivo feasibility of our imaging approach and study the performance and integration of our TEVGs within the host organism, two Lewis male rats underwent laparotomy and were engrafted with TEVG_SPION_TPU and TEVG_SPION in the infrarenal region of the abdominal aorta, respectively. The surgery occurred on day 0, followed by MRI and US on days 4, 11, and 18 (Fig. 7A). The inner diameter of the TEVGs was further decreased to 1.5 mm to avoid a significant mismatch with the native vessel (Fig. 7B). As depicted in Fig. 7C, due to unexpected stiffness caused mainly by the four ^{19}F-TPU fibers, the design of the TEVGs textile scaffold had to be changed accordingly, integrating only one ^{19}F-TPU fiber. Furthermore, as evidenced by the photo taken on day 18, the TEVGs retained their shape even though completely integrated within newly deposited ECM and remained functional and patent until the end of the experiment. As expected, the MRI signal from the ^{19}F-TPU fiber was visible only for TEVG_SPION_TPU, while no ^{19}F signal could be detected for TEVG_SPION. The ^{19}F MRI signal intensity of TEVG_SPION_TPU remained constant without any changes throughout the 18 days of observation time (Fig. 7D and E: TEVG_SPION_TPU day 1: 5185 a.u.; day 18: 5781 a. u.). On the other hand, SPION-PLGA of both TEVG_SPION_TPU and TEVG_SPION displayed decreasing R_2 values over time indicating degradable fibers resorption in both types of implanted TEVGs (Fig. 7D–F: TEVG_SPION_TPU day 1: 21.1 s^{-1}; day 11: 18.5 s^{-1}; day 18: 14.5 s^{-1}; TEVG_SPION day 1: 19.2 s^{-1}; day 11: 17.7 s^{-1}; day 18: 14.6 s^{-1}). Notably, it was increasingly challenging to visualize the TEVG_SPION as the SPIONs signal gradually decreased, highlighting the significant advantage of labeling the grafts' scaffold with the permanent ^{19}F-TPU fibers. As shown in Fig. 7G, Power Doppler US was performed to additionally investigate perfusion of our TEVGs. Blood flow within the TEVGs was confirmed by calculating the echo power (%) in the vascular graft and comparing it with the ligated abdominal aorta (Fig. 7H: TEVG_SPION_TPU and TEVG_SPION: 28.1 %; ligated abdominal aortas: 1.9 %). As shown in Fig. 7I, the animals exhibited a reduction in body weights (g) by 10.3 % and 10.9 % for the rats implanted with TEVG_SPION and TEVG_SPION_TPU, respectively. However, the weight loss can be attributed to the loss of fluids during surgery, a phenomenon observed in humans as well [33]. The well-being of both rats was reflected by the stabilization of the body weight within 7 days post-surgery. Further ex vivo histological analyses were performed to investigate TEVGs remodeling and integration within the host organism as well as new ECM deposition and possible loss of graft patency or graft calcification (Fig. 7J). H&E, alongside immunofluorescence staining for collagen III, αSMA, and elastin revealed abundant new ECM. Notably, elastin-positive cells were exclusively observed in TEVGs implanted in the infrarenal region of the abdominal aorta. Further elastin deposition and maturation into fiber-like structures may be detectable after longer monitoring. This aligns with our previous findings, where no elastin production was observed during 14 days of in vitro bioreactor conditioning and 21 days of subcutaneous implantation of TEVGs, respectively [12]. These data suggest that only the intense interplay between stronger mechanical stresses induced by arterial blood flow, constructive signaling molecules (i.e., matrix-bound nanovesicles), and inflammatory cells through the secretion of cytokines and growth factors stimulate a more intense remodeling of TEVGs, thus boosting an initial production of elastin. Von Kossa staining was additionally performed to investigate calcium deposits within the vascular prostheses and surrounding tissues. While Von Kossa staining detected calcification in the ligated rat abdominal aorta (RAA), no such deposits were observed within our vascular prostheses.
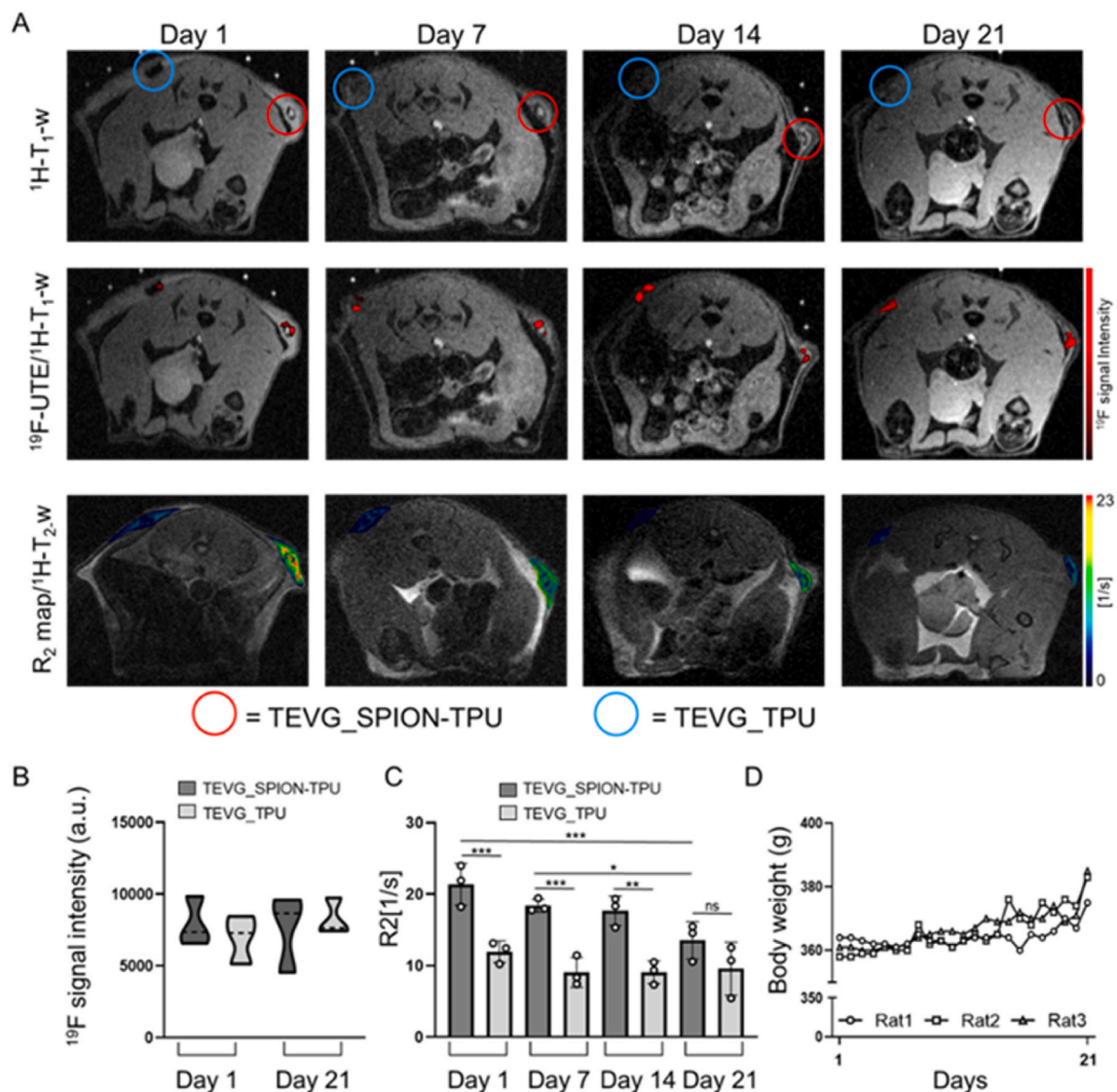
Fig. 5. Longitudinal in vivo monitoring of TEVGs by hybrid ^{1}H/^{19}F MRI. A) Representative ^{1}H-T$_1$-weighted images, ^{19}F-UTE superimposed on ^{1}H-T$_1$-weighted images, and R$_2$ colormaps superimposed on ^{1}H-T$_2$-weighted images show the temporal evolution of ^{19}F-TPU signal intensity and SPION-PLGA relaxometry throughout the 21 days of MR longitudinal monitoring. TEVG_SPION-TPU are encircled in red, whereas the samples highlighted in blue contain TEVG_TPU. B) The quantification of ^{19}F-TPU signal intensities of TEVG_SPION-TPU and TEVG_TPU samples at the beginning and end of the experiment reveal no significant alterations. The violin plot shows the frequency distribution of the data, and its width corresponds with the approximate frequency of data points in each region. C) R$_2$ relaxometry shows the degradation of the SPION-PLGA compared to plain PLGA throughout the 21 days of observation. D) Animal body weight was not negatively affected by the surgical procedure and the implanted prostheses. All values were obtained in triplicates and are presented as means ± SD; One-way ANOVA with Tukey post hoc correction was applied to compare groups, indicating $p > 0.05$ as ns, $p < 0.05$ as *, $p < 0.01$ as **, $p < 0.001$ as ***, and $p < 0.0001$ as ****. (For interpretation of the references to color in this figure legend, the reader is referred to the Web version of this article.)

It is crucial to note that this study provides only mere initial evidence of the potential applications of our imaging approach. Further studies are necessary to statistically validate these initial findings on larger animal cohorts.

4. Discussion

The field of tissue engineering is evolving toward more complex and multifaceted 3D constructs to meet the needs of the highly heterogeneous patient population. Here, TEVGs are promising as they enable high standardization on one hand, but also personalization, in vivo remodeling, and adaptation on the other. Furthermore, they can improve in vivo durability and reduce thrombogenic and adverse immunogenic effects, which often characterize fully synthetic grafts [34–37]. Biohybrid TEVGs are composed of a non-degradable synthetic scaffold and a biodegradable and biocompatible textile component to allow prosthesis maturation. In our previous work, we developed a comprehensive imaging approach to enhance the MRI visibility and the possibility for long-term monitoring of the resorption of our biodegradable component, namely PLGA fibers, by passive incorporation of SPIONs [12]. We observed that the in vitro and in vivo resorption of the PLGA fibers correlated with the decrease of the R$_2$ values indicating the release of the SPIONs. Nonetheless, once the SPION-PLGA fibers were entirely degraded, we lost the information regarding the positioning and structural integrity of the implanted TEVGs. Therefore, we here suggest extending our imaging approach by knitting non-degradable ^{19}F-TPU fibers onto the pre-existing MRI inert PVDF scaffold.

Another aspect worth considering is that the production of autologous or syngeneic vascular grafts involves harvesting ECs and SMCs directly from patients. This approach offers immune compatibility, but
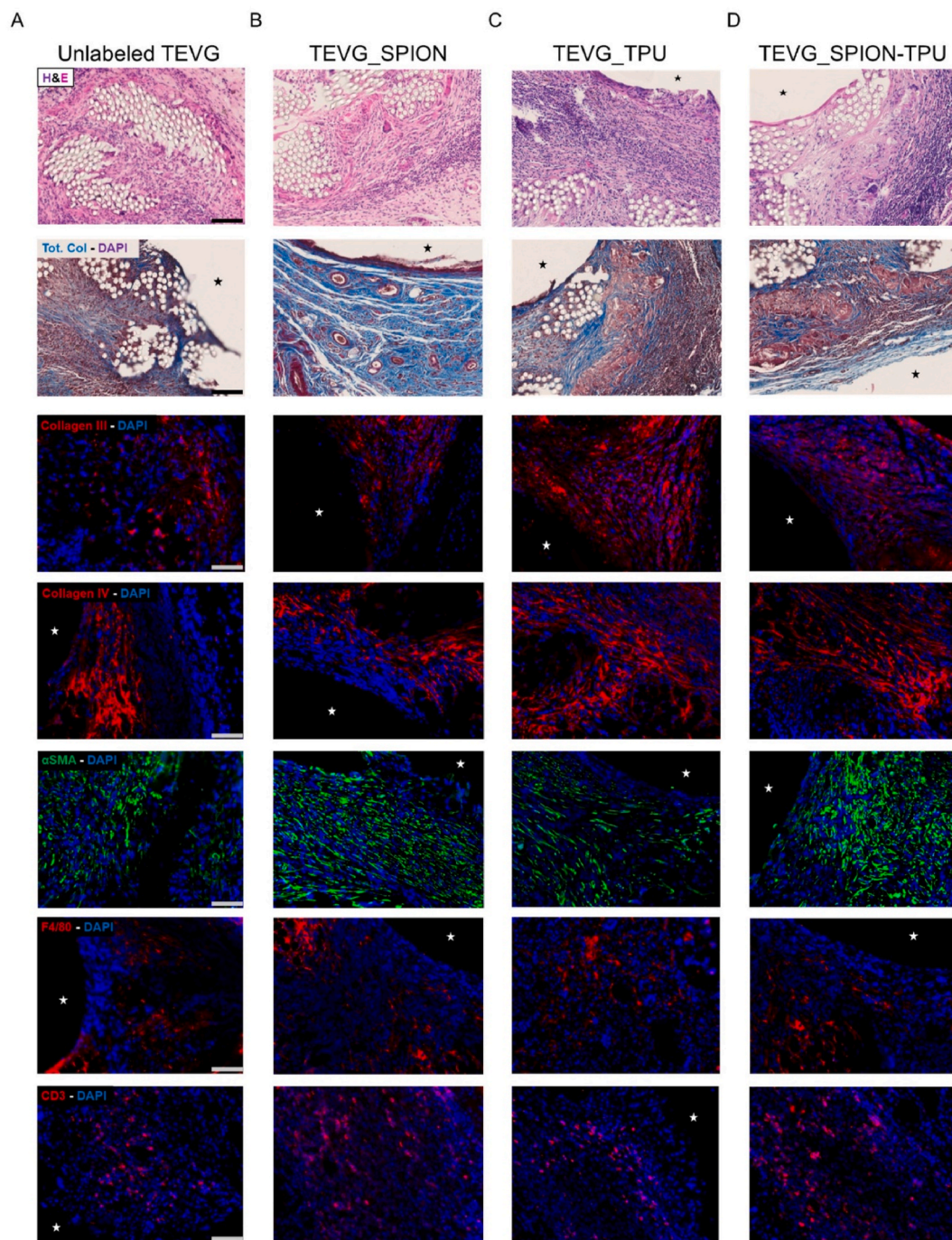
Fig. 6. Ex vivo histological analyses evaluating the effects of ^{19}F-TPU on ECM deposition and host reaction. A-B) Unlabeled TEVGs lacking both MR contrast agents used throughout this study (A) and TEVGs containing SPION-PLGA (TEVG_SPION, B) are used as negative controls. C) Vascular prostheses labeled with only the novel ^{19}F-TPU fibers (TEVG_TPU) were used as a supplementary negative control to exclude any additive, synergistic, or antagonistic effect between SPIONs and ^{19}F-TPU. D) Representative images of complete TEVGs labeled with both MR contrast agents, i.e., SPION-PLGA and ^{19}F-TPU fibers, (TEVG_SPION-TPU). H&E staining was performed to get an overview of ECM (in pink) and cell nuclei (in purple), highlighting the presence and infiltration of immune cells. The Masson's trichrome staining complementary shows total collagen in light blue, while nuclei are stained in purple. Fluorescence images in the bottom rows show collagen III and IV, F4/80, and CD3 in red, respectively, αSMA in green, and nuclei (DAPI) in blue. For all stainings no significant differences are observed, indicating that SPIONs incorporation into PLGA and ^{19}F-TPU does not change the body reactions after TEVGs implantation. Scale bar: 50 µm. The stars indicate TEVGs' lumen. (For interpretation of the references to color in this figure legend, the reader is referred to the Web version of this article.)

also implies invasive biopsies, limited cell quantity, and expensive and time-consuming culturing. Pluripotent/multipotent stem cells present a valuable alternative. For example, mesenchymal stem cells (MSCs) have been used to derive SMCs via chemical and mechanotransduction signals to mimic the tunica media of native vessels and secret anti-inflammatory factors [38]. However, harvesting enough MSCs remains challenging,

and moving toward progenitor cell in vivo maturation and differentiation requires a deeper understanding of their biointerfaces and crosstalks. These hurdles prompted interest in the production of in situ off-the-shelf implants. To confer immunocompatibility and off-the-shelf availability, grafts are processed via decellularization, depleting the cells but leaving the ECM architecture unmodified.
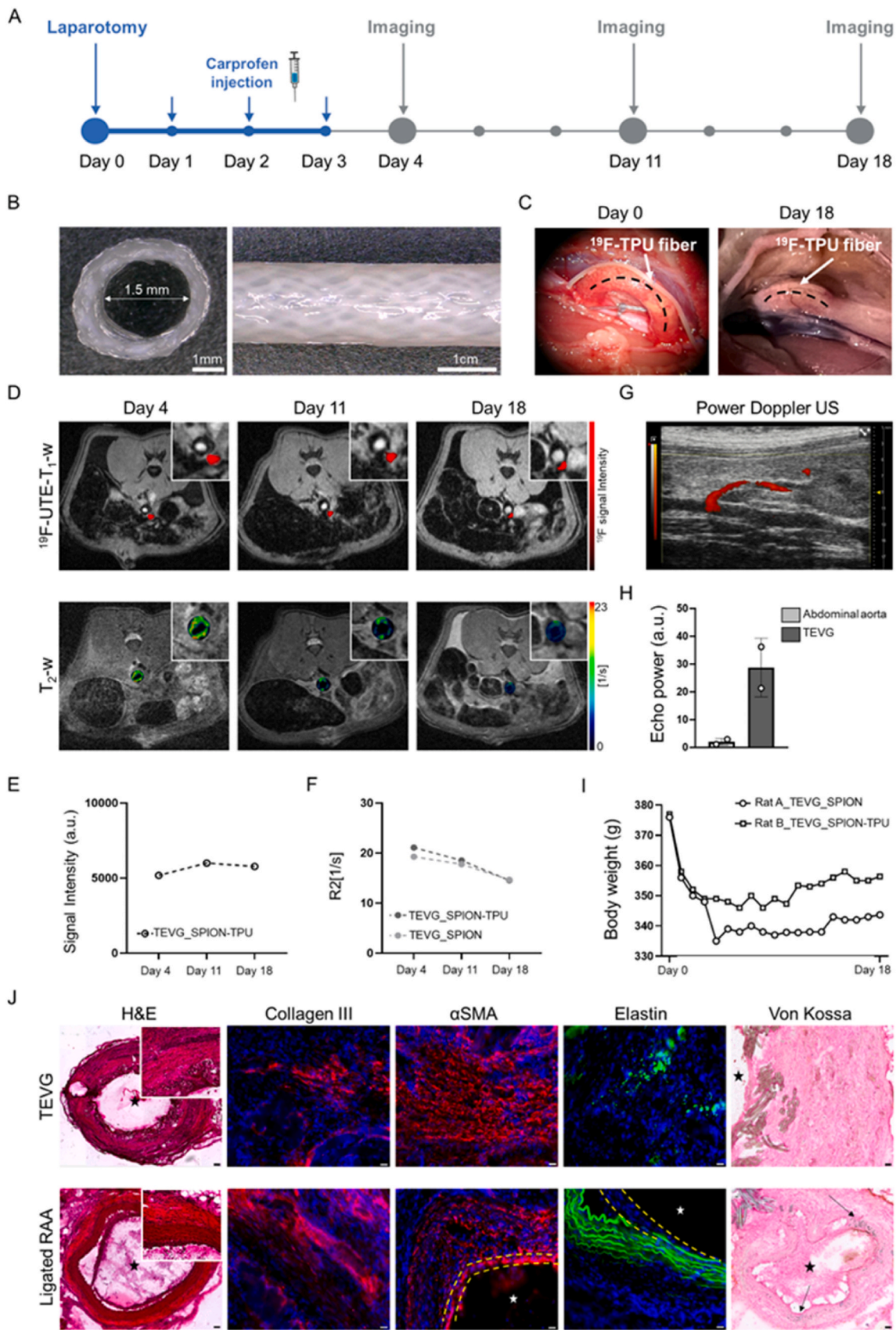
(caption on next page)

Fig. 7. Longitudinal in vivo monitoring of TEVGs implanted in the abdominal aorta. A) Schematic representation of the timeline of the animal experiments. B) Photos of a TEVG before implantation with inner diameter of 1.5 mm, wall thickness of 0.7 mm, and length of 4 cm, with the latter being decreased during the surgery at the discretion of the surgeons. C) TEVG implanted in the infrarenal region of the abdominal aorta labeled with only one ^{19}F-TPU fiber at day 0 and day 18. D) Representative ^{19}F-UTE superimposed on ^{1}H-T$_1$-weighted images show the permanent signal provided by the ^{19}F-TPU fiber. At the same time, R$_2$ colormaps superimposed on ^{1}H-T$_2$-weighted images demonstrate the SPION-PLGA degradation over time. E) The quantification of ^{19}F-TPU signal intensity of the TEVG_SPION-TPU confirms no significant change. F) R$_2$ relaxometry indicates the degradation of the SPION-PLGA in both TEVG_SPION_TPU and TEVG_SPION. G) Power Doppler US displays blood flow within the TEVGs. H) The echo power calculated from the Power Doppler videos indicates blood flow only within the TEVGs. I) A reduction of the animals' body weight was observed after surgery explained by the loss of liquids during the laparotomy. The animals started to stabilize and regain weight after the first week post-op. J) H&E (ECM in pink and nuclei in purple) as well as collagen III (in red), αSMA (in red), and elastin (in green) exhibit significant deposition of new ECM components and graft integration within the host organism. Dotted lines have been used to highlight the location of the intima where possible, aiming to clarify that αSMA and elastin are not expressed in the tunica intima of vessels but within the media. The presence of a small tunica intima may be attributed to underdevelopment within our TEVGs and damage in the ligated rat abdominal aorta (RAA). Von Kossa staining (calcification in black) depicts no calcium deposits that might impair the functionality of the vascular prostheses. In contrast, initial calcium deposits were observed in the ligated RAA, highlighted by the black arrows. H&E overview scale bar: 600 μm; Collagen III, αSMA, and elastin scale bar: 50 μm; Von Kossa scale bar: 200 μm. The stars indicate TEVGs' lumens. (For interpretation of the references to color in this figure legend, the reader is referred to the Web version of this article.)

Although the approaches of decellularization and recellularisation could potentially simplify the production of vascular prostheses, several studies suggested that decellularized scaffolds are more costly and could potentially elicit an immunogenic response, leading to graft failure, due to the presence of xenogeneic debris [39,40] Further research is needed to determine the most effective approach for achieving controlled tissue remodeling, scaffold degradation, selective cell recruitment, adhesion, and differentiation, leading to native-like tissues.

Despite our promising results, ^{19}F-TPU is characterized by elasticity and stickiness, hindering its spinnability. During our examinations, we observed that the stretching of the polymer during the production of thinner fibers is enough to cause a complete loss of ^{19}F MRI signal (unpublished data). Even though no crystallization peak was observed in the differential scanning calorimetry (DSC) curves (unpublished data), we hypothesize that the heating and manipulation of the polymer through extruders, followed by cooling on winders, provoke conformational changes in the disposition of the ^{19}F atoms, limiting their movements. To address this problem, further investigations will explore textile fibers composed of a ^{19}F-TPU core and an outer shell consisting of a polymer with excellent spinnability characteristics, such as PVDF or polyethylene terephthalate.

Hybrid ^{1}H/^{19}F MRI is typically susceptible to chemical shift artifacts due to the difference in resonance frequencies between ^{1}H and ^{19}F nuclei, leading to misregistration or misalignment of the images, and signal interference due to the presence of both nuclei in the same region of interest [41,42]. Moreover, the combination with iron-based contrast agents (i.e., SPIONs) can produce artifacts due to magnetic field inhomogeneities and iron susceptibility to magnetic fields, leading to geometric distortions, signal voids, and blooming effects [43]. These artifacts can affect image quality and interpretation, potentially compromising the diagnostic accuracy of MRI scans. Additionally, the lower gyromagnetic ratio and relaxation properties of ^{19}F MRI, which lead to lower sensitivity and thus, longer measurement times, along with the need for custom-built radiofrequency coils tuned to the ^{19}F resonance frequency (40.05 MHz/T), have limited the ^{1}H/^{19}F MRI clinical application to date [19,20]. However, as evidenced by our in vitro and in vivo investigations, the combination of our oleic-acid coated SPIONs with ^{19}F-TPU fibers does not cause any relevant interference or artifacts, highlighting the potential of our approach to foster ^{19}F MRI clinical translation.

In our study, a double-tuned ^{1}H/^{19}F volume coil with limited sensitivity to ^{19}F compared to other coil designs was used. Here improved MRI hardware, pulse sequences, broadband amplifiers, coils, and post-processing and image reconstruction software may help us to reduce the scan time and increase ^{19}F MRI sensitivity in the future. For example, different groups already suggested to modify the quadrature mode of birdcage coils, employing shingled-leg coil design, combining two coils using magnetic coupling, inserting shields and dielectric materials into the coil design, or using PIN-diodes switches [44–47].

^{19}F MRI could also be combined with other non-invasive and non-destructive imaging modalities, such as US, positron emission tomography (PET), and single-photon emission computed tomography (SPECT), providing precise quantification, high sensitivity, functional information, low background, and high resolution without expected interference. For example, studies already showed the potential of a hybrid ^{19}F MRI and PET approach for precise and accurate imaging of inflammation, or ^{19}F MRI and SPECT to improve diagnostic accuracy and guided therapy [48,49]. Furthermore, as already published by different groups, the combined application of ^{19}F MRI and US might also provide valuable insights into the integrity or disruption of the vessel endothelial lining, hyperplasia of the intima, development of atherosclerosis and thrombosis by foam cell formation, and acute or chronic inflammation [50–54].

The biocompatibility of our labeled TEVGs was demonstrated in vitro, in vivo, and ex vivo via XTT assay, visual assessment of the post-surgery incisions, and histology results. Despite SPIONs' desirable characteristics, such as biodegradability and tailorable accumulation and retention time, they are known to potentially induce reactive oxygen species (ROS) formation if not coated with biocompatible materials. ROS formation can potentially cause cell-cell signaling interference, gene transcription alteration, necrosis, and apoptosis [55]. Previous studies conducted by our group investigated scaffolds labeled with iron oxide nanoparticles (SPIONs and ultrasmall superparamagnetic iron oxide nanoparticles, USPIOs) via in vivo hybrid positron emission tomography-computed tomography (PET-CT) and ex vivo immunofluorescence analyses showing no in situ inflammation or differences with the unlabeled counterparts [13,56]. Furthermore, in line with previous findings by Rama et al. our follow-up study demonstrates that PLGA fibers labeled with SPIONs, coated with oleic acid to avoid aggregation, toxicity, and immunogenicity, do not elicit an inflammatory reaction upon in vivo implantation [12]. As recently reported, the employment of oleic acid as a coating material of iron nanoparticles protects cells from SPIONs-induced ROS and cell death [57]. Nonetheless, further studies are still required to evaluate long-term SPIONs toxicity toward different cells and tissues and, consequently, identify the most effective strategy to engineer SPIONs' surface and coating [58].

^{19}F-labeled polymers or contrast agents are widely investigated as fluorine is chemically inert and, based on current knowledge, non-immunogenic [59,60]. Although fluorine is known to interact with calcium, abundant in bones and teeth, ^{19}F-TPU fibers, not exposed to the lumen of the vascular prostheses, are not expected to undergo significant metabolism and biotransformation. However, the calcification of non-degradable polymers has been described as a significant issue affecting the function and long-term durability of vascular implants [61–63]. Therefore, further studies are deeply needed to investigate the potential calcification within our TEVGs in a longer monitoring period.

Fluorinated surfaces are also well-known for their non-adhesive nature. They possess very low surface energy, which makes them highly hydrophobic and minimizes interactions with polar molecules, including water, proteins, and cells [64,65]. This non-adhesive property

might yield advantages, such as reduced hyperplasia of the intima, risk of blood clot formation, stenosis, thrombosis, and inflammation, as well as negative implications, such as reduced cell-material interactions, which can be detrimental when designing materials for TE. Thus, to avoid hindering cell attachment and growth as well as TEVGs integration within the host organism, we opted to use ^{19}F-TPU fibers as an MRI label instead of producing a textile scaffold completely consisting of ^{19}F-TPU. Furthermore, the chemical, physical, and morphological properties of the TEVGs textile scaffold's surface might also play an important role in cellular response upon implantation. Different studies have extensively explored tailoring polymer characteristics, such as wettability, hydrophobicity, adhesivity, and topography, to influence protein adsorption, cell attachment, function, and matrix formation while also reshaping cytokine profile and immune cell activation, which is pivotal for maintaining a balance between wound healing, tissue regeneration, and implant rejection [8,66]. In this regard, our TEVGs, with and without ^{19}F-TPU fibers, were found to evoke a comparable number of infiltrated immune cells, similar ECM content, and no altered cellular behavior, indicating no cellular toxicity and a comparable immune system response most probably due to balanced wettability, hydrophobicity, adhesivity, and overall biocompatibility of our TEVGs, even with the inclusion of ^{19}F-TPU fibers within the textile scaffold. Nonetheless, further studies are still needed to fully characterize ^{19}F-TPU from a material point of view and functionalize its surface to achieve enhanced biocompatibility via controlled adhesion and specific cell-material or material-material interactions.

5. Conclusions

In this manuscript, we introduce a concept for the complementary non-invasive longitudinal assessment of cardiovascular implants using ^{1}H/^{19}F MRI. Our approach makes TEVGs visible by biocompatible MRI labels, enabling simultaneous monitoring of the degradation and remodeling process while preserving essential information about the positioning and structural integrity. Moreover, we demonstrate the feasibility of imaging TEVGs with an inner diameter of 1.5 mm that can be produced and implanted in the rat abdominal aorta. This highlights that our TEVGs may even be used for small human vessels, such as the coronary arteries. Our approach is applicable in vivo and holds promise for enhancing clinical translation by offering an innovative and specific non-invasive monitoring method for textile scaffolds.

CRediT authorship contribution statement

Elena Rama: Writing – review & editing, Writing – original draft, Visualization, Validation, Methodology, Investigation, Formal analysis, Data curation, Conceptualization. **Saurav Ranjan Mohapatra:** Methodology, Investigation, Conceptualization. **Yukiharu Sugimura:** Methodology, Investigation, Conceptualization. **Tomoyuki Suzuki:** Methodology, Investigation. **Stefan Siebert:** Methodology, Investigation. **Roman Barmin:** Methodology, Investigation, Conceptualization. **Juliane Hermann:** Methodology, Investigation, Data curation. **Jasmin Baier:** Methodology, Investigation. **Anne Rix:** Methodology, Investigation. **Teresa Lemainque:** Methodology, Investigation, Conceptualization. **Susanne Koletnik:** Methodology, Investigation. **Asmaa Said Elshafei:** Methodology, Investigation. **Roger Molto Pallares:** Methodology, Investigation, Conceptualization. **Seyed Mohammadali Dadfar:** Methodology, Investigation. **René H. Tolba:** Project administration. **Volkmar Schulz:** Methodology, Conceptualization. **Joachim Jankowski:** Supervision, Investigation, Data curation. **Christian Apel:** Methodology, Investigation, Conceptualization. **Payam Akhyari:** Supervision, Data curation, Conceptualization. **Stefan Jockenhoevel:** Supervision, Data curation, Conceptualization. **Fabian Kiessling:** Writing – review & editing, Supervision, Project administration, Funding acquisition, Conceptualization.

Declaration of generative AI and AI-assisted technologies in the writing process

During the preparation of this work the author(s) used ChatGPT/OpenAI in order to improve language and readability. After using this tool/service, the author(s) reviewed and edited the content as needed and take(s) full responsibility for the content of the publication.

Declaration of competing interest

The authors declare that they have no known competing financial interests or personal relationships that could have appeared to influence the work reported in this paper.

Data availability

Data will be made available on request.

Acknowledgements

Appendix A. Supplementary data

Supplementary data to this article can be found online at https://doi.org/10.1016/j.biomaterials.2024.122669.

References

[1] G.A. Mensah, G.A. Roth, V. Fuster, The global burden of cardiovascular diseases and risk factors - 2020 and beyond, J. Am. Coll. Cardiol. 74 (2019) 2529–2532, https://doi.org/10.1016/j.jacc.2019.10.009.

[2] C.W. Tsao, A.W. Aday, Z.I. Almarzooq, C.A.M. Anderson, P. Arora, C.L. Avery, C. M. Baker-smith, A.Z. Beaton, A.K. Boehme, A.E. Buxton, Y. Commodore-mensah, M.S.V. Elkind, K.R. Evenson, C. Eze-nliam, S. Fugar, G. Generoso, N.S. Shah, E. L. Thacker, S.S. Virani, Heart disease and stroke statistics — 2023 update : a Report from the American heart association. https://doi.org/10.1161/CIR.000000000000 1123, 2023.

[3] L.E. Niklason, J.H. Lawson, Bioengineered Human Blood Vessels, 2020, p. 8682, https://doi.org/10.1126/science.aaw8682.

[4] J.T. Patterson, T. Gilliland, M.W. Maxfield, S. Church, Y. Naito, T. Shinoka, Tissue-engineered vascular grafts for use in the treatment of congenital heart disease : from the bench to the clinic and back again, Futur. Med. (n.d.) 409–419.

[5] C.E.T. Stowell, Y. Wang, Quickening: Translational Design of Resorbable Synthetic Vascular Grafts, 2018, p. 7330.

[6] P. Zilla, M. Deutsch, D. Bezuidenhout, N.H. Davies, T. Pennel, Progressive reinvention or destination lost ? Half a century of cardiovascular tissue engineering, Front. Cardiovasc. Med. 7 (2020) 1–32, https://doi.org/10.3389/fcvm.2020.00159.

[7] J.D. Drews, V.K. Pepper, C.A. Best, J.M. Szafron, J.P. Cheatham, A.R. Yates, K. N. Hor, J.C. Zbinden, Y. Chang, G.J.M. Mirhaidari, A.B. Ramachandra, S. Miyamoto, K.M. Blum, E.A. Onwuka, J. Zakko, J. Kelly, S.L. Cheatham, N. King, J.W. Reinhardt, T. Sugiura, H. Miyachi, Y. Matsuzaki, J. Breuer, E.D. Heuer, T. A. West, T. Shoji, D. Berman, B.A. Boe, J. Asnes, M. Galantowicz, G. Matsumura, N. Hibino, A.L. Marsden, Spontaneous reversal of stenosis in tissue-engineered vascular grafts, Sci. Transl. Med. 12 (2020) 1–14.

[8] F. Zhang, M.W. King, Immunomodulation strategies for the successful regeneration of a tissue-engineered vascular graft, Adv. Healthcare Mater. 11 (2022) 1–24, https://doi.org/10.1002/adhm.202200045.

[9] J.G. Bartolacci, M.N. Behun, J.P. Warunek, T. Li, A. Sahu, G.K. Dwyer, A. Lucas, J. Rong, F. Ambrosio, H.R. Turnquist, S.F. Badylak, Matrix-bound nanovesicle-

associated IL-33 supports functional recovery after skeletal muscle injury by initiating a pro-regenerative macrophage phenotypic transition, Npj Regen. Med. 9 (2024), https://doi.org/10.1038/s41536-024-00346-2.

[10] U. Jehn, K. Schuette-nuetgen, D. Kentrup, V. Hoerr, S. Reuter, Renal allograft rejection : noninvasive ultrasound- and MRI-based diagnostics, Contrast Media Mol. Imaging 2019 (2019).

[11] Kilian M.A. Mueller, Geoffrey J. Topping, Sebastian P. Schwaminger, Younzhe Zou, Diana M. Rojas-Gonzalez, Elena M. De-Juan-Pardo, Sonja Berensmeier, Franz Schilling, Petra Mela, Visualization of USPIO-labeled melt-electrowritten scaffolds by non-invasive magnetic resonance imaging, Biomater. Sci. (2021) 4607–4612, https://doi.org/10.1039/d1bm00461a.

[12] E. Rama, S.R. Mohapatra, C. Melcher, T. Nolte, S.M. Dadfar, R. Brueck, V. Pathak, A. Rix, T. Gries, V. Schulz, T. Lammers, C. Apel, S. Jockenhoevel, F. Kiessling, Monitoring the remodeling of biohybrid tissue-engineered vascular grafts by multimodal molecular imaging, Adv. Sci. 9 (2022) 1–15, https://doi.org/10.1002/advs.202105783.

[13] F. Wolf, V. Paefgen, O. Winz, M. Mertens, S. Koch, N. Gross-Weege, A. Morgenroth, A. Rix, H. Schnoering, K. Chalabi, S. Jockenhoevel, T. Lammers, F. Mottaghy, F. Kiessling, P. Mela, MR and PET-CT monitoring of tissue-engineered vascular grafts in the ovine carotid artery, Biomaterials 216 (2019) 119228, https://doi.org/10.1016/j.biomaterials.2019.119228.

[14] R. Garnett, A comprehensive review of dual-energy and multi-spectral computed tomography, Clin. Imag. 67 (2020) 160–169, https://doi.org/10.1016/j.clinimag.2020.07.030.

[15] K. Rajendran, M. Petersilka, A. Henning, E.R. Shanblatt, B. Schmidt, T.G. Flohr, A. Ferrero, F. Baffour, F.E. Diehn, L. Yu, P. Rajiah, J.G. Fletcher, S. Leng, C. H. McCollough, First clinical photon-counting detector CT system: technical evaluation, Radiology 303 (2022) 130–138, https://doi.org/10.1148/RADIOL.212579.

[16] Y. Xiao, R. Paudel, J. Liu, C. Ma, Z. Zhang, S. Zhou, Int. J. Mol. Med. (2016) 1319–1326, https://doi.org/10.3892/ijmm.2016.2744. MRI contrast agents: Classification and application (Review).

[17] M. Jeon, M.V. Halbert, Z.R. Stephen, M. Zhang, Iron oxide nanoparticles as T1 contrast agents for magnetic resonance imaging: fundamentals, challenges, applications, and prospectives, Adv. Mater. 33 (2021) 1–18, https://doi.org/10.1002/adma.201906539.

[18] T. Shin, J. Choi, S. Yun, I. Kim, H. Song, Y. Kim, K. In Park, J. Cheon, T1 and T2 dual-mode MRI contrast agent for enhancing accuracy by engineered nanomaterials, ACS Nano (2014) 3393–3401.

[19] I. Tirotta, V. Dichiarante, C. Pigliacelli, G. Cavallo, G. Terraneo, F.B. Bombelli, P. Metrangolo, G. Resnati, 19F magnetic resonance imaging (MRI): from design of materials to clinical applications, Chem. Rev. 115 (2015) 1106–1129, https://doi.org/10.1021/cr500286d.

[20] C. Zhang, S.S. Moonshi, Y. Han, S. Puttick, H. Peng, B.J.A. Magoling, J.C. Reid, S. Bernardi, D.J. Searles, P. Král, A.K. Whittaker, PFPE-based polymeric 19F MRI agents: a new class of contrast agents with outstanding sensitivity, Macromolecules 50 (2017) 5953–5963, https://doi.org/10.1021/acs.macromol.7b01285.

[21] T. Lammers, M.E. Mertens, P. Schuster, K. Rahimi, V. Schulz, A.J.C. Kuehne, S. Jockenhoevel, F. Kiessling, Fluorinated polyurethane scaffolds for 19F magnetic resonance imaging, Chem. Mater. 29 (2017) 2669–2671, https://doi.org/10.1021/acs.chemmater.6b04649.

[22] S.R. Mohapatra, E. Rama, C. Melcher, T. Call, M.A. Al Enezy-Ulbrich, A. Pich, C. Apel, F. Kiessling, S. Jockenhoevel, From in vitro to perioperative vascular tissue engineering: shortening production time by traceable textile-reinforcement, Tissue Eng. Regen. Med. 19 (2022) 1169–1184, https://doi.org/10.1007/s13770-022-00482-0.

[23] M. Patel, A. Jha, R. Patel, Potential application of PLGA microsphere for tissue engineering, J. Polym. Res. 28 (2021), https://doi.org/10.1007/s10965-021-02562-6.

[24] S. Mohammadali, K. Roemhild, N.I. Drude, S. Von Stillfried, R. Knüchel, F. Kiessling, T. Lammers, Iron Oxide Nanoparticles : Diagnostic , Therapeutic and Theranostic Applications, 138, 2019, pp. 302–325, https://doi.org/10.1016/j.addr.2019.01.005.

[25] R. Hufschmid, H. Arami, R.M. Ferguson, M. Gonzales, E. Teeman, L.N. Brush, D. Browning, K.M. Krishnan, Synthesis of phase-pure and monodisperse ironoxide nanoparticles by thermal decomposition, Nanoscale (2015) 11142–11154, https://doi.org/10.1039/c5nr01651g.

[26] R.G. Marangoni, B. Korman, J. Varga, Adipocytic progenitor cells give rise to pathogenic myofibroblasts: adipocyte-to-mesenchymal transition and its emerging role in fibrosis in multiple organs, Curr. Rheumatol. Rep. 22 (2020), https://doi.org/10.1007/s11926-020-00957-w.

[27] S. Lin, K. Mequanint, Bioreactor-induced mesenchymal progenitor cell differentiation and elastic fiber assembly in engineered vascular tissues, Acta Biomater. 59 (2017) 200–209, https://doi.org/10.1016/j.actbio.2017.07.012.

[28] A.J. Collins, R.N. Foley, D.T. Gilbertson, S.C. Chen, United States Renal Data System public health surveillance of chronic kidney disease and end-stage renal disease, Kidney Int. Suppl. 5 (2015) 2–7, https://doi.org/10.1038/kisup.2015.2.

[29] A.F. Schild, E. Perez, E. Gillaspie, C. Seaver, J. Livingstone, A. Thibonnier, Arteriovenous fistulae vs. arteriovenous grafts: a retrospective review of 1,700 consecutive vascular access cases, J. Vasc. Access 9 (2008) 231–235, https://doi.org/10.1177/112972980800900402.

[30] R.L. Madden, G.S. Lipkowitz, B.J. Browne, A. Kurbanov, A comparison of cryopreserved vein allografts and prosthetic grafts for hemodialysis access, Ann. Vasc. Surg. 19 (2005) 686–691, https://doi.org/10.1007/s10016-005-6621-2.

[31] S.L.M. Dahl, A.P. Kypson, J.H. Lawson, J.L. Blum, J.T. Strader, Y. Li, R.J. Manson, W.E. Tente, L. DiBernardo, M.T. Hensley, R. Carter, T.P. Williams, H.L. Prichard,

[32] M.S. Dey, K.G. Begelman, L.E. Niklason, Readily available tissue-engineered vascular grafts, Sci. Transl. Med. 3 (2011), https://doi.org/10.1126/scitranslmed.3001426.

[33] T.S. Hirotsugu Kurobe, Mark W. Maxfield, Christopher K. Breuer, Concise review: tissue-engineered vascular grafts for cardiac surgery: past, present, and future, Stem Cells Transl. Med. 1 (2012) 566–571.

[34] B. Brandstrup, Fluid therapy for the surgical patient, Best Pract. Res. Clin. Anaesthesiol. 20 (2006) 265–283, https://doi.org/10.1016/j.bpa.2005.10.007.

[35] S. Cho, D.E. Discher, K.W. Leong, G. Vunjak-Novakovic, J.C. Wu, Challenges and opportunities for the next generation of cardiovascular tissue engineering, Nat. Methods 19 (2022) 1064–1071, https://doi.org/10.1038/s41592-022-01591-3.

[36] R.Z. Zhuang, R. Lock, B. Liu, G. Vunjak-Novakovic, Opportunities and challenges in cardiac tissue engineering from an analysis of two decades of advances, Nat. Biomed. Eng. 6 (2022) 327–338, https://doi.org/10.1038/s41551-022-00885-3.

[37] D. Kim, J.J. Chung, Y. Jung, S.H. Kim, The effect of Substance P/Heparin conjugated PLCL polymer coating of bioinert ePTFE vascular grafts on the recruitment of both ECs and SMCs for accelerated regeneration, Sci. Rep. (2019) 1–13, https://doi.org/10.1038/s41598-019-53514-6.

[38] T. Zhu, H. Gu, H. Zhang, H. Wang, H. Xia, X. Mo, J. Wu, Covalent grafting of PEG and heparin improves biological performance of electrospun vascular grafts for carotid artery replacement, Acta Biomater. 119 (2021) 211–224, https://doi.org/10.1016/j.actbio.2020.11.013.

[38] T.W. Hatem Jouda, Luis larrea murillo, clinical applications, Cells 11 (2022) 445–456.

[39] A. Porzionato, E. Stocco, S. Barbon, F. Grandi, V. Macchi, R. De Caro, Tissue-engineered grafts from human decellularized extracellular matrices: a systematic review and future perspectives, Int. J. Mol. Sci. 19 (2018), https://doi.org/10.3390/ijms19124117.

[40] X. Zhang, X. Chen, H. Hong, R. Hu, J. Liu, C. Liu, Decellularized extracellular matrix scaffolds: recent trends and emerging strategies in tissue engineering, Bioact, Mater 10 (2022) 15–31, https://doi.org/10.1016/j.bioactmat.2021.09.014.

[41] L. Wu, F. Liu, S. Liu, X. Xu, Z. Liu, X. Sun, Perfluorocarbons-based 19F magnetic resonance imaging in biomedicine, Int. J. Nanomed. 15 (2020) 7377–7395, https://doi.org/10.2147/IJN.S255084.

[42] C.H. Choi, S.M. Hong, J. Felder, N.J. Shah, The state-of-the-art and emerging design approaches of double-tuned RF coils for X-nuclei, brain MR imaging and spectroscopy: a review, Magn. Reson. Imaging 72 (2020) 103–116, https://doi.org/10.1016/j.mri.2020.07.003.

[43] A. Hahn, F.T. Kurz, Advanced Imaging/MRI for Tissue Engineering, third ed., Elsevier Ltd., 2021 https://doi.org/10.1016/B978-0-12-820508-2.00016-7.

[44] P. Bowyer, J. Finnigan, B. Marsden, B. Taber, A. Zens, Using magnetic coupling to implement 1H, 19F, 13C experiments in routine high resolution NMR probes, J. Magn. Reson. 261 (2015) 190–198, https://doi.org/10.1016/j.jmr.2015.10.010.

[45] S. Ha, M.J. Hamamura, O. Nalcioglu, L.T. Muftuler, A PIN diode controlled dual-tuned MRI RF coil and phased array for multi nuclear imaging, Phys. Med. Biol. 55 (2010) 2589–2600, https://doi.org/10.1088/0031-9155/55/9/011.

[46] L. Hu, F.D. Hockett, J. Chen, L. Zhang, S.D. Caruthers, G.M. Lanza, S.A. Wickline, A generalized strategy for designing 19F/1H dual-frequency MRI coil for small animal imaging at 4.7 Tesla, J. Magn. Reson. Imag. 34 (2011) 245–252, https://doi.org/10.1002/jmri.22516.

[47] P. Villa-Valverde, I. Rodríguez, D. Padró, M. Benito, C.E. Garrido-Salmon, J. Ruiz-Cabello, A dual 1 H/19 F birdcage coil for small animals at 7 T MRI, Magn. Reson. Mater. Physics, Biol. Med. 32 (2019) 79–87, https://doi.org/10.1007/s10334-018-00733-z.

[48] Z. Guo, M. Chen, C. Peng, S. Mo, C. Shi, G. Fu, X. Wen, R. Zhuang, X. Su, T. Liu, N. Zhang, X. Zhang, pH-sensitive radiolabeled and superfluorinated ultra-small palladium nanosheet as a high-performance multimodal platform for tumor theranostics, Biomaterials 179 (2018) 134–143, https://doi.org/10.1016/j.biomaterials.2018.06.040.

[49] C. Wang, B.I. Leach, D. Lister, S.R. Adams, H. Xu, C. Hoh, P. McConville, J. Zhang, K. Messer, E.T. Ahrens, Metallofluorocarbon nanoemulsion for inflammatory macrophage detection via PET and MRI, J. Nucl. Med. 62 (2021) 1146–1153, https://doi.org/10.2967/JNUMED.120.255273.

[50] A. Dasgupta, M. Liu, T. Ojha, G. Storm, F. Kiessling, T. Lammers, Ultrasound-mediated drug delivery to the brain: principles, progress and prospects, Drug Discov. Today Technol. 20 (2016) 41–48, https://doi.org/10.1016/j.ddtec.2016.07.007.

[51] D. Janasik, T. Krawczyk, 19F MRI probes for multimodal imaging, Chem. Eur J. 28 (2022), https://doi.org/10.1002/chem.202102556.

[52] R. Díaz-López, N. Tsapis, E. Fattal, Liquid perfluorocarbons as contrast agents for ultrasonography and 19F-MRI, Pharm. Res. (N. Y.) 27 (2010) 1–16, https://doi.org/10.1007/s11095-009-0001-5.

[53] A. Curaj, Z. Wu, S. Fokong, E.A. Liehn, C. Weber, A. Burlacu, T. Lammers, M. Van Zandvoort, F. Kiessling, Noninvasive molecular ultrasound monitoring of vessel healing after intravascular surgical procedures in a preclinical setup, Arterioscler. Thromb. Vasc. Biol. 35 (2015) 1366–1373, https://doi.org/10.1161/ATVBAHA.114.304857.

[54] A. Curaj, Z. Wu, A. Rix, O. Gresch, M. Sternkopf, S. Alampour-Rajabi, T. Lammers, M. Van Zandvoort, C. Weber, R.R. Koenen, E.A. Liehn, F. Kiessling, Molecular ultrasound imaging of junctional adhesion molecule A depicts acute alterations in blood flow and early endothelial dysregulation, Arterioscler. Thromb. Vasc. Biol. 38 (2018) 40–48, https://doi.org/10.1161/ATVBAHA.117.309503.

[55] V. Frantellizzi, M. Conte, M. Pontico, A. Pani, R. Pani, G. De Vincentis, New frontiers in molecular imaging with superparamagnetic iron oxide nanoparticles (SPIONs): efficacy, toxicity, and future applications, Nucl. Med. Mol. Imaging 54 (2010) 65–80, https://doi.org/10.1007/s13139-020-00635-w, 2020.

[56] M.E. Mertens, A. Hermann, A. Bühren, L. Olde-Damink, D. Möckel, F. Gremse, J. Ehling, F. Kiessling, T. Lammers, Iron oxide-labeled collagen scaffolds for non-invasive MR imaging in tissue engineering, Adv. Funct. Mater. 24 (2014) 754–762, https://doi.org/10.1002/adfm.201301275.

[57] N. Repar, E.J. Jovičić, A. Kump, G. Birarda, L. Vaccari, A. Erman, S. Kralj, S. Nemec, T. Petan, D. Drobne, Oleic acid protects endothelial cells from silica-coated superparamagnetic iron oxide nanoparticles (SPIONs)-Induced oxidative stress and cell death, Int. J. Mol. Sci. 23 (2022), https://doi.org/10.3390/ijms23136972.

[58] R. Vakili-Ghartavol, A.A. Momtazi-Borojeni, Z. Vakili-Ghartavol, H.T. Aiyelabegan, M.R. Jaafari, S.M. Rezayat, S. Arbabi Bidgoli, Toxicity assessment of superparamagnetic iron oxide nanoparticles in different tissues, Artif. Cells, Nanomedicine Biotechnol. 48 (2020) 443–451, https://doi.org/10.1080/21691401.2019.1709855.

[59] A. Mali, E.L. Kaijzel, H.J. Lamb, L.J. Cruz, 19F-nanoparticles: platform for in vivo delivery of fluorinated biomaterials for 19F-MRI, J. Contr. Release 338 (2021) 870–889, https://doi.org/10.1016/j.jconrel.2021.09.001.

[60] R. Holman, O. Lorton, P.C. Guillemin, S. Desgranges, C. Contino-Pépin, R. Salomir, Perfluorocarbon emulsion contrast agents: a mini review, Front. Chem. 9 (2022) 1–9, https://doi.org/10.3389/fchem.2021.810029.

[61] A. Lejay, B. Bratu, S. Kuntz, N. Neumann, F. Heim, N. Chakfé, Calcification of synthetic vascular grafts: a systematic review, EJVES Vasc. Forum. 60 (2023) 1–7, https://doi.org/10.1016/j.ejvsvf.2023.05.013.

[62] Y. Hayabuchi, K. Mori, T. Kitagawa, M. Sakata, S. Kagami, Polytetrafluoroethylene graft calcification in patients with surgically repaired congenital heart disease: evaluation using multidetector-row computed tomography, Am. Heart J. 153 (2007) 806.e1–806.e8, https://doi.org/10.1016/j.ahj.2007.01.035.

[63] A.A. Gostev, V.S. Chernonosova, I.S. Murashov, D.S. Sergeevichev, A.A. Korobeinikov, A.M. Karaskov, A.A. Karpenko, P.P. Laktionov, Electrospun polyurethane-based vascular grafts: physicochemical properties and functioning in vivo, Biomed. Mater. 15 (2020), https://doi.org/10.1088/1748-605X/ab550c.

[64] D.W. Grainger, C.W. Stewart, Fluorinatecl coatings and films: motivation and significance, ACS Symp. Ser. 787 (2001) 1–14, https://doi.org/10.1021/bk-2001-0787.ch001.

[65] H. Peng, I. Blakey, B. Dargaville, F. Rasoul, S. Rose, A.K. Whittaker, Synthesis and evaluation of partly fluorinated block copolymers as MRI imaging agents, Biomacromolecules 10 (2009) 374–381, https://doi.org/10.1021/bm801136m.

[66] S. Franz, S. Rammelt, D. Scharnweber, J.C. Simon, Immune responses to implants - a review of the implications for the design of immunomodulatory biomaterials, Biomaterials 32 (2011) 6692–6709, https://doi.org/10.1016/j.biomaterials.2011.05.078.

Supporting Information

In Vitro and *in Vivo* **Evaluation of Biohybrid Tissue-Engineered Vascular Grafts with Transformative ^{1}H/^{19}F MRI Traceable Scaffolds**

Elena Rama[a], Saurav Ranjan Mohapatra[b], Yukiharu Sugimura[c], Tomoyuki Suzuki[c], Stefan Siebert[b], Roman Barmin[a], Juliane Hermann[d], Jasmin Baier[a], Anne Rix[a], Teresa Lemainque[a,e], Susanne Koletnik[a], Asmaa Said Elshafei[a], Roger M. Pallares[a], Seyed Mohammadali Dadfar[a,f], René H. Tolba[g], Volkmar Schulz[a], Joachim Jankowski[d,h,i], Christian Apel[b], Payam Akhyari[c], Stefan Jockenhoevel[b] and Fabian Kiessling[a*]

[a] Institute for Experimental Molecular Imaging, Faculty of Medicine, RWTH Aachen University, Forckenbeckstraße 55, 52074 Aachen, Germany

[b] Department of Biohybrid & Medical Textiles, AME-Institute of Applied Medical Engineering, Helmholtz Institute, RWTH Aachen University, Forckenbeckstraße 55, 52074 Aachen, Germany

[c] Department of Cardiac Surgery, Medical Faculty and RWTH University Hospital Aachen, RWTH Aachen University, Aachen, Germany.

[d] Institute for Molecular Cardiovascular Research (IMCAR), University Hospital RWTH Aachen, Aachen, Germany

[e] Department of Diagnostic and Interventional Radiology, Medical Faculty, RWTH Aachen University, 52074 Aachen, Germany

[f] Ardena Oss, 5349 AB Oss, The Netherlands

[g] Institute for Laboratory Animal Science and Experimental Surgery, Faculty of Medicine, RWTH Aachen International University, Aachen, Germany

[h] Aachen-Maastricht Institute for CardioRenal Disease (AMICARE), University Hospital RWTH Aachen, Aachen, Germany

[i] Department of Pathology, Cardiovascular Research Institute Maastricht (CARIM), University of Maastricht, The Netherlands

* Corresponding author: Prof. Dr. Fabian Kiessling, MD, Institute for Experimental Molecular Imaging, Faculty of Medicine, RWTH Aachen University, Forckenbeckstraße 55, 52074 Aachen, Germany
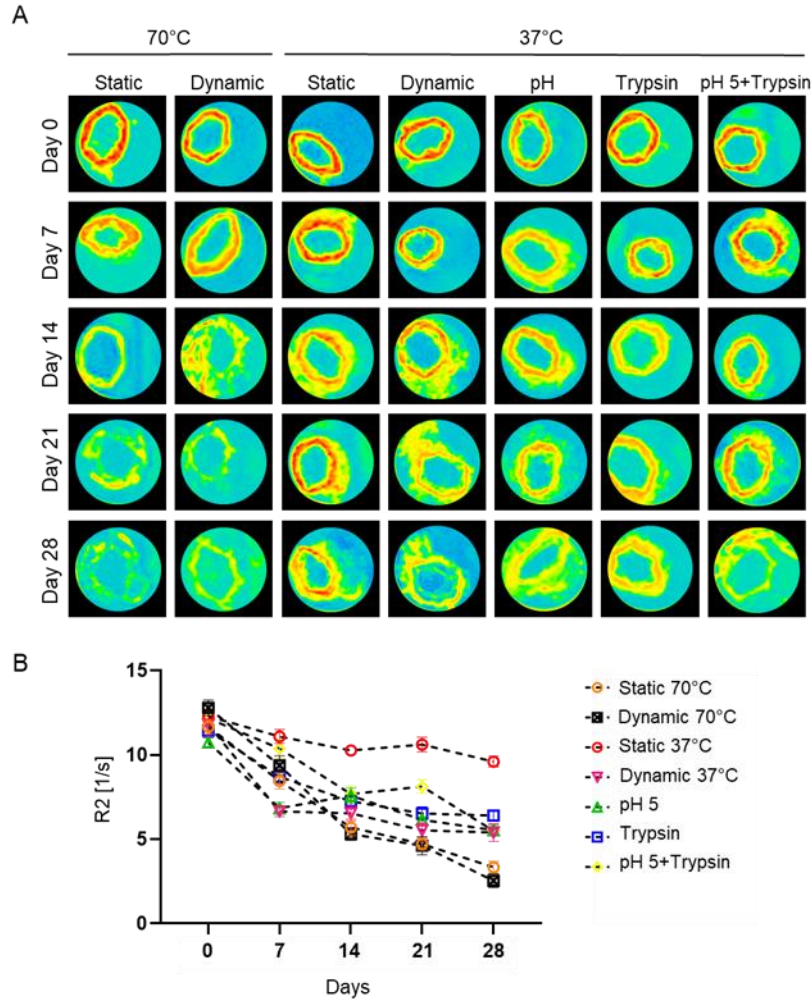Phone: +49 (0) 241 8080116. E-mail: fkiessling@ukaachen.de

Figure S1: MRI longitudinal monitoring of SPION-PLGA fiber degradation. A) R_2 colormaps show gradual degradation of SPION-PLGA fibers electrospun on PVDF tubular scaffolds exposed to different temperatures (37 and 70 °C), static or dynamic culturing, and different degradation process (hydrolysis or enzymatic) to evaluate these parameters as main variables affecting their degradation. Samples were monitored weekly via MRI for 4 weeks. B) Temperature plays an important role in the accelerating the PLGA fiber resorption, as evidenced by the loss of contrast in the R_2 colormaps and the decrease of the R_2 values over time (R_2 values for static 70°C day 0: (11.6 ± 0.3) s^{-1} versus day 28: (3.3 ± 0.2) s^{-1}; dynamic 70°C day 0: (12.7 ± 0.4) s^{-1} versus day 28: (2.5 ± 0.3) s^{-1}). Although the difference between static and dynamic culturing at 70°C was not substantial, this parameter played a significant role at 37°C (static 37°C day 0: (12.3 ± 0.3) s^{-1} versus day 28: (9.6 ± 0.3) s^{-1}; dynamic 37°C day 0: (11.8 ± 0.6) s^{-1} versus day 28: (5.4 ± 0.4) s^{-1}). Regarding the samples exposed to pH 5, trypsin, and the combination of pH 5 and trypsin, no statistically significant differences were observed. Nonetheless, a faster PLGA fiber degradation was observed in comparison to statically cultured samples at 37°C (pH 5 day 0: (10.7 ± 0.2) s^{-1} versus day 28: (5.5 ± 0.3) s^{-1}; trypsin day 0: (11.4

$\pm$ 0.3) s^{-1} versus day 28: (6.4 $\pm$ 0.3) s^{-1}; pH 5+trypsin day 0: (12.2 $\pm$ 0.2) s^{-1} versus day 28: (5.5 $\pm$ 0.2) s^{-1}).

Samples	^{19}F-TPU signal intensity (a.u.)		R_2 relaxation time (s^{-1})	
	First week	Third week	First week	Third week
Design 1	5048 $\pm$ 485	5688 $\pm$ 1786	4.3 $\pm$ 0.4	2.3 $\pm$ 0.3
Design 2	7475 $\pm$ 300	7725 $\pm$ 793	3.7 $\pm$ 0.5	2.1 $\pm$ 0.1
Design 3	8492 $\pm$ 1014	6862 $\pm$ 1010	4.2 $\pm$ 0.3	2.1 $\pm$ 0.1
VG-SPION	-	-	4.1 $\pm$ 0.1	1.9 $\pm$ 0.2
Unlabeled VG	-	-	1.8 $\pm$ 0.6	1.6 $\pm$ 0.5

Table S1: Signal intensities and R_2 changes of ^{19}F-TPU and SPION-PLGA fibers of three different designs, respectively. The samples were measured over a 3-week period during static cultivation. These designs involved knitting ^{19}F-TPU fibers onto SPION-PLGA and PVDF textile scaffolds. ^{19}F-TPU signal intensity did not significantly change, indicating that the ^{19}F-TPU remained stable over the observation period. On the contrary, R_2 relaxation time of SPION-PLGA fibers gradually decreased during the 3 weeks of monitoring indicating the degradation of the fibers.
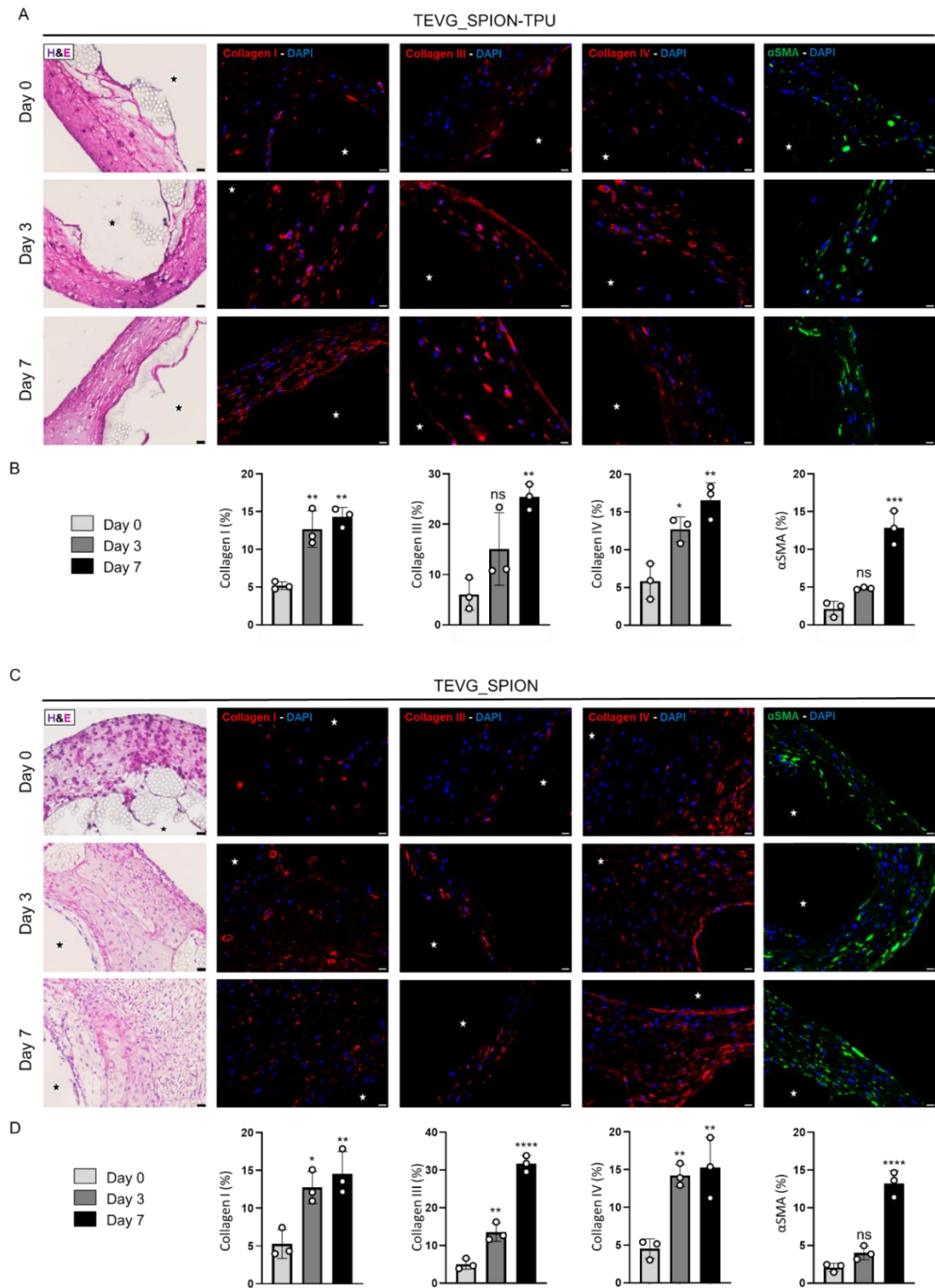
Figure S1: Immunofluorescence and H&E stainings exclude a prominent influence of ^{19}F-TPU on important ECM markers. A) TEVGs labeled with both contrast agents, i.e., TEVG_SPION-TPU, were stained to evaluate ECM development throughout the 3 observation time points (1, 3, and 7 days of bioreactor dynamic conditioning). Representative H&E images show nuclei in purple stained with haematoxylin and undifferentiated ECM components in pink

stained via eosin. Collagen I, III, and IV are depicted in red, αSMA in green, and nuclei in blue. B) A significant increase in production and deposition is observed for all the evaluated markers after 7 days of *in vitro* conditioning. C) TEVG_SPION are used as a negative control. D) Collagen I, III, IV and αSMA, show a statistically significant increase after 3 or 7 days of conditioning. Both TEVG_SPION-TPU and TEVG_SPION are similarly characterized by increased ECM components deposition, αSMA development, and textile scaffold remodeling. All values were obtained in triplicates and are presented as means ± SD; One-way ANOVA with Tukey post hoc correction was applied to compare groups, indicating $p > 0.05$ as ns, $p < 0.05$ as *, $p < 0.01$ as **, $p < 0.001$ as ***, and $p < 0.0001$ as ****. Scale bar: 20 μm. Stars indicate TEVGs' lumen. Statistical significance is reported as a comparison to the control samples (day 0).

Figure S2: Histological assessment of elastin fiber production and deposition in our TEVGs. Representative images of TEVG_SPION-TPU and TEVG_SPION, used as a negative control, show no elastin deposition is observed after 7 days of bioreactor dynamic conditioning. Human umbilical artery (HUA) was used as a positive control. Elastin fibers are depicted in green and nuclei in blue (DAPI). The scale bar is 20 μm. The stars indicate TEVGs' lumen. The employment of human samples was granted by the Ethical Committee approval (EK 2067).

Samples	^{19}F-TPU signal intensity (a.u.)		R_2 relaxation time (s^{-1})			
	Day 1	Day 21	Day 1	Day 7	Day 14	Day 21
TEVG_SPION_TPU	6957 ± 1374	8275 ± 1044	21.3 ± 2.3	18.3 ± 0.7	17.6 ± 1.6	13.5 ± 2.1
TEVG_TPU	7921 ± 3600	8594 ± 2990	11.9 ± 1.2	9.1 ± 1.7	9.1 ± 1.2	9.5 ± 3.1

Table S2: Signal intensities and R_2 changes of ^{19}F-TPU and SPION-PLGA fibers implanted subcutaneously in rats, respectively. The ^{19}F-TPU fibers remained visible without

significant changes in signal intensity. Additionally, no differences were observed between TEVG_SPION-TPU and TEVG_TPU. However, TEVG_SPION_TPU exhibited higher R_2 values compared to its TEVG_TPU counterpart, which is attributed to the SPIONs contrast. Notably, while the R_2 values of TEVG_TPU remained constant, those of TEVG_SPION_TPU progressively decreased throughout the observation period.
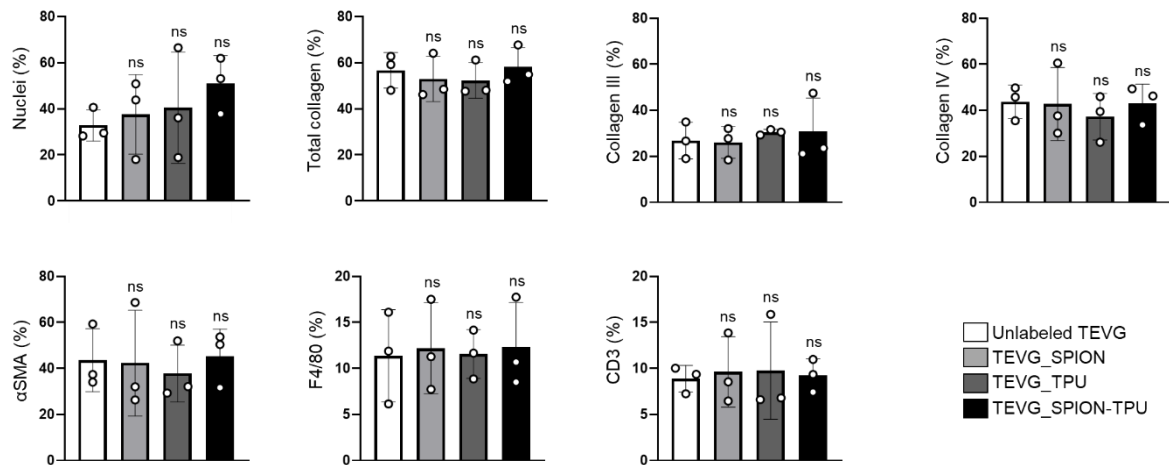

Figure S3: *Ex vivo* **histological quantification of ECM components, cell infiltration, and host immune response.** No statistically significant differences were observed for number of nuclei, thus cells, and total amount of collagen, in particular collagen III and IV. Furthermore, the amounts of αSMA, macrophages, and T-cells are comparable. All values were obtained in triplicates and are presented as means ± SD; One-way ANOVA with Tukey post hoc correction was applied to compare groups, indicating $p > 0.05$ as ns, $p < 0.05$ as *, $p < 0.01$ as **, $p < 0.001$ as ***, and $p < 0.0001$ as ****. Statistical significance is reported as a comparison to the control samples (unlabeled TEVG).
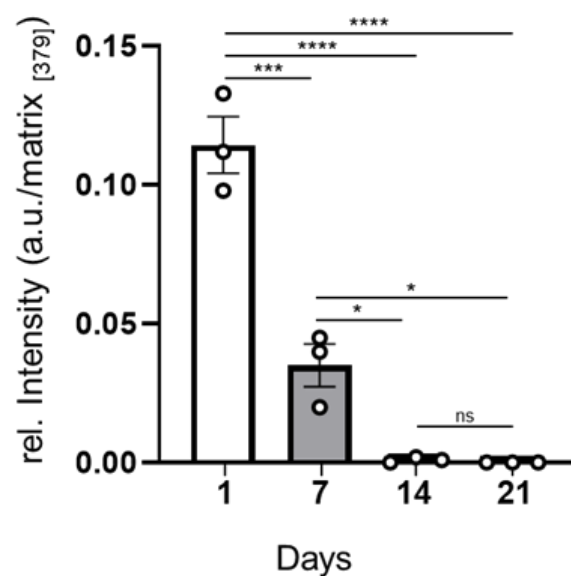
Figure S4: MS investigation of SPION-PLGA fiber degradation. MS analysis of in vitro and in vivo paraffin-embedded samples collected throughout the longitudinal evaluation of our TEVGs. Statistically significant differences were observed between samples prepared and analysed on day 0 compared to those cultivated in bioreactors for 7 and 14 days and samples implanted in vivo for 21 days. These results indicate the gradual degradation of the PLGA fibers over time, supporting the MRI data. All values were obtained in triplicates and are presented as means ± SD; One-way ANOVA with Tukey post hoc correction was applied to compare groups, indicating $p > 0.05$ as ns, $p < 0.05$ as *, $p < 0.01$ as **, $p < 0.001$ as ***, and $p < 0.0001$ as ****.

Affidavit according to § 5(1) for Data Retention

Hiermit erkläre ich, dass die dieser Dissertation zur Grunde ligenden Originaldaten (I hereby declare that the original data forming the basis of this doctoral thesis are stored) im Institut für Experimentelle Molekulare Bildgebung des Universitätklinikums Aachen hinterlegt sind.

Affidavit according to § 5 (1) and (2), and § 11 (3) 12 of the doctoral studies regulations

I, **Elena Rama,** hereby declare on oath, that I have contributed a significant part, and thus majority, of the publication:

E. Rama, S. R. Mohapatra, C. Melcher, T. Nolte, S. M. Dadfar, R. Brueck, V. Pathak, A. Rix, T. Gries, V. Schulz, T. Lammers, C. Apel, S. Jockenhoevel, F. Kiessling: Monitoring the Remodeling of Biohybrid Tissue-Engineered Vascular Grafts by Multimodal Molecular Imaging; Advance Science; 2022, Volume 9 (10).

The contributions to the publication were as follows:

	Study design	Sample preparation	Contrast agents' preparation	In vitro MRI and US	In vivo MRI	In vitro cell culture and histology	Data evaluation	Statistical evaluation	Data interpretation	Literature survey	Manuscript writing	Manuscript revising
E. Rama	50	40	50	70	80	60	75	99	60	82	100	
S. R. Mohapatra	5	30		5	5	40	5	1	5	1		5
C. Melcher		30										5
T. Nolte				20			20		5	1		5
S. M. Dadfar			40							1		5
R. Brueck					15							5
V. Pathak			10									5
A. Rix				5								5
T. Gries										1		5
V. Schulz										1		5
T. Lammers										1		5
C. Apel	5									1		5
S. Jockenhoevel	10									1		5
F. Kiessling	30								30	10		40
Sum (%)	100	100	100	100	100	100	100	100	100	100	100	100

The position as the first author obviously arises from this significant contribution.

_____
    Elena Rama

As supervisor and / or corresponding author I confirm the statements of Elena Rama and as a representative of the collaborative partners

_____
    Fabian Kiessling

As co-author I endorse the statement of Fabian Kiessling

S. R. Mohapatra	C. Melcher	T. Nolte	S. M. Dadfar	R. Brueck	V. Pathak
A. Rix	T. Gries	V. Schulz	T. Lammers	C. Apel	S. Jockenhoevel

Affidavit according to § 5 (1) and (2), and § 11 (3) 12 of the doctoral studies regulations

I, **Elena Rama,** hereby declare on oath, that I have contributed a significant part, and thus majority, of the publication:

E. Rama, S. R. Mohapatra, Y. Sugimura, T. Suzuki, S. Siebert, R. Barmin, J. Hermann, J. Baier, A. Rix, T. Lemainque, S. Koletnik, A. S. Elshafei, R. M. Pallares, S. M. Dadfar, R. H. Tolba, V. Schulz, J. Jankowski, C. Apel, P. Akhyari, S. Jockenhoevel, F. Kiessling: In Vitro and in Vivo Evaluation of Biohybrid Tissue-Engineered Vascular Grafts with Transformative ^{1}H/^{19}F MRI Traceable Scaffolds; Biomaterials; 2024, Volume 311.

The contributions to the publication were as follows:

	Study design	Sample and contrast agent preparation	In vitro cell culture	In vitro MRI / US	Surgery and in vivo MRI / US	Histology and Mass spectrometry	In vivo study legislative aspects	Data evaluation	Statistical evaluation	Data interpretation	Manuscript writing	Manuscript revising
E. Rama	30	25	80	75	40	50	30	70	80	70	100	
S.R. Mohapatra	5	25		5		10						5
Y. Sugimura					15							5
T. Suzuki					10							
S. Siebert		20										
R. Barmin		15										5
J. Hermann						30						
J. Baier					5							5
A. Rix					5							5
T. Lemainque				10								5
S. Koletnik					5							5
A. S. Elshafei			20									
R. M. Pallares		10										5
S. M. Dadfar		5										5
R. H. Tolba							35					5
V. Schulz				10								5
J. Jankowski						10						
C. Apel	5				10			5				5
P. Akhyari					10							5
S. Jockenhoevel	30							5				5
F. Kiessling	30						35	20	20	30		30
Sum (%)	100	100	100	100	100	100	100	100	100	100	100	100

The position as the first author obviously arises from this significant contribution.

_____
Elena Rama

As supervisor and / or corresponding author I confirm the statements of Elena Rama and as a representative of the collaborative partners

_____
Fabian Kiessling

As co-author I endorse the statement of Fabian Kiessling

_____ _____ _____ _____ _____ _____
S. R. Mohapatra   Y. Sugimura   T. Suzuki   S. Siebert   R. Barmin   J. Hermann

_____ _____ _____ _____ _____ _____
J. Baier   A. Rix   T. Lemainque   S. Koletnik   A. S. Elshafei   R. M. Pallares

Affidavit according to § 5 (1) and (2), and § 11 (3) 12 of the doctoral studies regulations

I, **Elena Rama,** hereby declare on oath, that I have contributed a significant part, and thus majority, of the publication:

E. Rama, S. R. Mohapatra, Y. Sugimura, T. Suzuki, S. Siebert, R. Barmin, J. Hermann, J. Baier, A. Rix, T. Lemainque, S. Koletnik, A. S. Elshafei, R. M. Pallares, S. M. Dadfar, R. H. Tolba, V. Schulz, J. Jankowski, C. Apel, P. Akhyari, S. Jockenhoevel, F. Kiessling: In Vitro and in Vivo Evaluation of Biohybrid Tissue-Engineered Vascular Grafts with Transformative ^{1}H/^{19}F MRI Traceable Scaffolds; Biomaterials; 2024, Volume 311.

The contributions to the publication were as follows:

	Study design	Sample and contrast agent preparation	In vitro cell culture	In vitro MRI / US	Surgery and in vivo MRI / US	Histology and Mass spectrometry	In vivo study legislative aspects	Data evaluation	Statistical evaluation	Data interpretation	Manuscript writing	Manuscript revising
E. Rama	30	25	80	75	40	50	30	70	80	70	100	
S.R. Mohapatra	5	25		5		10						5
Y. Sugimura					15							5
T. Suzuki					10							
S. Siebert		20										
R. Barmin		15										5
J. Hermann						30						
J. Baier					5							5
A. Rix					5							5
T. Lemainque				10								5
S. Koletnik					5							5
A. S. Elshafei			20									
R. M. Pallares		10										5
S. M. Dadfar		5										5
R. H. Tolba							35					5
V. Schulz				10								5
J. Jankowski						10						
C. Apel	5				10			5				5
P. Akhyari					10							5
S. Jockenhoevel	30							5				5
F. Kiessling	30						35	20	20	30		30
Sum (%)	100	100	100	100	100	100	100	100	100	100	100	100

The position as the first author obviously arises from this significant contribution.

_____
        Elena Rama

As supervisor and / or corresponding author I confirm the statements of Elena Rama and as a representative of the collaborative partners

_____
        Fabian Kiessling

As co-author I endorse the statement of Fabian Kiessling

_____ _____ _____ _____ _____ _____
S. M. Dadfar   R. H. Tolba   V. Schulz   J. Jankowski   C. Apel   P. Akhyari

_____
S. Jockenhoevel

ELENA RAMA

CONTACT

Melatenerstrasse 110 b, 52074 Aachen
Phone: 0039 3663283678
Email: elenarama942@gmail.com

Date of birth: 20/10/1994
Place of birth: Magenta (Italy)
Nationality: Italian

EDUCATION

01/2019 – 2024 (expected end 2024)
Doctoral studies • RWTH Aachen University, Germany

Dr. rer. medic at the Institute of Experimental Molecular Imaging (ExMI), Center for Biohybrid Medical Systems (CBMS)

Main Projects:

- Longitudinal monitoring of biohybrid tissue-engineered prostheses by multimodal molecular imaging
- Riboflavin-targeted polymers improve tolerance of paclitaxel while maintaining therapeutic efficacy

09/2013 – 12/2018
Master's degree in Pharmaceutical Chemistry and Technologies • Carlo Bo Urbino University, Department of Biomolecular Sciences, Pharmacy school, Pharmaceutical Chemistry and Technology, Urbino, Italy

04/2018 – 11/2018
Master thesis at the Institute of Experimental Molecular Imaging (ExMI), Center for Biohybrid Medical Systems (CBMS), supported by ERASMUS + TRAINEESHIP program provided by Carlo Bo Urbino University, Italy
Project: Microenvironmental characterization of multidrug resistant murine breast tumor model

07/2017 – 03/2018
Traineeship • Cantó Dr. Croce Cantó Pharmacy, Pescara, Italy

AWARDS AND CERTIFICATES

Poster Award by European Molecular Imaging Meeting (EMIM 2024)
Women in Molecular Imaging Network (WIMIN) scholar award (WMIC 2022)
Student Travel Stipend Award (WMIC 2022)
Vevo Research Award 2022 by FUJIFILM VisualSonics, Amsterdam, The Netherlands (EMIM 2022)
Poster Award by World Molecular Imaging Congress (WMIC 2021)
Basics of Laboratory Animal Science by Federation of European Laboratory Animal Science

(FELASA), category B (2019)

PRESENTATIONS

European Molecular Imaging Meeting (EMIM), 2024 (Poster)
Tissue Engineering and Regenerative Medicine International Society (TERMIS), 2023 (Talk)
European Molecular Imaging Meeting (EMIM), 2023 (Poster)
World Molecular Imaging Congress (WMIC), 2022 (Talk)
European Congress of Radiology (ECR), 2022 (EPOS)
European Molecular Imaging Meeting (EMIM), 2022 (Talk)
Tissue Engineering and Regenerative Medicine International Society (TERMIS), 2021 (Talk)
World Molecular Imaging Congress (WMIC), 2021 (e-poster)
European Molecular Imaging Meeting (EMIM), 2021 (Poster)
German young Molecular Imaging Community (GyMIC), 2021 (Talk)
Umbrella Symposium-Life Science and Engineering, 2021 (Talk)
European Molecular Imaging Meeting (EMIM), 2020 (e-poster)
German young Molecular Imaging Community (GyMIC), 2018 (Talk)

LANGUAGES

English (Full proficiency), Italian (Native), German (B1), French (A2)

INTERESTS

Reading, painting, hiking, cycling, traveling